Search for dark matter produced in association with top quarks at the Compact Muon Solenoid

by

Victor Shang

A dissertation submitted in partial fulfillment
of the requirements for the degree of
Doctor of Philosophy
(Physics)

at the
University of Wisconsin-Madison
2024

Date of Final Oral Exam: 11/25/2024
The dissertation is approved by the following members of the Final Oral Committee:
Tulika Bose, Professor, Physics
Kevin Black, Professor, Physics
Yang Bai, Professor, Physics
Elena D'Onghia, Associate Professor, Astronomy

Search for dark matter produced in association with top quarks at the Compact Muon Solenoid

Victor Shang

Abstract

One of the fundamental open questions that cannot be currently explained by the Standard Model is the particle nature of dark matter. Though astrophysical observations provide indirect evidence of its existence, dark matter has not been directly measured so far. However, under certain assumptions, dark matter may be possible to produce and detect at high energy particle colliders like the LHC.

This thesis presents a search for dark matter produced in association with top quarks in data collected by the CMS detector at the LHC, corresponding to 138 fb^{-1} of proton-proton collisions at a center-of-mass energy of 13 TeV. Production of dark matter particles in association with both a single top quark and a pair of top quarks are considered. The search is performed in three separate channels depending on the number of leptons in the final state, which include the all hadronic, single lepton, and dileptonic final states. The primary strategy of the search is to look for an excess of events with respect to the background-only prediction in events with a large imbalance in the transverse momentum. The results are interpreted in the context of a simplified model in which either a scalar or pseudoscalar mediator couples to top quarks and to dark matter fermions. Future prospects for improving the search are also discussed.

This thesis is dedicated to my family, who have provided me with their unwavering encouragement and support throughout my life. This work would not have been possible without you.

Acknowledgements

I would like to thank my advisor, Tulika Bose, for all the guidance and support she has provided me throughout my time at UW Madison. Your patience, wisdom, and expertise have been a continuous source of inspiration, and I am very fortunate to have had the opportunity to work with you.

I would also like to thank Deborah Pinna for her exceptional mentorship as well. You have been a role model to me, and your support has been invaluable to my growth as a researcher.

Furthermore, I would like to thank my collaborators at DESY, CERN, and IFCA for the work they have contributed to the DM analysis. In particular, I would like to thank Dominic William Stafford and Danyer Perez Adan for their efforts and insights that have been essential to the success of this search.

I would like to extend my sincere gratitude towards Alexander Savin for his supervision, as well as Varun Sharma and Pallabi Das for their assistance on working with the CaloL1 trigger. Moreover, I would like to thank Charis Kleio Koraka for the opportunity to work together on the VLL analysis, and Huiling Hua for the privilege of working together as TOP HLT co-conveners.

In addition, I would like to thank all the members of the Wisconsin CMS group for their collaboration and support. A special thanks goes out to my officemates, Abhishikth Mallampalli, He He, Ho Fung, Ganesh Parida, and Mitanshu Thakore, for their encouragement and camaraderie throughout the years.

Finally, I would like to extend my thanks to all my family and friends who have supported me throughout my time at UW Madison.

Contents

List of Figures

List of Tables

Chapter 1

Introduction

Over the last several decades, the Standard Model (SM) of particle physics has been extremely successful at describing the fundamental constituents of matter and their interactions. Many experiments have been conducted to test the electromagnetic, weak, and strong interactions and have found agreement with Standard Model predictions to extraordinary precision. However, there are still important open questions remaining that require the addition of physics beyond the Standard Model. One of these fundamental open questions is the nature of dark matter (DM).

Evidence for DM comes from various astrophysical observations, which set certain constraints on the properties that a candidate for DM must satisfy. Since the SM does not provide an explanation for DM, physics beyond the standard model (BSM) must be explored. One type of candidate is a weakly interacting massive particle (WIMP), which is a hypothetical particle predicted to have weak scale interactions with SM particles. Since WIMPs are predicted to have mass on the weak scale, it is possible to search for these candidates at high energy particle colliders such as the Large Hadron Collider (LHC) built at the European Organization of Nuclear Research (CERN) near Geneva, Switzerland.

This thesis describes an analysis searching for DM produced in association with top quarks using data collected from 2016–2018 by the Compact Muon Solenoid (CMS) at the LHC. This chapter provides a brief overview of the SM of particle physics. Chapter 2 covers the astrophysical evidence for DM as well as the theoretical framework used in the analysis. Chapter 3 describes the LHC and the different components of the CMS detector, including the SWATCH framework I worked on. Chapter 4 describes how the objects used in the analysis are reconstructed and identified. Chapter 5 covers the details and results of the DM analysis, including the strategy and variables used to distinguish DM events from SM processes as well as the statistical techniques used to analyze the data. Chapter 6 describes possible future improvements for the analysis as well as other possible BSM searches. Finally, chapter 7 provides a short summary of the thesis.

1.1 The Standard Model of particle physics

The SM of particle physics [1–4] is a theory that describes the fundamental particles and forces that govern the behavior of matter in the universe, with the sole exception of gravity, which is described by the theory of general relativity instead [5]. In more formal terms, it is a relativistic quantum field theory which is characterized by a global Poincare symmetry and a local gauge symmetry given by

$$G_{\mathrm{SM}} = \mathrm{SU}(3)_{\mathrm{C}} \otimes \mathrm{SU}(2)_{\mathrm{L}} \otimes \mathrm{U}(1)_{\mathrm{Y}} \tag{1.1}$$

where C, L, and Y are identified as the color charge, weak isospin, and the weak hypercharge of the symmetry groups, respectively. Elementary particles are then defined as excited states of the underlying quantum fields of this description.

Poincaré symmetry describes symmetry under the Poincaré group, which includes spatial and temporal translations, spatial rotations, and Lorentz boosts in Minkowski spacetime. By Noether's theorem [6], each of these symmetries directly implies a conservation law. In particular, symmetry under spatial and temporal translations implies conservation of energy and momentum, symmetry under spatial rotations implies conservation of angular momentum, and symmetry under Lorentz boosts implies conservation of center-of-mass velocity. These global symmetries ensure that the SM is consistent with the laws of special relativity [7].

The local $\mathrm{SU}(3)_\mathrm{C} \otimes \mathrm{SU}(2)_\mathrm{L} \otimes \mathrm{U}(1)_\mathrm{Y}$ gauge symmetries characterize the fundamental interactions described by the SM, those being the strong, weak, and electromagnetic interactions. These gauge symmetries dictate the interactions between elementary particles through invariance under local transformations. The $\mathrm{SU}(3)_\mathrm{C}$ group is responsible for determining the strong interaction, which is described by Quantum Chromodynamics (QCD) and characterized by the color charge C. There are three types of color charges, and transformations under $\mathrm{SU}(3)_\mathrm{C}$ describe rotations in this color space. The $\mathrm{SU}(2)_\mathrm{L}$ group is responsible for determining the weak interaction and is characterized by the weak isospin L. Finally, the $\mathrm{U}(1)_\mathrm{Y}$ group is responsible for determining the electromagnetic interaction and is characterized by the weak hypercharge Y.

Each elementary particle in the SM is described as an excited state of a quantum field. These elementary particles are characterized by both their transformations under the local gauge symmetry $\mathrm{SU}(3)_\mathrm{C} \otimes \mathrm{SU}(2)_\mathrm{L} \otimes \mathrm{U}(1)_\mathrm{Y}$ as well as what is known as spin s (or helicity). The spin of a particle is a form of intrinsic angular momentum that determines their statistical properties depending on whether the spin is an integer or half-integer value. Particles with half-integer spin, called fermions, follow Fermi-Dirac statistics and obey the Pauli exclusion principle [8], which means two fermions cannot occupy the same quantum state. On the other hand, particles with integer spin, called bosons, follow Bose-Einstein statistics and are allowed to occupy the same state.

Fermions in the SM are divided into two categories: leptons and quarks. The leptons are described by three generations of lepton pairs, with each generation of charged leptons being heavier than the last. These include the first generation electron (e) and electron neutrino (ν_e), the second generation muon (μ) and muon neutrino (ν_μ), and the third generation tau (τ) and tau neutrino (ν_τ). Leptons are characterized by the fact that they carry integer electric charge (0 or $\pm e$, where e is the elementary electric charge), but do not carry any color charge, and therefore do not interact with the strong interaction. Similarly, quarks are also described by three generations of an up-type and a down-type quark, which include the first generation up (u) and down (d) quarks, the second generation charm (c) and strange quarks, and the third generation top (t) and bottom (b) quarks. Up-type and down-type quarks carry an electric charge of $2e/3$ and $-e/3$, respectively, and also carry a non-zero color charge.

Fermions are further subdivided into different chirality states depending on how they transform under the $\mathrm{SU(2)_L}$ group. Fermions with left-handed chirality under $\mathrm{SU(2)_L}$ form doublets, namely

$$q_\mathrm{L} = \begin{pmatrix} u_\mathrm{L} \\ d_\mathrm{L} \end{pmatrix}, \qquad l_\mathrm{L} = \begin{pmatrix} \nu_\mathrm{L} \\ e_\mathrm{L} \end{pmatrix}, \tag{1.2}$$

while fermions with right-handed chirality under $\mathrm{SU(2)_L}$ form singlets: u_R, d_R, and e_R, where u, d, e, and ν are up-type quarks, down-type quarks, charged leptons, and neutrinos, respectively. Right-handed neutrinos are not included in the SM under the assumption that the SM neutrinos are massless, though recent evidence have refuted this assumption [9, 10]. Nonetheless, in the following formulation of the SM we shall continue to hold this assumption.

Gauge bosons in the SM are the force carriers that mediate the interactions between elementary particles. The electromagnetic force is mediated by the massless photon (γ), the weak force is mediated by the massive Z and $\mathrm{W}^{\pm}$ bosons, and the strong force is mediated by the massless gluon g. There is also a special spin-0 bosonic field called the Higgs field which is responsible for generating the masses of the massive gauge bosons through the Brout-Englert-Higgs mechanism [11–13]. Fermions acquire mass through their Yukawa coupling to the Higgs field [2] after electroweak symmetry breaking, which takes the form

$$y_f = \frac{\sqrt{2}m_f}{v}, \tag{1.3}$$

where y_f is the coupling of the fermion to the Higgs field, m_f is the mass of the fermion, and $v = 246.22$ GeV is the vacuum expectation value (VEV) of the Higgs field. Thus, the coupling of a fermion to the Higgs field is directly proportional to its mass, which is a key feature of the Yukawa coupling that will become important later on with respect to the

DM model used in the analysis. A summary of the group properties of the elementary particles of the SM are shown in Table 1.1.

Name	Label	$\mathrm{SU(3)_C}$	$\mathrm{SU(2)_L}$	$\mathrm{U(1)_Y}$	Spin
Quarks	$Q^i_\mathrm{L} = (u^i_\mathrm{L}, d^i_\mathrm{L})$	3	2	1/3	1/2
	u^i_R	3	1	4/3	1/2
	d^i_R	3	1	-2/3	1/2
Leptons	$L^i_\mathrm{L} = (\nu^i_\mathrm{L}, e^i_\mathrm{L})$	1	2	-1	1/2
	e^i_R	1	1	-2	1/2
Higgs boson	H	1	2	1	0
Photon	γ	1	1	0	1
W/Z bosons	$W^\pm, Z^0$	1	3	0	1
Gluons	g_α	8	1	0	1

Table 1.1: Elementary fermions and bosons of the SM, their group properties under the symmetry groups $\mathrm{SU(3)_C}$, $\mathrm{SU(2)_L}$, and $\mathrm{U(1)_Y}$, and their spin. The value under the $\mathrm{SU(3)_C}$ and $\mathrm{SU(2)_L}$ columns denote the representation that each particle field transforms under, while the value under the column $\mathrm{U(1)_Y}$ denotes the value of the weak hypercharge Y.

The dynamics and interactions of these elementary particles are then described by a Lagrangian of the form

$$\mathcal{L}_\mathrm{SM} = \mathcal{L}_\mathrm{gauge} + \mathcal{L}_\mathrm{fermions} + \mathcal{L}_\mathrm{Higgs} + \mathcal{L}_\mathrm{Yukawa} \tag{1.4}$$

where $\mathcal{L}_\mathrm{gauge}$ represents the gauge field terms, $\mathcal{L}_\mathrm{fermions}$ represents the terms associated with fermions, $\mathcal{L}_\mathrm{Higgs}$ represents the terms associated with the Higgs mechanism, and $\mathcal{L}_\mathrm{Yukawa}$ represents terms associated with Yukawa interactions of fermions with the Higgs field.

1.1.1 The electroweak interaction

The electromagnetic and weak interactions, together called the electroweak interactions, are generated by the group $\mathrm{SU(2)_L \otimes U(1)_Y}$, where $\mathrm{SU(2)_L}$ represents the weak isospin and $\mathrm{U(1)_Y}$ represents the weak hypercharge. Since left- and right-handed fermions transform differently under $\mathrm{SU(2)_L}$, the electroweak interaction is considered a chiral gauge theory, which means the weak interaction is not invariant under parity transformations. The electroweak Lagrangian contains both kinetic terms for the gauge fields as well as for fermions that are given by

$$\mathcal{L}_{\mathrm{EW}} = -\frac{1}{4}W^a_{\mu\nu}W^{a\mu\nu} - \frac{1}{4}B_{\mu\nu}B^{\mu\nu} + \overline{\psi}i\gamma^\mu D_\mu\psi, \tag{1.5}$$

where

$$W^a_{\mu\nu} = \partial_\mu W^a_\nu - \partial_\nu W^a_\mu + g\epsilon^{abc}W^b_\mu W^c_\nu \tag{1.6}$$

is the field strength tensor for the non-Abelian gauge fields W^a_μ $(a = 1, 2, 3)$ of $\mathrm{SU}(2)_\mathrm{L}$,

$$B_{\mu\nu} = \partial_\mu B_\nu - \partial_\nu B_\mu \tag{1.7}$$

is the field strength tensor of the Abelian gauge field B^μ of $\mathrm{U}(1)_\mathrm{Y}$, ψ are the fermionic fields, γ^μ are the gamma matrices, and D_μ is the covariant derivative of the $\mathrm{SU}(2)_\mathrm{L}\otimes\mathrm{U}(1)_\mathrm{Y}$ gauge fields.

The Lagrangian given in Eq. 1.5 predicts the existence of four gauge bosons. These bosons arise from the $\mathrm{SU}(2)_\mathrm{L} \otimes \mathrm{U}(1)_\mathrm{Y}$ gauge fields through a process described by the Brout-Englert-Higgs mechanism in which the electroweak symmetry is spontaneously broken, giving mass to the $W^\pm$ and Z bosons that mediate the weak force. The remaining electroweak boson remains massless and is identified as the photon.

The electroweak Lagrangian in Eq. 1.5 also includes Higgs and Yukawa terms coupling the gauge fields and fermions to the Higgs field (not shown) that will be covered in Section 1.1.3. The electroweak interactions are responsible for both the interactions between charged particles as well as interactions involving the weak force, such as radioactive decay.

1.1.2 Quantum chromodynamics

The strong interaction is described by QCD and is generated by the group $\mathrm{SU}(3)_\mathrm{C}$, which represents the strong color charge. There are three color charges, conventionally named red, green, and blue, and quarks which carry non-zero color charge form color triplets under $\mathrm{SU}(3)_\mathrm{C}$. There are also eight generators of $\mathrm{SU}(3)_\mathrm{C}$ corresponding to eight independent color transformations, which result in eight types of gauge bosons called gluons.

Though these gluons differ in their color charge, their other properties are identical. These gluons are the mediators of the strong interaction and are neutral and massless like the photon. However, since the SM is a Yang-Mills theory [14], the non-Abelian nature of the $\mathrm{SU}(3)_{\mathrm{C}}$ group implies that unlike photons, gluons can have self-interaction terms in the SM Lagrangian.

The QCD Lagrangian is given by

$$\mathcal{L}_{\mathrm{QCD}} = \overline{q}\left(i\gamma^{\mu} D_{\mu} - m_q\right) q - \frac{1}{4} G^{\alpha}_{\mu\nu} G^{\alpha\mu\nu}, \tag{1.8}$$

where q are the quark fields, D_{μ} is the covariant derivative for the $\mathrm{SU}(3)_{\mathrm{C}}$ gauge field given by

$$D_{\mu} = \partial_{\mu} - i g_s T^{\alpha} G^{\alpha}_{\mu} \tag{1.9}$$

with T^{α} being the generators of the SU(3) group, m_q is the mass of the quarks, and $G^{\alpha}_{\mu\nu}$ is the gluon field strength tensor given by

$$G^{\alpha}_{\mu\nu} = \partial_{\mu} G^{\alpha}_{\nu} - \partial_{\nu} G^{\alpha}_{\mu} + g_s f^{abc} G^{b}_{\mu} G^{c}_{\nu}, \tag{1.10}$$

with g_s being the strong coupling constant and f^{abc} being the structure constants of the SU(3) group for $a = 1, \ldots, 8$. One of the key properties of QCD is that due to color confinement, quarks and gluons do not appear as isolated particles. Instead, they appear as composite particles called hadrons. Since the LHC is a proton-proton collider, this property becomes important in considering how to identify and reconstruct elementary particles such as quarks involving QCD interactions.

Another important property of QCD is that unlike the electroweak interaction, the strong force gets weaker at smaller distances and at higher energies. This property is known as asymptotic freedom, and it also becomes important at the LHC in allowing for perturbative calculations in high energy scattering processes that are used in the analysis. Without asymptotic freedom, perturbative calculations would not be possible at the energy scales considered at the LHC.

1.1.3 The Higgs mechanism and Yukawa interactions

The last two terms in the SM Lagrangian given by Eq. 1.4 describe the Higgs mechanism and Yukawa interactions between fermions and the Higgs field. Starting with the Higgs term, the Lagrangian is given by two components: one for the kinetic term, and one for the Higgs potential. The Lagrangian for the kinetic term takes the form

$$\mathcal{L}_{\text{Higgs,kin}} = (D_\mu \phi)^\dagger (D^\mu \phi) \tag{1.11}$$

where ϕ is the Higgs field doublet given by

$$\phi = \begin{pmatrix} \phi^+ \\ \phi^0 \end{pmatrix} \tag{1.12}$$

and

$$D_\mu \phi = \left(\partial_\mu - i\frac{g}{2}\tau^i W_\mu^i - i\frac{g'}{2} B_\mu \right) \phi \tag{1.13}$$

is the covariant derivative acting on the Higgs field. The Lagrangian for the potential term takes the form

$$V(\phi) = -\mu^2 \phi^\dagger \phi + \lambda (\phi^\dagger \phi)^2 \tag{1.14}$$

where μ^2 and λ are real numbers to ensure unitarity. The Higgs mechanism occurs when $\mu^2 > 0$, which results in a non-zero VEV for the Higgs field given by

$$\langle \phi \rangle_0 = \begin{pmatrix} 0 \\ \frac{v}{\sqrt{2}} \end{pmatrix}, \qquad \text{with} \qquad v = \sqrt{\frac{\mu^2}{\lambda}}. \tag{1.15}$$

Figure 1.1 shows what the Higgs potential in Eq. 1.14 looks like when $\mu^2 > 0$. Choosing any point at the bottom of the potential spontaneously breaks the rotational U(1) symmetry. It is important to note that the original Lagrangian in Eq. 1.14 remains invariant under the original SM gauge symmetry. However, by selecting a particular minimum ground state for the Higgs potential, the symmetry $\mathrm{SU(2)_L} \otimes \mathrm{U(1)_Y}$ is broken down to $U(1)_{\mathrm{EM}}$, resulting in spontaneous electroweak symmetry breaking.

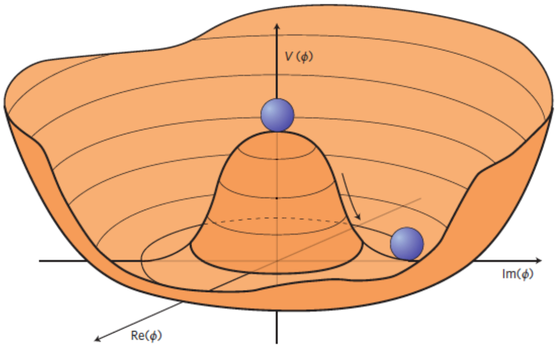

Figure 1.1: An illustration of the Higgs potential given in Eq. 1.14 for the case $\mu^2 > 0$. Figure taken from [15].

This mechanism results in generating the masses of the massive gauge bosons through the Higgs mechanism as well as generating the mass of the Higgs boson itself. A non-zero VEV for the Higgs field also results in the generation of masses for fermions though the Yukawa coupling described in Eq. 1.3. The Lagrangian for the Yukawa interaction is given by [16]

$$\mathcal{L}_{\text{Yukawa}} = -y_f(\overline{L}_L\phi e_R + \overline{Q}_L\tilde{\phi}u_R + \overline{Q}_L\phi d_R) + \text{h.c.} \tag{1.16}$$

where $(L_L,\, Q_L)$ are the left-handed fermion doublets, $(e_R,\, u_R,\, d_R)$ are the right-handed fermion singlets, y_f are the Yukawa coupling constants, $\tilde{\phi} = i\tau^2\phi^*$ is the conjugate of the Higgs doublet, f represents the different fermion types, and h.c. is the Hermitian conjugate of the previous terms. A summary of the masses and electric charges of the elementary particles of the SM as well as their interactions with the fundamental forces are shown in Table 1.2.

1.1.4 Limitations of the Standard Model

With the discovery of the Higgs boson in 2012 at the LHC [18–20], all the elementary particles predicted by the SM have been experimentally verified, and all 19 free parameters of the model have also been experimentally verified and found to be consistent with predictions to extraordinary precision [21–23]. Although the SM has seen incredible success in describing the interactions of elementary particles, there remain open questions that the

Type	Particle	Charge (e)	Mass	Interaction
Quarks	u	2/3	2.16 MeV	EM, Weak, Strong
	c	2/3	1.27 GeV	EM, Weak, Strong
	t	2/3	172.7 GeV	EM, Weak, Strong
	d	-1/3	4.67 MeV	EM, Weak, Strong
	s	-1/3	93.4 MeV	EM, Weak, Strong
	b	-1/3	4.18 GeV	EM, Weak, Strong
Leptons	e	-1	0.511 MeV	EM, Weak
	μ	-1	105.7 MeV	EM, Weak
	τ	-1	1.777 GeV	EM, Weak
	ν_e	0	≈ 0	Weak
	ν_μ	0	≈ 0	Weak
	ν_τ	0	≈ 0	Weak
Higgs boson	h	0	125 GeV	–
Photon	γ	0	0	EM
W bosons	$W^\pm$	± 1	80.4 GeV	EM, Weak
Z boson	Z^0	0	91.2 GeV	Weak
Gluons	g_α	0	0	Strong

Table 1.2: Elementary fermions and bosons of the SM, their electric charge, mass, and which fundamental interactions they participate in. Values taken from [17].

SM does not explain. One of the most notable questions is the origin of non-zero neutrino masses. In the SM, there are no right-handed neutrino fields, so neutrinos are predicted by the SM to be massless. However, observation of neutrino flavor oscillations [9, 10] implies that at least two of the neutrinos in the SM are massive. Theories have been proposed to explain the mass of the neutrinos such as through a see-saw mechanism of neutrino mass generation with the addition of heavy right-handed Majorana neutrinos [24] or the existence of sterile neutrinos [25, 26], which do not interact with the SM and mix with the SM neutrinos to give them mass. What these theories all have in common is that they require an extension of the SM to BSM physics in order to explain the non-zero mass of neutrinos.

Another notable component missing from the SM is a description of the gravitational force. Our current best theory of gravity is described by general relativity, but attempts to unify gravity with the SM through the introduction of a quantum gravity field result in non-renormalizable theories, making general relativity and the SM mathematically inconsistent [27]. In addition, the SM is defined on a fixed spacetime background, while in general relativity spacetime is a dynamic entity influenced by the distribution of matter through the Einstein field equations. Though attempts have been made to incorporate gravity into the SM through the proposal of BSM theories like string theory [28], no direct evidence has been observed for any of these BSM theories so far.

There are many other open questions that the SM cannot explain, but this thesis will focus on one in particular; the nature of DM. DM is thought to make up about 26% of the universe's total mass-energy content, while ordinary matter from the SM only makes up about 5%. Thus, even though the SM provides an accurate and precise description of ordinary matter, it does not provide a description for most of the matter comprising the universe. Though it does not interact with the electromagnetic force, DM has been indirectly observed through its gravitational interaction on visible matter. This evidence comes from astrophysical observations from various sources, including galactic rotation curves, gravitational lensing, and the Cosmic Microwave Background (CMB). From these observations, DM candidates must satisfy certain properties that rule out any elementary particle of the SM. Therefore, explaining the nature of DM requires BSM physics that can be confirmed through either direct or indirect measurements.

Chapter 2

The Search for Dark Matter

Though the particle nature of dark matter (DM) is still an open question, there has been a significant amount of indirect evidence that suggests its presence across the universe. This chapter provides an overview of the historical evidence and theory behind DM, as well as current efforts to search for it. Section 2.1 provides historical context and evidence for DM that comes from astrophysical observations. Section 2.2 describes some of the possible candidates for DM as well as the properties they must satisfy. Finally, Section 2.3 covers current methods to look for DM through various detection methods.

2.1 Historical evidence for dark matter

2.1.1 Early observations

The history of DM dates back all the way to the late 19th century, when astronomers had already began to propose the existence of non-luminous objects to explain dark regions in dense stellar fields [29]. Though there was no unanimous agreement about the existence of these dark structures, work was already being done on estimating its possible abundance in the universe. Lord Kelvin was one of the first to attempt to estimate the amount of DM in the Milky Way galaxy through the relationship between the size of the galaxy and the velocity dispersion of the stars [30]. He also obtained an upper limit on the density of this DM in the galaxy by arguing that larger densities would conflict with the observed velocities of stars. Other astronomers such as Henri Poincaré, Jacobus Kapteyn, and Jan oort also argued for the existence of DM in the Milky Way galaxy and provided their own estimations of the amount of DM near neighboring stars [31–33].

One of the most notable estimations of the density of DM was made by Fritz Zwicky, who used the dispersion velocity of galaxies in the Coma cluster to calculate its mass from its gravitational potential and then comparing the value to its mass from luminosity measurements [34]. From the virial theorem, for a conservative force we have

$$\langle T \rangle = -\frac{1}{2}\sum_{k=1}^{N}\langle \mathbf{F}_k \cdot \mathbf{r}_k \rangle \tag{2.1}$$

where T is the total kinetic energy of N particles, $\mathbf{F}_k$ represents the force on the kth particle, and $\mathbf{r}_k$ is the position of the kth particle. For the gravitational force described by Newtonian dynamics, Eq. 2.1 reduces to

$$2\langle T \rangle = -\langle U \rangle \tag{2.2}$$

where $\langle U \rangle$ is the average gravitational potential energy of the system. Thus, by measuring the velocity dispersion of the galaxies in the cluster, one can estimate the mass of the Coma cluster using the formula

$$M_{\text{virial}} = \frac{5R\sigma_v^2}{G} \tag{2.3}$$

where M_{virial} is the total mass of the cluster, R is its radius, σ_v is the velocity dispersion of its components, and G is the gravitational constant.

After comparing the mass calculated from the cluster's velocity dispersion to that obtained from luminosity measurements, Zwicky found that the visible mass of the Coma Cluster was too small to account for the velocity dispersion that was measured. Given the mass as estimated from its luminosity, the value of the velocity dispersion for the Coma Cluster he expected was 80 km/s while the value he observed was approximately 1000 km/s. As a result, he proposed the existence of non-luminous, or dark, matter that would explain the discrepancy in the velocity dispersion value he measured.

Another important contribution to early evidence for DM came from observations of galactic rotation curves by Vera Rubin and Kent Ford [35]. From Newtonian dynamics, assuming the mass of a galaxy is concentrated in its center, then the orbital velocity $v(r)$ of objects in the galaxy can be expressed as

$$v(r) = \sqrt{\frac{GM(r)}{r}} \tag{2.4}$$

where G is the gravitational constant, $M(r)$ is the mass of the galaxy, and r is the radius of the object from the center of the galaxy. Thus, one expects that measurements of the orbital velocity of objects like stars around a galaxy should follow an inverse square relationship as $v(r) \propto 1/\sqrt{r}$ as a function of its radius from the galactic center, which implies that the outer regions of galaxies should exhibit slower rotation speeds compared to their inner regions.

However, what Rubin and Ford found instead was that stars and gas in the outer regions of galaxies were orbiting at nearly the same speed as those near the center. Like Zwicky, Rubin and Ford had used luminosity measurements, in particular spectrographs measuring the Doppler shift of stars and gas, to estimate the mass of these galaxies in order to predict orbital velocities. This discrepancy between the expected and observed orbital velocities of objects within these galaxies led to the realization that there could be non-luminous matter, such as the DM proposed by Zwicky, that needed to be taken into account to explain their observations. Since the orbital velocity remains relatively constant at high velocities, from Eq. 2.4 this implies the presence of a DM halo around the galaxy whose mass distribution is approximately given by $M(r) \propto r$ in order to account for the discrepancy observed. Figure 2.1 shows the galactic rotation curve for NGC 6503, where the contributions from the galactic disk and gas are shown in comparison to what is obtained from data, as well as the contribution needed from a DM halo to match observations from data.

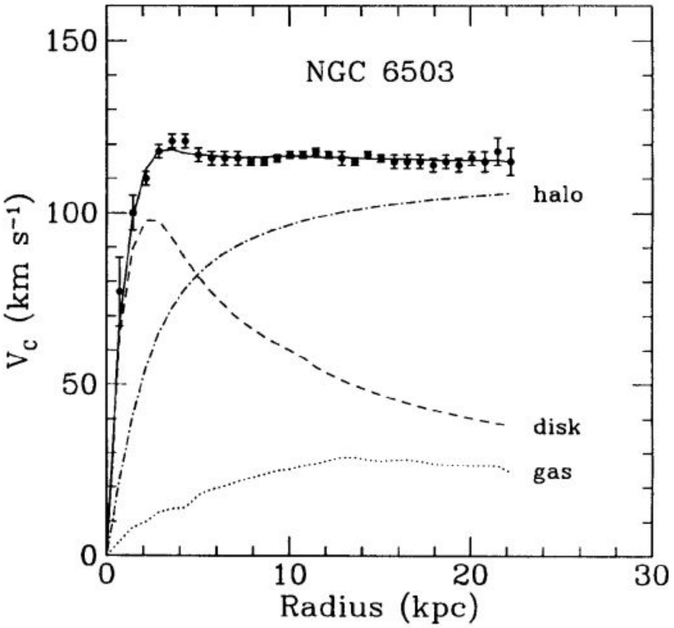

Figure 2.1: Galactic rotation curve for NGC 6503 showing disk and gas contribution plus the DM halo contribution needed to match the data. Figure taken from [36].

2.1.2 Gravitational lensing

One of the most direct pieces of evidence for DM comes from gravitational lensing measurements of galaxy clusters. From general relativity, light is expected to bend around massive objects. Therefore, the mass of an object can be inferred from measuring the bending of light from background objects like distant galaxies around a massive object like a galaxy cluster, a phenomenon known as gravitational lensing. This mass can then be compared to the mass observed from luminosity measurements like X-ray measurements to see if they agree. Any discrepancies observed imply a difference in the distribution of luminous matter compared to the total matter in the galaxy or cluster, indicating the presence of DM.

Multiple gravitational lensing measurements have confirmed the presence of DM in many different galaxies and galactic clusters [37]. One notable example of these measurements is that of 1E 0657-56 [38], otherwise known as the "Bullet Cluster", which was formed from the merging of two galactic clusters. Figure 2.2 shows the matter distribution of the Bullet Cluster as calculated from X-ray measurements in pink compared to the matter distribution calculated from gravitational lensing in blue. One can see that these two distributions are offset from each other, indicating that the Bullet Cluster contains non-luminous matter in addition to the luminous matter measured from X-rays. The offset in these distributions can be explained from the fact that during the collision of the two galactic clusters, the hot X-ray emitting gas in pink will slow down and interact through friction, leading to a matter distribution centered around the collision point. However, the visible galaxies which contain the DM are minimally affected and instead pass through relatively unimpeded. This behavior results in the majority of the gravitational mass in blue residing in regions separated from the hot gas, leading to the separation in the pink and blue regions.

Not only do these gravitational lensing measurements provide further evidence for DM, but they also provide a glimpse into some of its properties. For example, the fact that the gravitational mass stays aligned with the position of the galaxies during the collision of galactic clusters in the Bullet Cluster indicates that DM does not interact with the electromagnetic force or standard frictional forces, in contrast to the host X-ray emitting gas. In addition, these measurements provide evidence against alternative theories to DM such as Modified Newtonian Dynamics (MOND) [39], which propose a modification to the theory of gravity instead of the presence of DM. Though these MOND theories can provide alternative explanations to the galactic rotation curves described in Section 1.1.1, they face much more difficulties in explaining results of gravitational lensing measurements without resorting to including some form of non-luminous matter. Therefore, gravitational lensing measurements of objects like the Bullet Cluster provide some of the strongest pieces of evidence for DM.

2.1.3 The Cosmic Microwave Background

Though there were early attempts to estimate the amount of DM around various astrophysical objects like stars and galaxies, it was not until the discovery of the Cosmic Microwave

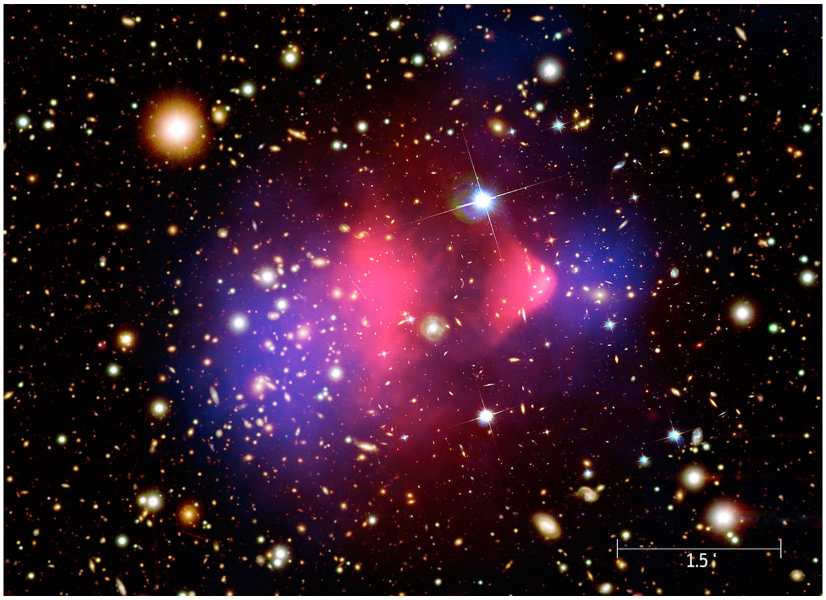

Figure 2.2: Image of the matter distribution in 1E 0657-56, known as the "Bullet Cluster", as calculated from X-ray measurements (pink) in comparison to the matter distribution as calculated from gravitational lensing (blue), superimposed over visible light from galaxies. Figure taken from [40].

Background (CMB) [41] that an estimate could be made for the total amount of DM in the universe. The CMB is the background radiation left over from the early universe after the Big Bang, during which the universe was filled with a hot, dense plasma of protons, electrons, and other particles. During this period, photons underwent constant scattering with free electrons through Thomson scattering, preventing them from freely traveling. Eventually, after around 380,00 years when the universe cooled enough for protons and electrons to combine into neutral hydrogen atoms during the recombination epoch [42], photons were able to finally travel freely, leading to decoupling of matter and radiation. This remnant radiation of the CMB can still be detected today, leaving a faint signal in the universe with a nearly uniform temperature of $\sim$2.72 Kelvin, shown in Fig. 2.3.

However, because of the coupling between photons and baryons in the early universe, acoustic oscillations created through the interactions of photons and baryons through radiation pressure and gravity led to small scale anisotropies in the temperature of the CMB [44, 45]. The power spectrum of these temperature anisotropies in the CMB is

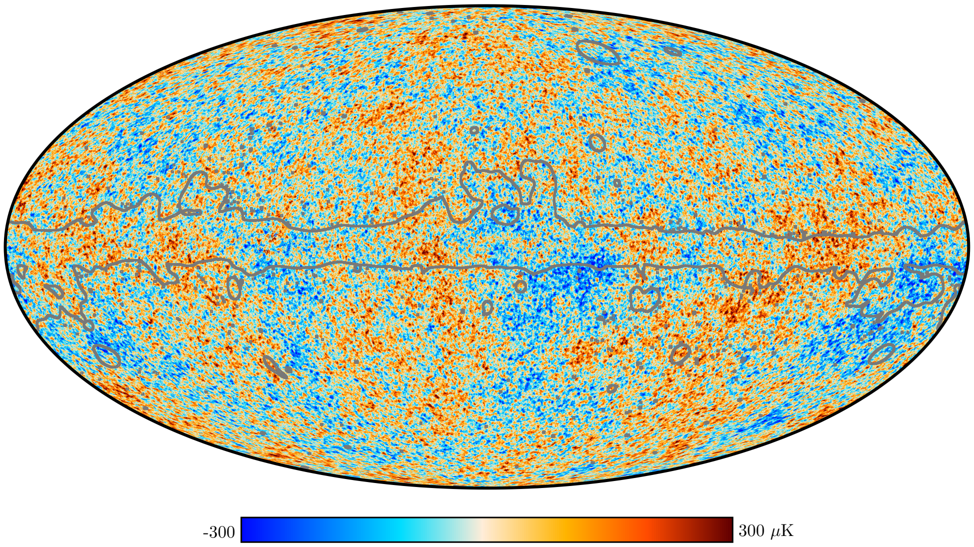

Figure 2.3: Image of the temperature anisotropies of the CMB as observed by the European Space Agency's Planck mission on the sky based on data published in July 2018. The gray outline shows the extent of the confidence mask, used to indicate regions of the CMB that are contaminated by foreground emissions. Figure taken from [43].

influenced by density fluctuations of matter and energy in the early universe and can therefore provide an estimate of the abundance of DM in the universe. In particular, by analyzing the acoustic peaks of the power spectrum for the CMB as a function of the multiple moment ℓ, which is a measure of the angular scale, one can extract cosmological parameters describing the total baryonic matter, DM, and dark energy in the universe.

Figure 2.4 shows the temperature-temperature (TT) power spectrum of the CMB as a function of ℓ. The spectrum is fit to the standard model of cosmology called the Lambda Cold Dark Matter (ΛCDM) model [46], which includes the following cosmological parameters in addition to others:

- $\mathbf{\Omega_b}$: the density of baryonic matter, which is ordinary matter composed of quarks.
- $\mathbf{\Omega}_{\mathrm{DM}}$: the density of cold DM.
- $\mathbf{\Omega_\Lambda}$: the density of dark energy, corresponding to the cosmological constant that drives the expansion of the universe.

The first peak in Fig. 2.4 describes the total matter density in the universe, including

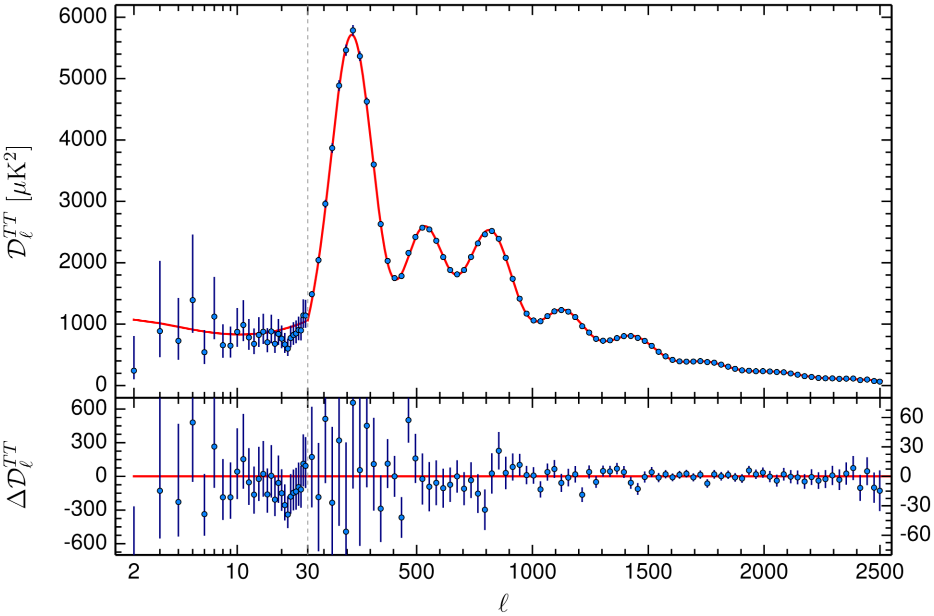

Figure 2.4: Image of the temperature-temperature (TT) power spectrum of the CMB as observed by the European Space Agency's Planck mission on the sky based on data published in Feb 2015. The blue dots correspond to measurements made by the Planck satellite with their corresponding error bars, while the red curve represents the best fit to the standard model of cosmology to data. Figure taken from [43].

both baryonic and dark matter. The second and third peaks depend on the baryonic and DM density Ω_b and $\Omega_{\rm DM}$, respectively. To extract these cosmological parameters, the temperature anisotropies are fit to an expansion of the form

$$\Delta T(\theta, \phi) = \sum_{\ell=0}^{\infty} \sum_{m=-\ell}^{\ell} a_{\ell m} Y_{\ell m}(\theta, \phi), \tag{2.5}$$

where ΔT are the temperature anisotropies, θ and ϕ denote the angular position of the anisotropy, ℓ is the multiple moment, $a_{\ell m}$ are spherical harmonic coefficients of the expansion, and $Y_{\ell m}$ are spherical harmonics. The CMB power spectrum C_ℓ is then given by

$$C_\ell = \langle |a_{\ell m}|^2 \rangle. \tag{2.6}$$

From this spectrum, the best-fit parameters of the ΛCDM model can be derived. Based on data published in 2018 by Planck, the total density of baryonic matter and DM is estimated to be [47]:

$$\Omega_{\mathrm{DM}} \approx 0.26, \qquad \Omega_b \approx 0.049 \tag{2.7}$$

From these values, DM is estimated to make up about 26% of the total energy density in the universe and around 85% of the total matter in the universe, with the remaining energy density consisting of dark energy. Thus, DM is not only predicted to exist but is also predicted to be the dominant form of matter in the universe.

2.2 Dark matter candidates

2.2.1 Properties of dark matter

Given the current astrophysical evidence, any DM candidate must satisfy several constraints in order to explain its observed cosmological effects. The most obvious constraint is that it must interact gravitationally, eliminating any candidates which are massless like photons or gluons. Another important constraint is that DM does not interact electromagnetically or through the strong interaction. This constraint comes from results from Planck [47] as well as previous experiments described in Section 2.1, which show that DM does not emit, absorb, or reflect light. As a result, DM cannot carry any electromagnetic charge in order to remain non-luminous. In addition, any electromagnetic interaction with DM would leave imprints on the CMB and affect the temperature anisotropies observed. The collisionless nature of DM observed in measurements of objects like the Bullet Cluster also implies that DM cannot carry a color charge as that would lead to interactions between DM and baryonic matter, which would cause DM to clump more tightly than observed [48]. Strong interactions with DM would also lead to different structures of galaxies and clusters than those predicted by the ΛCDM model [49], which provides the current best fit to cosmological and astrophysical observations.

In addition, DM must be long-lived and stable on the time scale of the lifetime of the universe [50]. If DM was not long-lived or stable, we would not be able to observe the current abundance as measured by the CMB. The long lifetime of DM also plays an important role in explaining the formation of large-scale structures like galaxies and clusters, which have existed for billions of years. If DM decays too quickly, these structures would not have been able to form. Indirect detection experiments looking for the decay of DM have also played stringent lower limits on DM's lifetime.

As the name implies, DM in the current standard model of cosmology, the Lambda cold dark matter (ΛCDM) model, must also be cold, or non-relativistic [51]. If DM were relativistic, or hot, then there would be a significant difference in the distribution and formation of structures in the universe. In particular, hot DM would erase smaller density perturbations in the early universe, leading to a top-down approach of the formation of astrophysical objects like stars and galaxies from larger scale structures. However, simulations show that the formation of structures in the universe followed a bottom-up approach, starting from the clumping of gas into smaller scale structures which merged to form larger ones like galaxies and clusters [52]. Measurements of the CMB anisotropies also confirm the results of these simulations, constraining DM to be cold during the early universe.

Finally, any DM candidate must account for the abundance observed from CMB measurements. Thus, DM cannot be normal baryonic matter given that CMB data shows the baryon density in the universe to only account for $\sim$5% of the total energy density of the universe. Taking into account the previous constraints, this leaves the neutrino as the only possible SM candidate given that it is electrically neutral, carries no color charge, and has been shown to be massive. However, the most recent constraints on the neutrino mass set an upper limit of $m_\nu < 1.1$ eV, which corresponds to an energy density in the universe of about 0.1%. From Eq. 2.7, this value is far too small to account for the 26% total DM energy density in the universe as observed from CMB measurements. Therefore, any possible candidate for DM requires extension beyond the SM.

2.2.2 Weakly Interacting Massive Particles

Many different DM candidates from BSM theories have been proposed, including supersymmetric particles, sterile neutrinos, axions, and even hidden DM involving dark sectors which interact very weakly with the SM [53–59]. One of the most well-studied class of candidates are WIMPs, particles which have tree-level interactions with the W and Z bosons, have no electric or color charge, and have mass $m_{weak} \sim 10$ GeV-TeV on the weak scale. In addition to satisfying the constraints listed in Section 2.2.1, the predicted relic abundance of WIMPs in the early universe turns out to closely match the observed DM density from CMB observations, a coincidence known as the "WIMP miracle" [60, 61].

The production of WIMPs can be estimated by considering the thermal relic of the Big Bang [62]. In the early universe, when temperatures were extremely high, particles including WIMPs remained in thermal equilibrium, being annihilated and produced continuously. Eventually, as the universe expanded and cooled to temperatures below the WIMP mass m_χ, the production of WIMPs became exponentially suppressed, leading to a decrease in the WIMP density as they continued to annihilate. The WIMP decay rate during this period is given by the Boltzmann equation

$$\frac{dn}{dt} + 3H(T)n = -\langle \sigma v \rangle \left(n^2 - n_{\text{eq}}^2 \right) \tag{2.8}$$

where n is the number density of the WIMP, H is the Hubble parameter, $\langle \sigma v \rangle$ is the thermally averaged annihilation cross section, and n_{eq} is the WIMP number density at thermal equilibrium. Therefore, the WIMP number density decays exponentially as $e^{-m_\chi/T}$, which is shown in Fig. 2.5.

As the universe continued to expand and cool, WIMPs continued to decay until the WIMP interaction rate fell below the Hubble parameter, at which point the gas of WIMPs became too diluted to continue annihilating. After this point, the WIMP number density stopped changing significantly as the annihilation rate dropped to zero, a process known

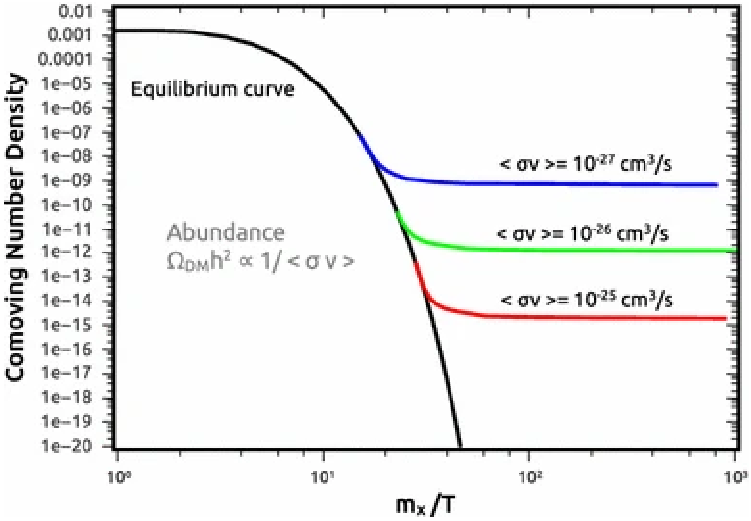

Figure 2.5: Evolution of comoving number density of WIMP as a function of the ratio of the WIMP mass m_χ and temperature T of the universe in the context of thermal freeze-out. The black line indicates the number density of a WIMP that remains in thermal equilibrium, while the red, green, and blue lines indicate scenarios for different values of the thermally averaged annihilation cross section $\langle \sigma v \rangle$. Figure taken from [63].

as "freeze out". This freeze out occurs when $n\langle \sigma v \rangle = H$, which gives a number density of

$$n_f \sim (m_\chi T_f)^{3/2} e^{-m_\chi/T_f} \sim \frac{T_f^2}{M_{\rm Pl}\langle \sigma v \rangle} \tag{2.9}$$

where the subscript f denotes quantities at freeze out and $M_{\rm Pl}$ is the Planck mass. Given a typical freeze out temperature of $T_f \sim m_\chi/20$, the WIMP thermal relic density is then given by

$$\Omega_\chi = \frac{m\chi n_0}{\rho_c} \sim \frac{x_f T_0^3}{\rho_c M_{\rm Pl}\langle \sigma v \rangle} \tag{2.10}$$

where ρ_c is the critical density, $x_f \equiv m_\chi/T_f$ and the subscript 0 denote present-day quantities. If the WIMP interacts with the SM on the weak scale through a heavier mediator with mass $m_{\rm med}$ and couplings to the WIMP and SM given by λ_χ and λ_f, respectively, then the WIMP cross section can be expressed

$$\langle \sigma v \rangle \sim \lambda_\chi^2 \lambda_f^2 \frac{m_\chi^2}{m_{\rm med}^4}. \tag{2.11}$$

Substituting the observed DM relic density from Eq. 2.7 into Eq. 2.10, one can numerically solve for the WIMP cross section to obtain

$$\langle \sigma v \rangle \sim 10^{-25} \mathrm{cm}^3 \mathrm{s}^{-1} \left(\frac{m_\chi}{100 \mathrm{GeV}} \right)^2 \left(\frac{1 \mathrm{TeV}}{m_{\mathrm{med}}} \right)^4 \lambda_\chi^2 \lambda_f^2 \tag{2.12}$$

which for suitable values of λ_χ and λ_f, predicts a WIMP mass in the range $m_\chi \sim 100$ GeV-TeV. Therefore, the WIMP miracle refers to the observation that to account for the observed DM relic density requires, WIMP cross sections and masses are predicted to both be on the weak scale given a typical freeze out temperature $T_f \sim m_\chi/20$. As a result, many different WIMP models have been proposed to explain DM, which will be further explored in Chapter 5.

2.3 Dark matter searches

In order to investigate possible WIMP models, searches need to be performed to look for DM. Efforts to detect DM generally fall under three main approaches depending on the signature of DM being measured:

- **Direct detection**: this approach involves experiments like XENON [64], LUX-ZEPLIN [65], and PandaX [66] that are designed to detect rare collisions between DM and atomic nuclei. The signal consists of nuclear recoils of SM particles produced from the elastic scattering of DM particles.

- **Indirect detection**: this approach involves experiments like Fermi-LAT [67] and AMS-02 [68] which are designed to observe the products of DM annihilation and decay, producing SM final products such as gamma rays positrons, and neutrinos.

- **Collider searches**: this approach involves colliders like the LHC which attempt to produce DM particles directly through the collision of SM particles like protons. Since these colliders cannot measure the presence of DM particles directly, DM signatures are usually studied in processes where DM is produced in association

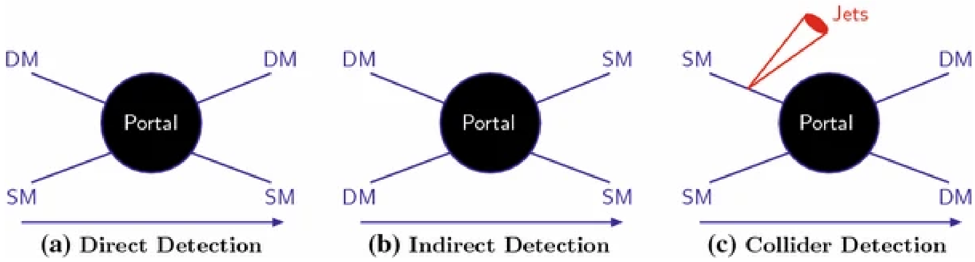

Figure 2.6: Schematic representation of the different types of experimental approaches that can be used to search for DM based on the interactions of DM with SM particles. Figure taken from [63].

with other SM signatures like hadronic jet showers.

Each of these approaches to searching for DM has its own advantages and limitations. For example, in the case of collider searches, any measurement of a DM signature cannot constrain the DM lifetime beyond the time it takes for the particle to escape, which is on the order of about 10^{-7} s. Therefore, to validate that the detected candidate is truly stable on timescales of the universe's lifetime, other experiments from direct and indirect detection are required to make sure the candidate satisfies cosmological DM constraints. Thus, any DM measurement made by collider searches cannot be directly interpreted as a discovery of DM without similar results through direct and indirect detection experiments.

It is important to note, though, that these approaches are complementary to each other and are all required to fully investigate the properties of DM [69]. For example, direct and indirect detection experiments can probe relic particle DM that would give insight to properties of DM halos and constrain properties of new DM particle measurements, while collider experiments can directly study DM production that would instead provide insight into DM interactions in the early universe. In addition, different methods are sensitive to different regions of parameter space covered by WIMP models, including low energy regimes all the way up to higher relativistic regimes. Figure 2.7 showcases the parameter space covered for classic WIMP models in terms of the DM mass and coupling strength by different frontiers of experiments, as well as the extension of this coverage to other DM models like vector-portal, sterile neutrino, axion-like and macroscopic DM models.

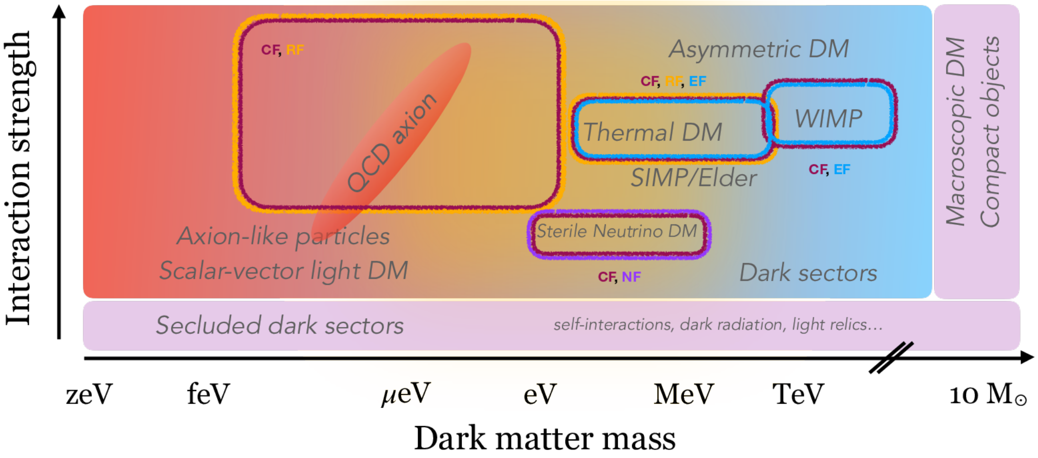

Figure 2.7: Summary of the parameter space covered by different DM detection approaches in terms of the coupling strength and DM mass. DM models like vector-portal, sterile neutrino, axion-like, and macroscopic DM models are included in addition to the classic minimal WIMP paradigm highlighted by the rounded rectangles. The shaded colors in the sketch are suggestive of the different experimental frontiers represented in the case studies in a given region: Cosmic Frontier (CF), Energy Frontier (EF), Rare and Precision Frontier (RF), and Neutrino Frontier (NF). Figure taken from [69].

2.3.1 Direct detection

The goal of direct detection experiments is to measure the nuclear recoil from the scattering of a WIMP particle. The scattering rate will depend on the local density and velocity distributions of WIMPs in the Milk Way, the WIMP mass, and the interaction cross section of the target nuclei. The differential cross section for WIMP-nucleus scattering is given by

$$\frac{d\sigma}{dE} = \frac{m_N}{2\mu^2 v^2}(\sigma^{SI} F^2(q) + \sigma^{SD} S(q)) \tag{2.13}$$

where m_N is the target nucleus mass, $\mu = m_\chi m_N/(m_\chi + m_N)$ is the WIMP-nucleus reduced mass, v is the velocity of DM with respect to the nucleus, σ^{SI} and σ^{SD} are the Spin-Independent (SI) and Spin-Dependent (SD) cross sections, and $F^2(q)$ and $S^2(q)$ are their respective form factors as defined in [60, 70–72].

Since WIMPs only interact weakly with SM particles, it is possible for WIMPs from space to pass through Earth and interact with atomic nuclei. However, these processes are expected to be extremely rare, with typical theoretical models predicting an interaction cross section of less than 10^{-42} cm^2 for almost all possible WIMP masses. As a result, the expected signal rate is extremely small, which requires methods to suppress residual background for signal detection to be possible. This background suppression is achieved through placing the experiment in deep underground laboratories to reduce noise from neutrons and gamma rays from the environment. Direct detection experiments are usually limited by uncertainty coming from neutrino-nucleus scattering, which comes from solar and atmospheric neutrinos that are difficult to suppress. However, even with these limitations, current direct detection experiments can place tight constraints on various WIMP models.

From Eq. 2.13, direct detection experiments can be separated into two categories: SI measurements and SD measurements. Since the cross section of SI measurements are proportional to the square of the mass of the target nuclei, experiments targeting SI cross section measurements use heavy nuclei like xenon to enhance sensitivity to DM. SI measurements are also sensitive to a larger range of WIMP masses compared to SD measurements, which allow both low and high mass WIMPS to be probed. In addition, many WIMP models involve DM candidates like neutralinos [53] that are predicted to have SI interactions with the SM, so SI measurements are also important in constraining these models. The current best limits on the SI WIMP-nucleon cross section set by the LUX-ZEPLIN experiment are shown in Figure 2.8, excluding cross sections above 9.2×10^{-48} cm^2 for WIMPs with a mass of 36 GeV/c^2 [65]. Limits are also shown for other SI direct detection experiments including PandaX-4T [73], XENON1T [64], LUX [74], and DEAP-3600 [75].

On the other hand, since SD measurements depend on the spin structure of the target nucleus, they are more sensitive to nuclei with unpaired protons and neutrons like hydrogen and fluorine that can interact with DM via spin-dependent forces. SI measurements are also important for testing WIMP models that predict axial-vector couplings such as models involving a new Z' gauge boson [76]. In addition, SI measurements are complementary to SD measurements as they are more sensitive to lower mass WIMPs and can target WIMP-

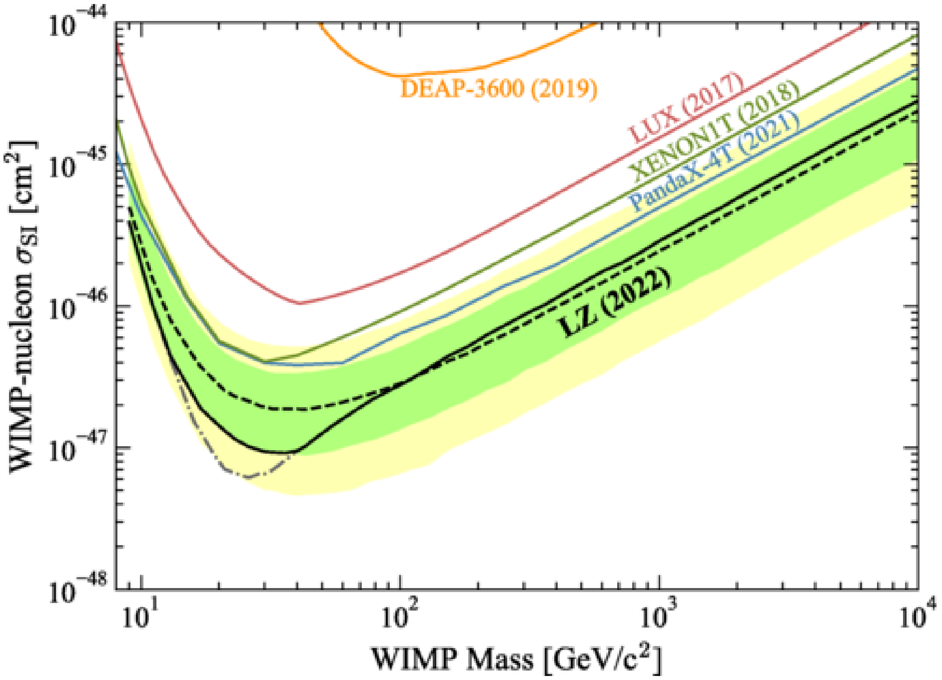

Figure 2.8: The 90% confidence limit (black line) for the SI WIMP scattering cross section on neutrons as a function of WIMP mass from the LUX-ZEPLIN experiment. The green and yellow bands show the 1σ and 2σ sensitivity bands. The dotted line shows the median of the sensitivity projection. 90% confidence limits are also shown for the PandaX-4T, XENON1T, LUX, and DEAP-3600 experiments. Figure taken from [65].

neutron and WIMP-proton couplings separately. The current best limits on SD WIMP-proton cross sections set by the PICO-60 C_3F_8 detector are shown in Fig. 2.9, excluding cross sections above 3.4×10^{-41} cm^2 for WIMPs with a mass of 25 GeV/c^2. Limits are also shown for other SD direct detection experiment including PICO-60 CF_3I [77], PICO-2L [78], PICASSO [79], SIMPLE [80], PandaX-II [66], IceCube [81], and Super-Kamiokande [82, 83].

2.3.2 Indirect detection

Unlike direct detection experiments, indirect detection experiments aim to measure solely SM particles that are the byproducts of WIMP annihilation or decay over expected background. These byproducts include gamma rays, positrons, neutrinos, and antiprotons, and can be detected by astrophysical observatories and neutrino detectors. Indirect detection

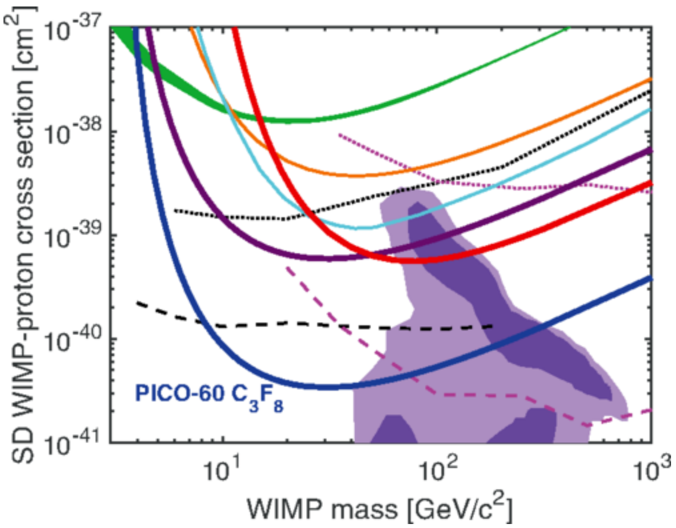

Figure 2.9: The 90% confidence limit (thick blue line) for the SD WIMP scattering cross section on protons as a function of WIMP mass from the PICO-60 C_3F_8 detector. Limits are also shown for the PICO-60 CF_3I (thick red), PICO-2L (thick purple), PICASSO (green band), SIMPLE (orange), PandaX-II (cyan), IceCube (dashed and dotted pink), and Super-Kamiokande (dashed and dotted black) experiments. The purple region represents parameter space of the constrained minimal supersymmetric model of Ref. [84]. Figure taken from [85].

experiments probe complementary properties of WIMPs compared to direct detection experiments since they are sensitive to how DM is distributed, the annihilation cross section of DM today compared to in the early universe, and to the WIMP mass. In addition, if the annihilation cross section for DM is not velocity dependent, then bounds on the current annihilation cross section can be directly connected to the DM relic density. For example, stringent limits on the plane of the annihilation cross section versus WIMP mass can be set by observation of gamma-ray measurements which can be produced by DM annihilation. If annihilation cross sections above 10^{-26} cm^{3}s^{-1} are excluded for WIMP masses below 100 GeV, then the correct relic density cannot be reproduced by the method described in Section 2.1.3. Thus, constraints set by indirect detection experiments can also be complementary to constraints set by the observed DM relic density from CMB measurements.

Current indirect detection experiments look for various signatures of DM annihilation or decay. Experiments like Fermi-LAT [67], HESS [86], and CTA [87] look for excesses in gamma rays produced from WIMP annihilation in regions where the density of DM is expected to be high. These regions include the center of the Milky Way, dwarf spheroidal galaxies with low levels of visible matter, galaxy clusters, and the halo of the Milky Way. Other experiments like IceCube [88], Super-Kamiokande [89], and ANTARES [90] instead look for high energy neutrinos produced by WIMP annihilation from inside the Sun or near the center of the Milk Way. Finally, AMS-02 [68] is an experiment designed to measure excess cosmic rays of antimatter like positrons and antiprotons produced from DM annihilation. Figure 2.10 shows the current sensitivity of the IceCube experiment to the thermally averaged cross section of DM annihilation into $\nu_e\overline{\nu}_e$ in comparison to previous IceCube results [91–93], as well as the Super-Kamiokande [89] and ANTARES [94].

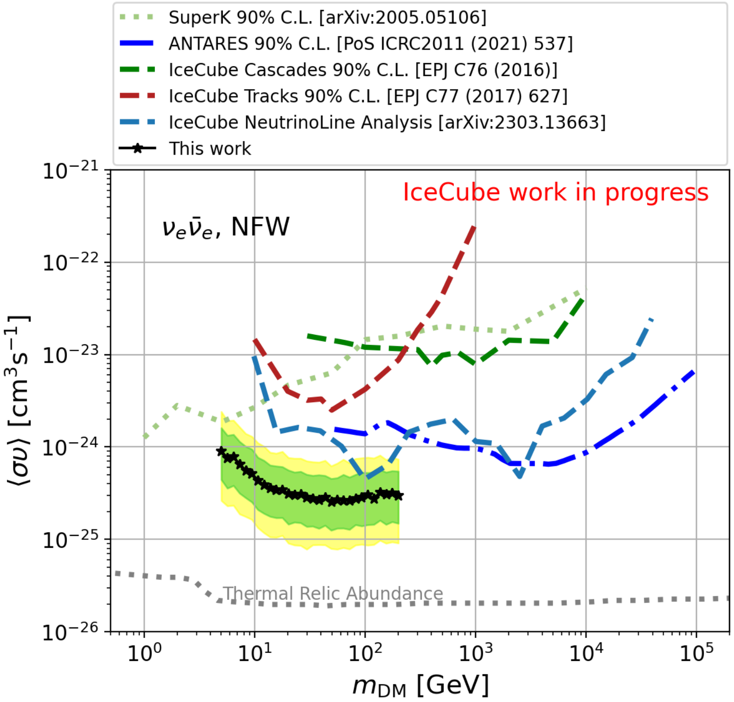

Figure 2.10: Sensitivity of the thermally averaged cross section of the $\nu_e\overline{\nu}_e$ channels for DM annihilation compared to previous IceCube results, as well as Super-Kamiokande and ANTARES. The green and yellow bands represent 1σ and 2σ uncertainties. The dotted grey line is the cross section required to produce the observed DM relic abundance from thermal freeze out computed in Ref. [95]. Figure taken from [88].

2.3.3 Collider searches

The main advantage of looking for DM in colliders is the possibility to produce DM directly in the lab rather than relying on rare natural processes. Depending on the theoretical model considered, DM can be produced in association with other SM particles like leptons, photons, and QCD jets resulting from the hadronization of heavy flavor quarks. Since WIMPs do not interact with the electromagnetic or strong force, their presence at colliders cannot be directly measured. Instead, their presence is inferred from missing momentum balanced by the other visible particles produced (see Section 4.7). Neutrinos are also electrically neutral and do not interact with the strong force, making them difficult to detect as well and potentially contribute to missing momentum in the collider. However, by selecting events with large missing momentum, one can reduce the SM background in order to potentially disentangle the DM signal.

Although detection of DM signals at colliders cannot constrain the lifetime of the particle beyond the order of 10^{-7} s, they still provide a complementary search strategy to identifying WIMPs in combination with other detector experiments and cosmological constraints. In particular, searches for events with large missing momentum can be used to derive strict constraints on WIMP-nucleon scattering cross sections that can be compared to those derived from direct and indirect measurements [96–103]. At the LHC, both the CMS and ATLAS collaborations have performed searches for the production of DM in association with QCD jets and other SM particles, known as Mono-X searches, that have set various constraints on WIMP models [104, 105]. In addition, searches for invisible decay of the Higgs and Z boson to WIMPs have also been performed [106, 107]. The WIMP models considered in these searches usually focus on a spin-1 or spin-0 mediator in the context of an effective field theory (EFT) or simplified model in which the interaction of DM with the SM is governed by a small number of free parameters. As a result, constraints on many different types of models can be set depending on the final signature being considered in the search. More details of the specific model covered by the DM analysis described in this thesis will be presented in Section 5.1.

Chapter 3

Experimental Apparatus

This chapter describes the experimental apparatus used in the search for DM, which was the Compact Muon Solenoid (CMS) detector at the Large Hadron Collider (LHC). Section 3.1 provides a brief overview of the LHC, while Section 3.2 describes the CMS detector as well as its different components and related subsystems. In particular, Section 3.2.9 describes the SWATCH system, whose Level-1 Calorimeter subsystem I was responsible for.

3.1 The Large Hadron Collider

The LHC [108] is a large particle accelerator located at the European Organization for Nuclear Research (CERN) near Geneva, Switzerland. As the world's most powerful particle accelerator, it is primarily designed to collide protons at a center-of-mass (COM) energy of 14 TeV, though it can also produce heavy ion collisions such as lead (PbPb) and xenon (XeXe) collisions. The goal of the LHC was to rigorously test predictions of the SM, which included the discovery of the Higgs boson in 2012 [18–20], and to search for BSM physics such as dark matter.

It is composed of a chain of smaller particle accelerators and is installed in a 26.7 km tunnel originally constructed for the CERN Large Electron Positron (LEP) machine, situated between 45 and 170 m beneath the French-Swiss border near Geneva. In order to produce high energy proton collisions, hydrogen gas is initially ionized to create protons which are then accelerated up to 160 MeV by the Linear Accelerator 4 (LINAC4). These protons are then further accelerated up to 2 GeV after being injected into the Proton Synchrotron Booster (PSB), which then transfers the protons to the Proton Synchrotron (PS) to accelerate them to 26 GeV. These protons are then injected into the Super Proton Synchrotron (SPS) in order to boost the energy of the protons to 450 GeV before entering the main LHC ring. The main LHC ring consists of two separate rings which accelerate the protons in opposite directions using superconducting radiofrequency (RF) cavities operating at 400 MHz, bringing the protons up to a final energy of 6.5 TeV. In addition, superconducting dipole magnets operating at a temperature of 1.9 K and producing a magnetic field of 8.3 T are used to maintain the protons in circular orbit.

The proton beams in the two separate rings are then focused using quadrupole magnets before colliding at designated interaction points (IPs) in bunches containing 10^{11} protons each, with an inter-bunch distance of 25 ns (or 40 MHz). Several large detectors are installed at the IPs corresponding to the four major experiments at LHC:

- Compact Muon Solenoid (CMS) [109, 110]: a general-purpose detector built around a huge soleonid magnet that is designed to make SM precision measurements and search for new physics like dark matter.
- A Toroidal LHC Apparatus (ATLAS) [111]: another general-purpose detector to complement CMS.
- A Large Ion Collider Experiment (ALICE) [112]: a heavy ion detector designed to study the quark-gluon plasma.
- Large Hadronic Collider beauty (LHCb) [113]: a series of subdetectors designed to study the bottom quark.

A schematic overview of the LHC complex, including the injection chain, the LHC ring, and the experiments at the IPs, is shown in Fig. 3.1.

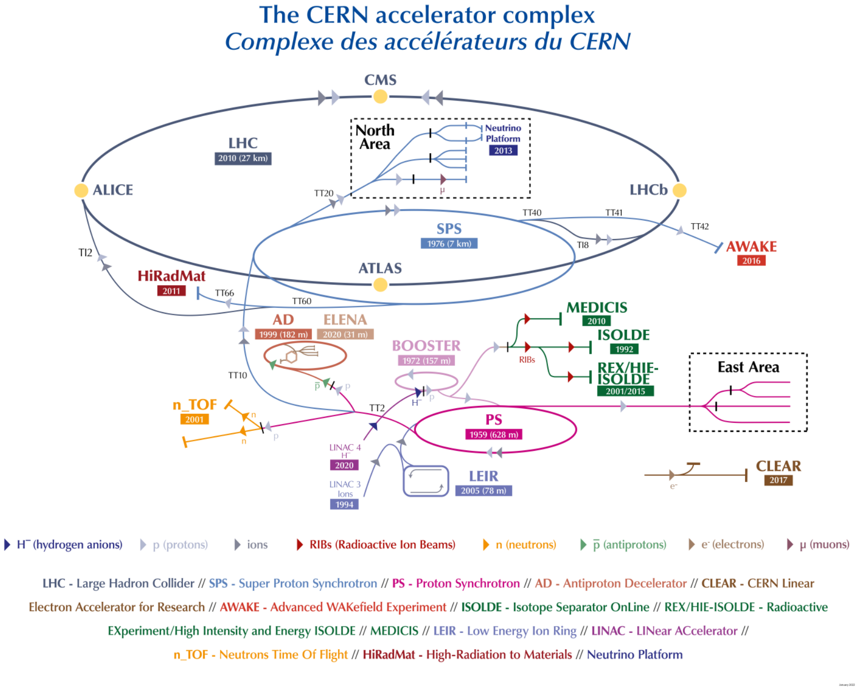

Figure 3.1: Schematic overview of the LHC complex, including the injection chain, the LHC ring, and the experiments at the interaction points. Figure taken from [114].

Particles produced by proton-proton collisions at the LHC can be divided into two classes based on the type of scattering process that produced the particle. Soft particles are particles produced by soft scattering where only a small amount of the initial momentum of the protons is transferred to the particle, resulting in particles that are scattered at small angles with respect to the beam axis. Hard particles, on the other hand, are particles produced by hard scattering where a large amount of momentum is exchanged from the colliding protons. A key signature of hard scattering is the production of particles with high transverse momentum. For these signatures, conservation of momentum in the transverse direction can be applied to infer the presence of particles that cannot be directly measured by the detector (see Section 4.7).

The number of events per second, N_{event}, generated by the proton-proton collisions in the LHC is given by

$$N_{\text{event}} = L\sigma_{\text{event}}, \tag{3.1}$$

where σ_{event} is the cross section for the event and L is the instantaneous luminosity of the beam. The instantaneous beam luminosity itself depends only on the beam parameters and is given by

$$L = \frac{N_b^2 n_b f_{\text{rev}} \gamma_r}{4\pi \epsilon_n \beta *} F \tag{3.2}$$

assuming a Gaussian beam distribution, where N_b is the number of particles per bunch, n_b is the number of bunches per beam, f_{rev} is the revolution frequency, γ_r is the relativistic gamma factor, ϵ_n is the normalized transverse beam emittance, $\beta *$ is the beta function at the collision point, and F is the geometric luminosity reduction factor due to the crossing angle at the IP of the beam. The factor F accounts for the fact that a larger crossing angle at the IP results in a lower effective luminosity because of the reduction of overlap between the beams in the transverse plane. It is given by

$$F = \left(1 + \left(\frac{\theta_c \sigma_z}{2\sigma *}\right)^2\right)^{-1/2} \tag{3.3}$$

assuming round beams with equal beam parameters for both beams, where θ_c is the full crossing angle at the IP, $\sigma_z \ll \beta$ is the RMS bunch length, and $\sigma *$ is the transverse RMS beam size at the IP. For proton-proton collisions, the LHC is designed to reach a nominal instantaneous luminosity of up to $L = 10^{34}$ cm^{-2}s^{-1}, and has achieved a peak instantaneous luminosity of around twice the nominal value.

Data taking at the LHC can be separated into distinct eras, starting with Run 1 (2010–2013) at a COM energy of 7 TeV in 2010 which was increased to 8 TeV in 2012, during which the Higgs boson was discovered. Upgrades to the detectors and maintenance were then performed during Long Shutdown 1 (LS1) from 2013–2015, after which Run 2 (2015–2018) of data taking started at a COM energy of 13 TeV. After Run 2, further upgrades and maintenance of the detectors were performed during Long Shutdown 2 (LS2) from 2019–2021 to prepare the LHC for higher luminosities. Currently, Run 3 (2022–2026) data taking is ongoing at a COM energy of 13.6 TeV, after which upgrades for the High-Luminosity LHC (HL-LHC) project will be performed during Long Shutdown 3 (LS3)

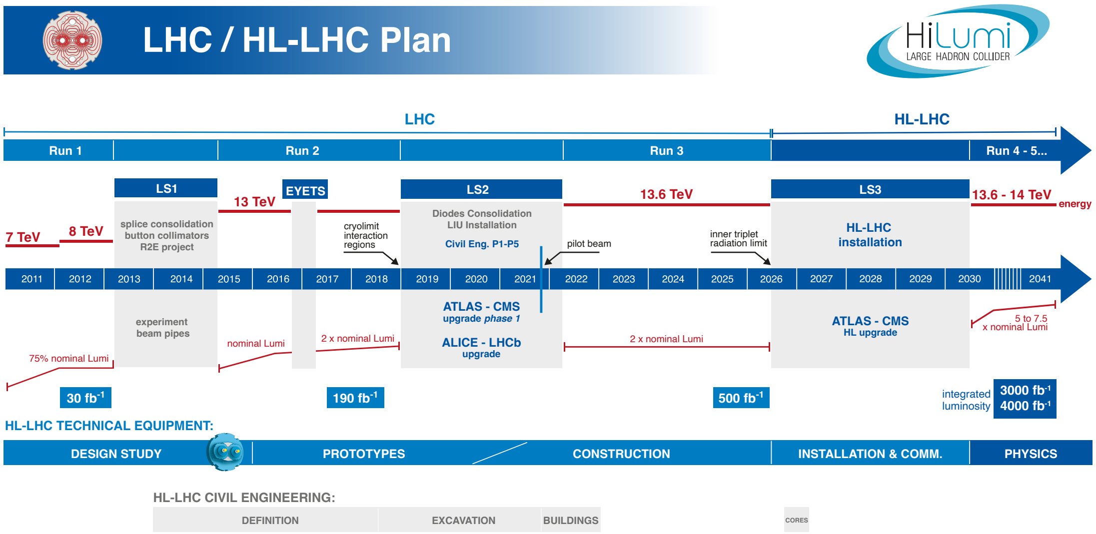

Figure 3.2: Illustration showing the different eras of data taking and shutdowns at the LHC, including the future proposed HL-LHC project. The total integrated luminosity since the start of data taking at the LHC up to the end of various data taking eras are also shown. Figure taken from [115].

from 2026-2030. The HL-LHC aims to increase data collected by the LHC by a factor of 10 and is expected to start data taking by 2030 at a COM energy of 13.6–14 TeV. These separate eras of data taking can also be classified into different phases: Phase 1, which covers data taking up to Run 3, and Phase 2, which will cover data taking at the HL-LHC. An illustration of the different phases of data taking at the LHC is shown in Fig. 3.2.

The total amount of data produced by the LHC can be quantified by what is known as the total integrated luminosity $\mathcal{L} = \int L(t)dt$, which represents the integrated luminosity over a period of time. Along with the increase in COM energy, each subsequent era of data taking has also delivered higher total integrated luminosity. For example, during Run 1 and 2, the LHC delivered approximately 30 fb^{-1} and 160 fb^{-1} of data, respectively, while for Run 3, the LHC is expected to deliver around 300 fb^{-1} of data. Of this data, the amount that was actually recorded by CMS and certified for good physics analyses corresponds to a total integrated luminosity of 27 fb^{-1} and 138 fb^{-1} during Run 1 and 2, respectively. The cumulative total integrated luminosity recorded by the LHC and

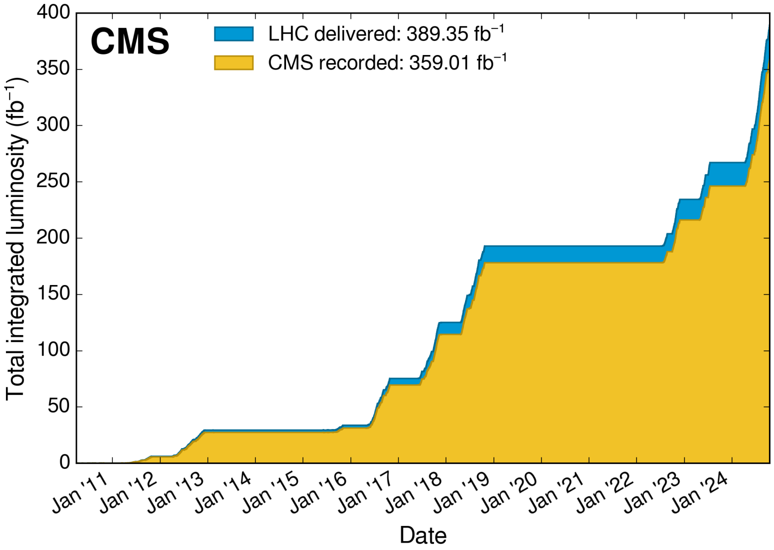

Figure 3.3: Cumulative total integrated luminosity versus time for 2010–2012, 2015–2018, and 2022–2023 for *pp* collisions delivered by the LHC and recorded by CMS. Figure taken from [116].

delivered to CMS are shown in Fig. 3.3.

3.2 The Compact Muon Solenoid detector

The CMS detector is a multipurpose apparatus designed to study a wide range of physics, from precision SM measurements to searches for new BSM physics. As the name implies, it is designed around a large superconducting solenoid that can generate up to a 3.8 T magnetic field. Surrounding the magnet are several concentric layers of subdetector systems, each dedicated to measuring the energy and momenta of different types of particles. The innermost layer around the magnet is the inner tracking system, which is designed to measure the trajectories of charged particles from their bending in the magnetic field. Beyond that is the electromagnetic calorimeter (ECAL) designed to identify electrons and photons. After the ECAL comes the hadron calorimeter (HCAL), which is designed to identify hadronic particles. Finally, the outermost layer is the muon system, which consists of a series of subdetectors dedicated to identifying muons. In addition, there is also

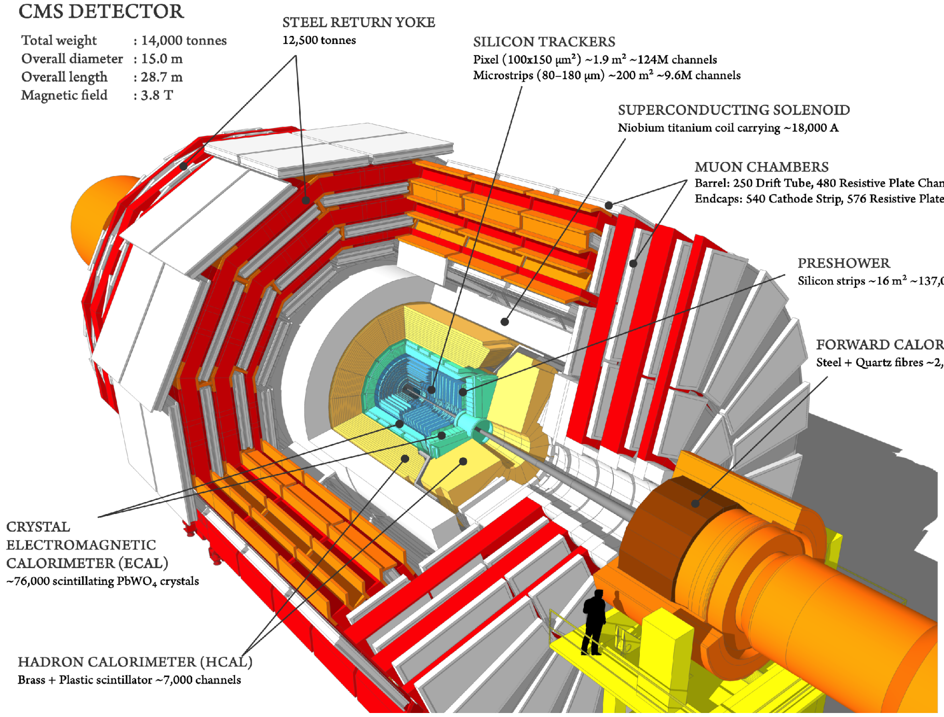

Figure 3.4: Schematic overview of the CMS detector, showing the different subcomponents and subdetector systems. Figure taken from [117].

a two-tier trigger system to filter the events and process the data collected, A schematic overview of the CMS detector is shown in Fig. 3.4.

3.2.1 Coordinate conventions

For the coordinate system of CMS, the origin is defined to be the center of the detector where the nominal collision point occurs, with the y-axis pointing vertically upwards and the x-axis pointing radially inwards towards the center of the LHC ring. The z-axis is then defined to point along the beam direction anticlockwise from above. The azimuthal angle ϕ is measured in the $x-y$ plane, while the polar angle θ is measured from the $z-$ axis and is used to define the pseudorapidity which is given by

$$\eta = -\ln\tan(\theta/2). \tag{3.4}$$

Since particles produced at the LHC tend to be highly relativistic, Lorentz invariance of measured quantities is important because quantities measured by the detectors may not necessarily be the same as quantities measured in the rest frame of the collision that produced these particles. Thus, η is a useful quantity to measure because for highly relativistic particles where the mass of the particle is negligible compared to its momentum ($m \ll p$), such as those found during proton-proton collisions at the LHC, η converges to the rapidity y given by

$$y = \frac{1}{2} \ln \left(\frac{E + p_z}{E - p_z} \right), \tag{3.5}$$

where E is the energy of the particle and p_z is the magnitude of its momentum along the beam direction. Since y is invariant under Lorentz boosts along the beam direction, η is also approximately invariant under Lorentz boosts along the beam direction for highly relativistic particles. Other quantities that are also invariant under Lorentz boosts along the beam direction include the measured transverse momentum ($\mathrm{p_T}$) and energy ($\mathrm{E_T}$), which are computed from the x and y components, as well as the imbalance of momentum measured in the transverse plane $\mathrm{p_T^{miss}}$. A schematic overview of the CMS coordinate system is shown in Fig. 3.5.

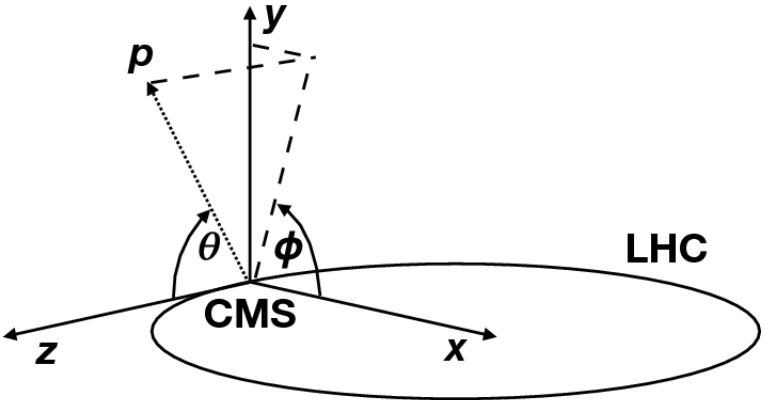

Figure 3.5: Illustration of the coordinate system as defined at CMS relative to the LHC. Figure taken from [118].

3.2.2 Magnet

The magnetic field in the CMS detector is generated by a large but thin solenoid coil with a diameter of 6 m and a length of 12.5 m. The solenoid is composed of a niobium-titanium (NbTi) alloy which becomes superconducting at very low temperatures. The solenoid is kept cooled at a temperature of 1.9 K using liquid helium, and can generate a central magnetic flux density of 3.8 T. In order to contain and redirect the magnetic field back through the coil in a closed loop, an iron return yoke weighing about 10,000 tons surrounds the solenoid.

The high magnetic flux density generated by the CMS magnet is necessary for providing an accurate measurement of the momenta of charged particles in the detector. A map of the value of the magnetic flux density in a longitudinal section of the CMS detector is shown in Fig. 3.6. Of the magnetic flux generated by the solenoid, about two thirds pass through the cross sections of the return yoke while the remaining third creates a stray magnetic field around the yoke. For example, at a radius of 50 m from the coil axis in the central plane of the detector, the magnetic flux density is 2.1 mT, while at a distance of 50 m from the center of the solenoid along its axis, the magnetic flux density is 0.6 mT. Nonetheless, most of the subdetectors in CMS are contained within the 3.8 T magnetic field generated by the solenoid magnet.

3.2.3 Inner tracking system

The inner tracking system of CMS surrounds the interaction point (IP) with a length of 5.8 m and a diameter of 2.5 m and is designed to provide precise and efficient measurements of the trajectories of charged particles in the magnetic field of the detector. A schematic cross section of the inner tracking system is shown in Fig. 3.7. It is composed of a pixel detector with three barrel layers with radii between 4.4 cm and 10.2 cm along with a silicon strip tracker with 10 barrel detection layers extending outwards to a radius of 1.1 m. Each of these detectors are also surrounded by endcap disks which extend the acceptance of the tracker up to a pseudorapidity of $|\eta| < 2.5$. In total, the inner tracking system is

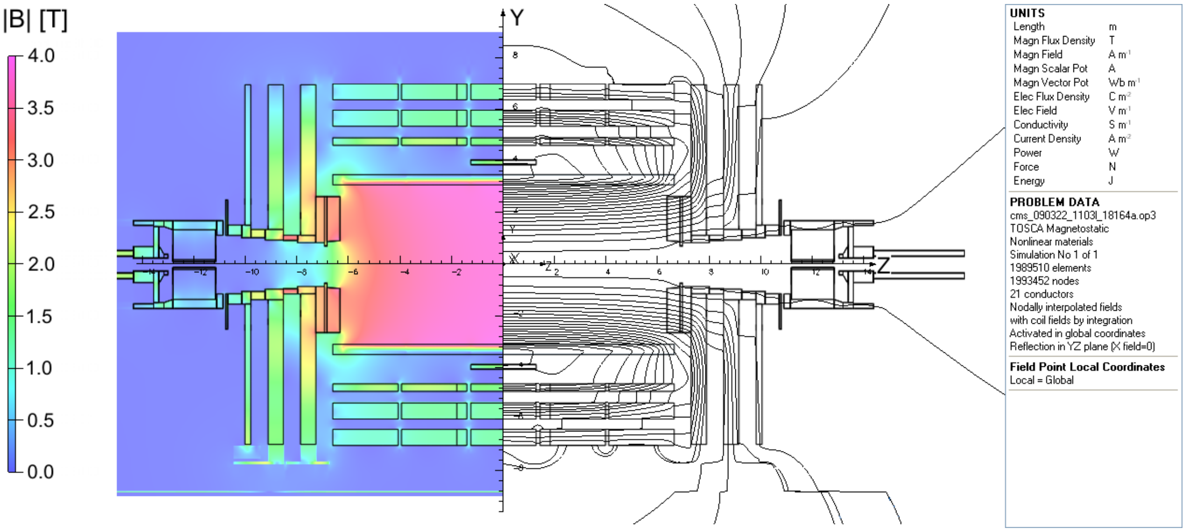

UNITS

Length	m
Magn Flux Density	T
Magn Field	$\mathrm{A\,m^{-1}}$
Magn Scalar Pot	A
Magn Vector Pot	$\mathrm{Wb\,m^{-1}}$
Elec Flux Density	$\mathrm{C\,m^{-2}}$
Elec Field	$\mathrm{V\,m^{-1}}$
Conductivity	$\mathrm{S\,m^{-1}}$
Current Density	$\mathrm{A\,m^{-2}}$
Power	W
Force	N
Energy	J

PROBLEM DATA
cms_090322_1103l_18164a.op3
TOSCA Magnetostatic
Nonlinear materials
Simulation No 1 of 1
1989510 elements
1993452 nodes
21 conductors
Nodally interpolated fields
with coil fields by integration
Activated in global coordinates
Reflection in YZ plane (X field=0)

Field Point Local Coordinates
Local = Global

Figure 3.6: Value of the magnetic flux density magnitude $|B|$ (left) and field lines (right) on a longitudinal section of the CMS detector for a central magnetic flux density of 3.8 T. Each fieldline represents a magnetic flux increment of 6 Wb. Figure taken from [119].

composed of around 1850 pixel and 15,000 strip detector modules. Each of these detector modules are composed entirely of silicon in order to meet the high radiation tolerance and performance constraints necessary in the CMS detector.

The pixel detector is located closest to the IP and is used to reconstruct primary and secondary vertices of the collision with a total of 124 million readout channels. The three barrel layers are located at a mean radii of 4.4 cm, 7.3 cm, and 10.2 cm, with a length of 53 cm. The two endcap disks extend from 6 to 15 cm in radius and are placed on each side of the detector at $|z = 34.5$ cm and 46.5 cm. The spatial resolution of the pixel detectors is about 10 μm in the $r - \phi$ plane and about 20 μm along the $z-$axis.

The barrel region of the silicon strip detector is divided into two parts, the Tracker Inner Barrel (TIB) and the Tracker Outer Barrel (TOB). The TIB is made up of 4 layers and covers up to $|z| < 65$ cm using silicon sensors with a thickness of 320 μm and a strip pitch which varies from 80 to 120 μm. The TOB is composed of 6 layers with a half-length of $|z| < 110$ cm, where thicker 500 μm silicon sensors are used since the radiation levels are smaller compared to the inner barrel region. The endcap disks are also divided into two parts, the Tracker End Cap (TEC) and the Tracker Inner Disks (TID). Each TEC

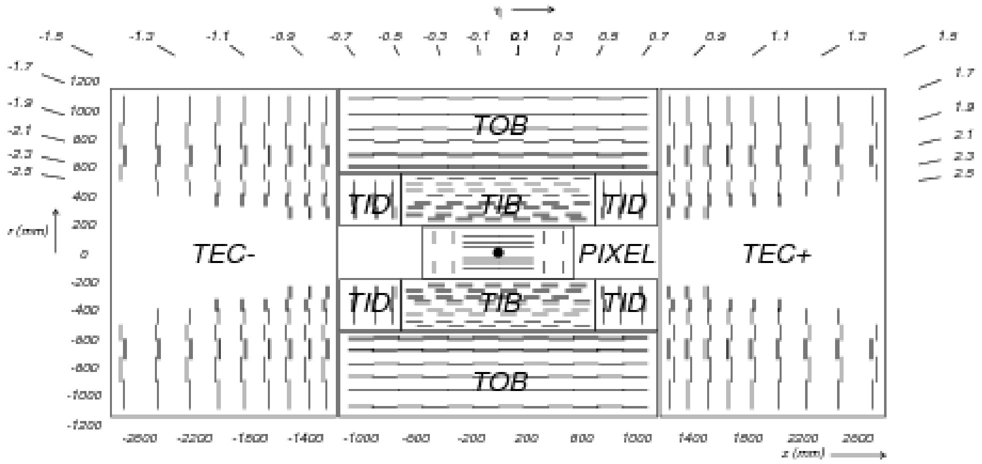

Figure 3.7: Schematic cross section of the CMS inner tracking system in the $r-z$ plane. Each line element represents a detector module, while closely space double line elements indicate back-to-back silicon strip modules. Figure taken from [109].

is composed of 9 disks extending into the region 120 cm $< |z| <$ 280 cm, and each TID is composed of 3 small disks situated in the gap between the TIB and the TEC. The silicon strip detectors have a spatial resolution between 35 μm and 52 μm depending on the direction.

3.2.4 Electromagnetic calorimeter

The ECAL is a hermetic, homogeneous calorimeter comprised of 61200 lead tungstate ($PbWO_4$) crystals mounted in the central barrel and closed by 7324 crystals in each of the 2 endcaps. A preshower detector is also placed in front of the endcap crystals. It is specifically designed to measure the energy of electrons (e) and photons (γ), both of which can produce a cascade of secondary particle showers through a combination of bremsstrahlung ($e \to e\gamma$) and photon pair production ($\gamma \to e^+e^-$). These showers are characterized by the radiation length X_0, the mean distance the electron travels after having its energy reduced by a factor of e from electromagnetic interactions with the detector. The energies of these particle showers are then measured by the scintillation light produced as these particles pass through the $PbWO_4$ crystals with avalanche photodiodes (APDs) in the barrel and

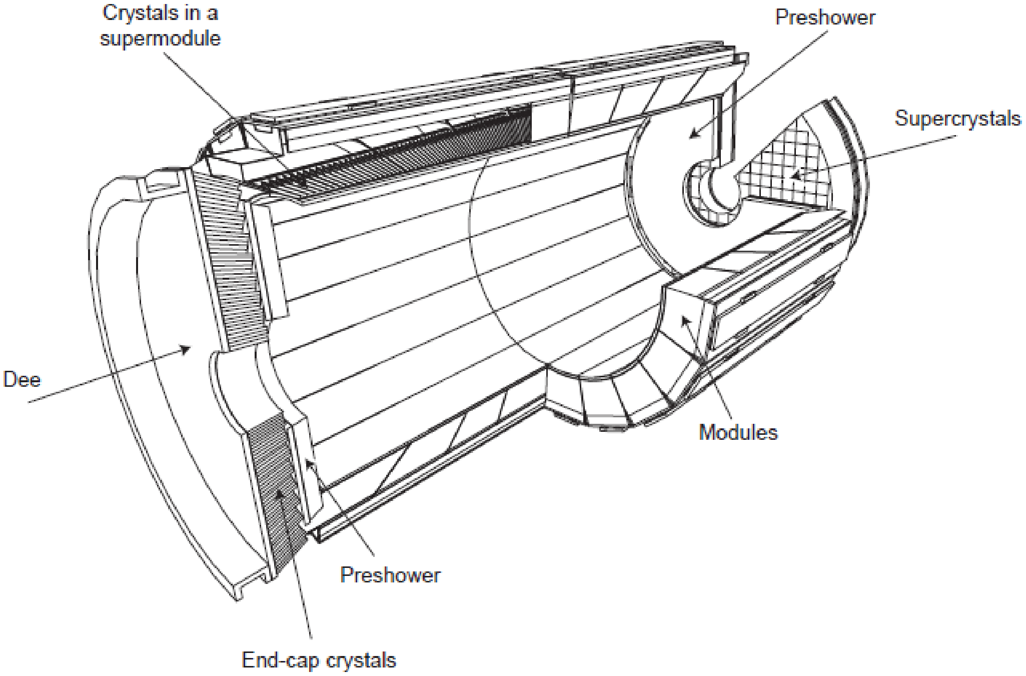

Figure 3.8: Layout of the ECAL showing the arrangement of the subcomponents, including the modules, supermodules, endcaps, and preshower. Figure taken from [109].

vacuum phototriodes (VPTs) in the endcap regions. The properties of the $PbWO_4$ crystals make them ideal for use in the ECAL, with their high density (8.28 g/cm^3), short radiation length ($X_0 = 0.89$ cm), small Molière radius (2.2 cm), and short scintillation decay time (80% of the light emitted in 25 ns).

The layout of the different components of the ECAL is shown in Fig. 3.8. The barrel section (EB) is composed of 35 identical supermodules, with an inner radius of 129 cm that covers half the barrel length and corresponding to a pseudorapidity range of $0 < |\eta| < 1.479$. The length of each crystal is 230 mm corresponding to $25.X_0$, and they are mounted in a quasi-projective geometry to avoid cracks aligned with particle trajectories. The endcaps section (EE) is located 3.14 cm from the IP and covers a pseudorapidity range of $1.479 < |\eta| < 3.0$. It is comprised of groups of 5x5 crystals, each with a length of 220 mm ($24.7X_0$), arranged in a rectangular grid in the $x - y$ plane.

The energy resolution of the ECAL is given by [110]

$$\left(\frac{\sigma}{E}\right)^2 = \left(\frac{S}{\sqrt{E}}\right)^2 \oplus \left(\frac{N}{E}\right)^2 \oplus C^2, \tag{3.6}$$

where E is the total energy of the particle, S is a stochastic term, N represents noise in the detector, and C is a constant term. For typical beam test conditions, the value of these parameters are $S = 3.63$, $N = 124$ MeV, and $C = 0.26$, corresponding to an energy resolution between 0.4% and 1.5% for energies in the range 10–250 GeV.

3.2.5 Hadron calorimeter

The HCAL is a series of alternating layers of absorbing plates and active material that surrounds the ECAL, which includes the hadron barrel (HB), hadron endcap (HE), hadron outer (HO), and hadron forward (HF) detectors. It is designed to measure the energy and momentum of hadrons such as protons, neutrons, and pions which penetrate the ECAL. Like photons and electrons, hadrons can also interact with the detector material to produce showers of secondary particles. However, unlike electromagnetic showers, hadronic showers are more widespread and longer in length. These showers are characterized by the nuclear interaction length λ_I, which is the mean free path of the hadron traveling through the detector before it interacts with a nucleus. Once a hadron enters the HCAL, it will interact with the absorbing plates and create hadronic showers which then interact with active material to produce light from either scintillation (HB, HE, HO) or Cherenkov radiation (HF). This light is then amplified and readout by multi-channel hybrid photodiodes (HPDs).

A schematic view of one quadrant of the HCAL is shown in Fig. 3.9. Both the HB and HE detectors are composed of alternating layers of brass plates and scintillator tiles. Brass is used for the absorber material since it has a relatively short interaction length ($\lambda_i = 16.42$ cm), is easy to machine, and is non-magnetic. The HB detector is constructed of 2 half barrels consisting of 32 towers in η that cover the pseudorapidity region of $-1.4 < |\eta| < 1.4$ for a total of 2304 HB towers, while the HE detector consists of 14 towers

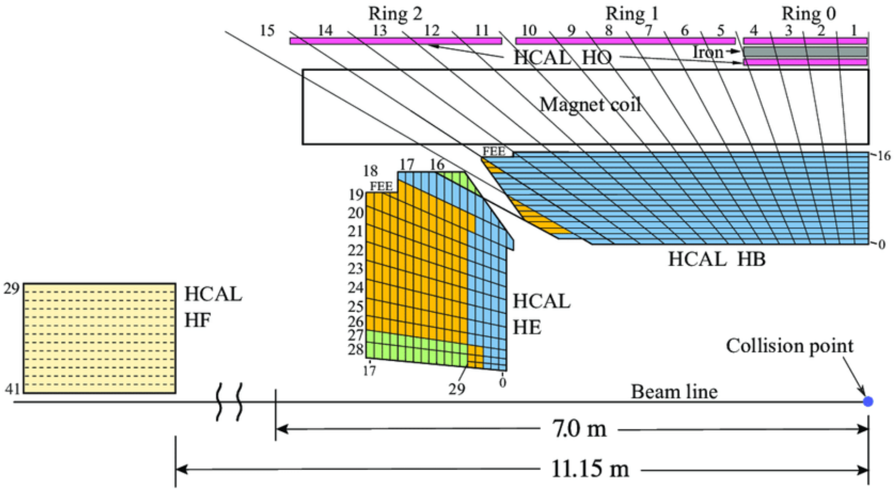

Figure 3.9: A schematic view of one quadrant of the HCAL in the $r - z$ plane showing the arrangement of its subcomponents, including the HB, HE, HO, and HF calorimeters. Figure taken from [120].

in η with a 5° ϕ segmentation covering a pseudorapidity region of $1.3 < |\eta| < 3.0$ for a total of 2304 HE towers. The HO detector is located inside the barrel muon system and contains plastic scintillator tiles with a thickness of 10 mm, covering the pseudorapidity region of $-1.26 < |\eta| < 1.26$. It is also divided into 5 sections along η called “rings” -2, -1, 0, 1, and 2. Finally, the HF detector sits in the pseudorapidity region of $3.0 < |\eta| < 5.0$ and is composed of alternating steel absorbers and quartz fibers. Both HF modules contain 13 towers in η with a 10° ϕ segmentation, leading to a total of 900 HF towers.

For pions, the combined ECAL and HCAL relative energy resolution in the barrel and endcap is given by [117]

$$\frac{\sigma}{E} = \frac{84.7\%}{\sqrt{E}} \oplus 7.6\%, \tag{3.7}$$

while the HF energy resolution is given by

$$\frac{\sigma}{E} = \frac{280\%}{\sqrt{E}} \oplus 11\%. \tag{3.8}$$

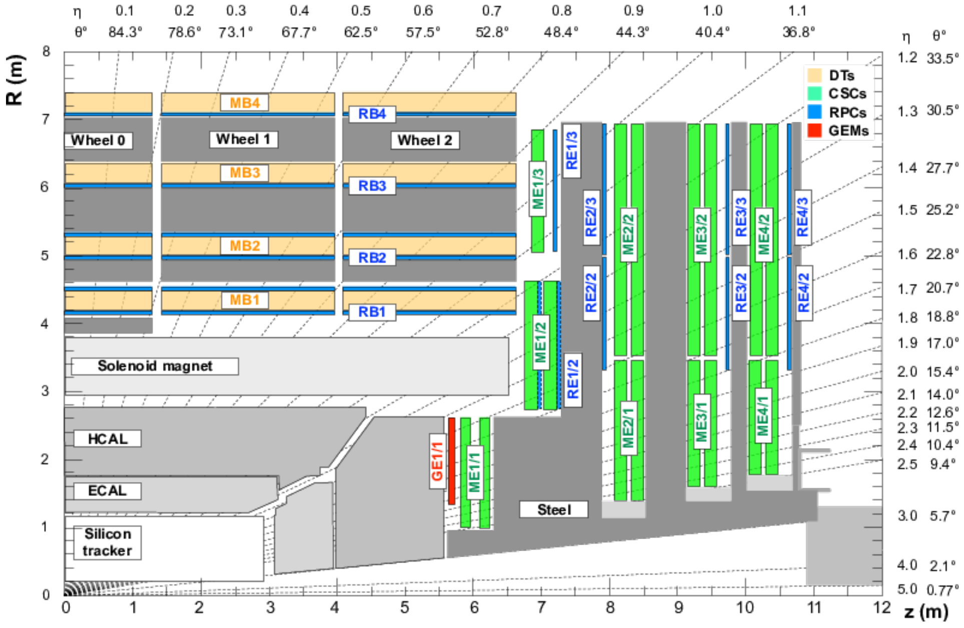

Figure 3.10: A schematic view of one quadrant of the muon system in the $r - z$ plane showing the arrangement of its subcomponents, including the DTs (labeled MB), CSCs (labeled ME), RPCs (labeled RB and RE), and GEMs (labeled GE). Figure taken from [117].

3.2.6 Muon system

The muon system [121] is composed of four complementary detector systems arranged in the steel return yoke of the CMS detector, including drift tubes (DTs), cathode strip chambers (CSCs), resistive plate chambers (RPCs), and gas electron multipliers (GEMs). As the name implies, it is dedicated to identifying, measuring, and triggering on muons, which is critical to many physics results at CMS like the discovery of the Higgs boson. By positioning the muon system behind the calorimeters and solenoid in the steel return yoke, there is a lower probability of particles other than muons and neutrinos penetrating the muon detectors.

A schematic view of one quadrant of the muon system is shown in Fig. 3.10. The central section is configured in a barrel geometry with four roughly cylindrical stations at different radii from the beam axis, while the section in the endcap is arranged in four planar stations instead along the z direction. The DTs are located in the barrel region with pseudorapidity $|\eta| < 1.2$ and provide precise spatial measurements as well as trigger information. The CSCs are located in the endcap region with pseudorapidity $0.9 < |\eta| < 2.4$ and also provide both trigger and precision position information, with a faster response time than the DTs. The RPCs are located in both the barrel and endcap regions in order to complement the DTs and CSCs. Though RPCs have coarser position resolution compared to DTs and CSCs, their very fast response time allows them to be used to unambiguously identify the bunch crossing corresponding to a muon trigger candidate. Finally, the GEM chambers are located in front of the inner ring of CSC chambers in the endcap region and are designed to enhance track reconstruction and trigger capabilities of the endcap muon spectrometer, providing both fast response times and good spatial resolution.

The spatial resolution of the DTs is between 200–600 μm depending on the region, while the spatial resolution of the CSCs is between 75–150 μm. In comparison, the RPCs have a lower spatial resolution of around 1 cm, while the GEMs have a good spatial resolution of around 150–250 μm. The p_T resolution is 1% in the barrel and 3% in the endcap regions for muons with energy up to 100 GeV, and about 10% for high energy muons with p_T up to several TeV.

3.2.7 Trigger system

During data taking, the LHC collides protons with a bunch spacing of 25 ns, corresponding to about one billion proton-proton interactions and a maximum rate of about 40 MHz of data collected. However, due to bandwidth constraints, only about 1000 events per second corresponding to a rate of 1 kHz could be recorded for further analysis during Run 2, which was increased to about 2.6 kHz during Run 3. In order to reduce the rate of data collected while ensuring events with potentially interesting physics are selected, the CMS trigger system divides the data processing into two levels: the Level-1 (L1) Trigger [122], implemented in custom hardware, and the High-Level Trigger (HLT) [123], implemented in software and running on a farm of commercial computers. A diagram of the data flow for an event through the CMS trigger system is shown in Fig. 3.11.

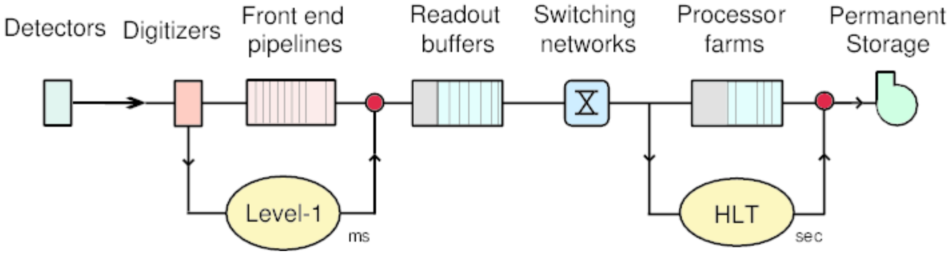

Figure 3.11: A schematic overview of the data flow through the CMS trigger system. Figure taken from [124].

As the first level of the CMS trigger system, the L1 Trigger is designed to reduce the output rate to 100 kHz, which in practice corresponds to a maximal output rate of 30 kHz assuming an approximate safety factor of three. The L1 Trigger uses coarsely segmented data from the calorimeter and muon systems as input and stores high-resolution data in pipelined memories in the front-end electronics. It is split into separate components on the local, regional, and global level. At the local level, local triggers called Trigger Primitive Generators (TPGs) use as input energy deposits in calorimeter trigger towers and track segments or hit patterns in muon chambers, respectively. Regional triggers then combine this information using pattern logic in order to sort trigger objects such as electron or muon candidates into limited spatial regions. The Global Calorimeter and Global Muon Triggers then use this information to determine the highest-rank calorimeter and muon objects and transfer them to the highest level of the L1 Trigger, the Global Trigger. A decision is then made to either reject the event or accept it for further evaluation by the HLT, with an overall latency below 4 μs. A diagram of the architecture of the L1 Trigger is shown in Fig. 3.12.

The HLT consists of a computer farm cluster of about 200 nodes with a combination of CPUs as well as GPUs added during Run 3 that performs further selections in order to reduce the output data rate to 1–2.6 kHz. In addition to the main data stream, data can also be written to an alternate stream called“HLT data scouting” which stores events at higher rates by reducing the data content per event in order to control the bandwidth required. This data scouting stream can be used for calibration purposes as

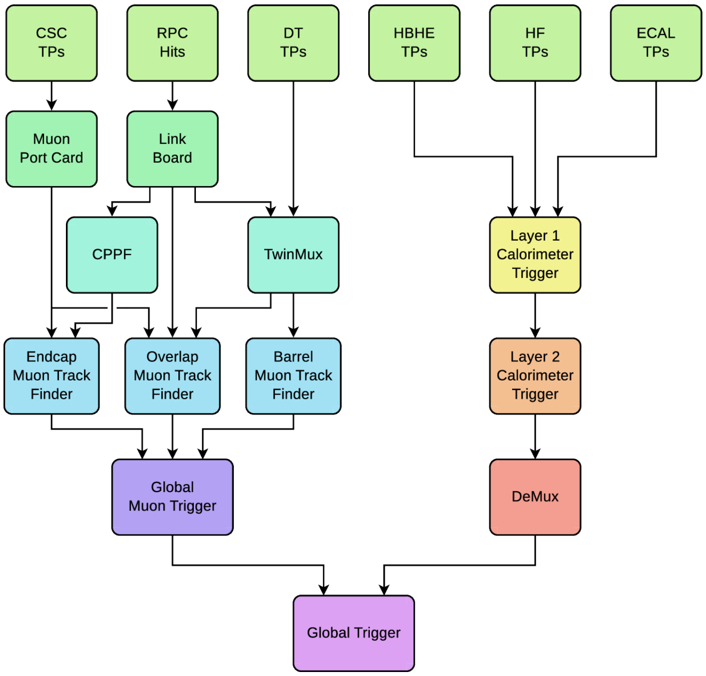

Figure 3.12: A diagram of the upgraded CMS L1 Trigger system during Run 2. Figure taken from [122].

well as alternate physics analyses that can take advantage of lower trigger thresholds. Once data is sent to the HLT, sequences of algorithmic steps called HLT paths are run by the computing cluster in order to reconstruct physics objects and make selections based on certain physics requirements. A configuration of these HLT paths is organized into a trigger menu that is designed to meet specific targets for physics object thresholds and rate allocations. The overall global latency for the HLT during Runs 2 and 3 was between 200–300 ms.

3.2.8 Data acquisition system

After processing by the trigger system, data is then collected and stored by the Data Acquisition (DAQ) system [125], whose architecture is shown in Fig. 3.13. After acceptance by the L1 Trigger, data stored in front-end buffers are pushed into the DAQ system by the Front-End Drivers (FEDs), which are then fed into a two-stage event builder. The data then passes through the event filter farm of the HLT and is temporarily stored at

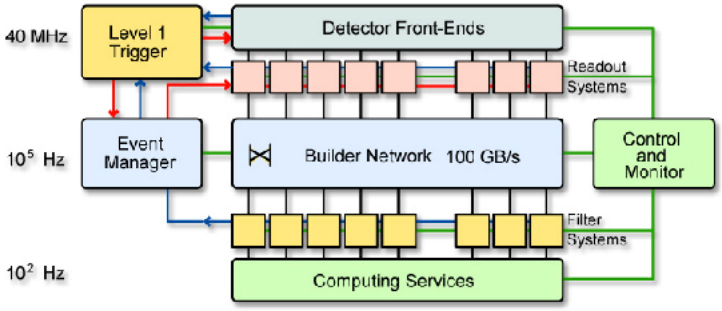

Figure 3.13: A diagram of the architecture of the DAQ system. Figure taken from [109].

CERN's Tier-0 computing facility. This data is then further sent to a global network of computing centers called the Worldwide LHC Computing Grid (WLCG) [126] to handle further data processing and storage. The WLCG includes Tier-1 centers which perform further data processing, storage, and analysis, as well as smaller Tier-2 and Tier-3 facilities for distribution of the data worldwide.

In order to provide feedback on the quality of the recorded data, the DAQ system also includes a Data Quality Monitoring (DQM) system [127] that provides both online and offline monitoring of detector performance and data quality analysis. It is also used in validating reconstruction software production releases and Monte Carlo simulation samples. The DQM system consists of software modules that includes a data collection step, a graphic interface for visualizing the monitoring elements, and tools to handle metadata. Once data has been validated by the DQM, it can be used further in physics analyses. During Run 2, the fraction of data collected at CMS that was certified good for physics ranged between 85–90%, while a similar fraction of above 90% is expected for Run 3 [116].

3.2.9 SWATCH

In order to configure, control, and monitor the L1 Trigger system, CMS has implemented a generic software design called the SWATCH (SoftWare for Automating the conTrol of Common Hardware) framework. The SWATCH framework was originally developed as part of the Phase 1 upgrade to the L1 Trigger system and consists of a set of interfaces for controlling and monitoring the hardware of each of the 9 subsystems associated with the L1 Trigger. Each subsystem is composed of one or more processor boards housed in crates that carry Advanced Mezzanine Card (AMC) modules [128]. These modules are responsible for the clock, data acquisition services, and feedback mechanism for the Trigger Throttling System which monitors the status of the data buffers. The data processing logic for the boards consists of an algorithm block, a Trigger Timing and Control (TTC) block, zero or more ports, and a readout block that sends data from the input and output buffers to the DAQ. This logic is implemented on Field-Programmable Gate Arrays (FPGAs) that transport data through high-speed serial optical links.

The combination of these processors, ports, and interconnections defines the architecture of each subsystem and is stored in subsystem-agnostic data structures in the SWATCH framework. Each component of the subsystems is represented by an abstract class whose objects are built using subsystem specific plugin libraries that include generic system, processing, and manager classes. The generic interface for controlling and monitoring the L1 Trigger hardware includes a processor class which represents the cards that process the data, a DaqTTCManager class for representing the connection to the Timing and Control Distribution System (TCDS) as well as the DAQ network, and a system class representing each trigger subsystem. Each generic interface class also contains a built-in common monitoring and control framework based on actions for controlling the hardware.

Configuration of the hardware is based on three concepts: commands, command sequences, and finite state machines (FSMs). Commands are the basic building block of hardware control and represent stateless actions that can be executed by the hardware, such as resetting the boards or configuring the links. Command sequences are composed of a series of commands that are executed in sequence, while FSMs represent the various control states of the hardware whose transition to other states are defined by commands or command sequences. This configuration data is stored using an Oracle relational database with a single common schema for all the L1 Trigger subsystems composed of four distinct XML-based modules. These modules include “Hardware” for the full system architecture description, “Infra” for the board timing alignment points, “Algo” for calibration

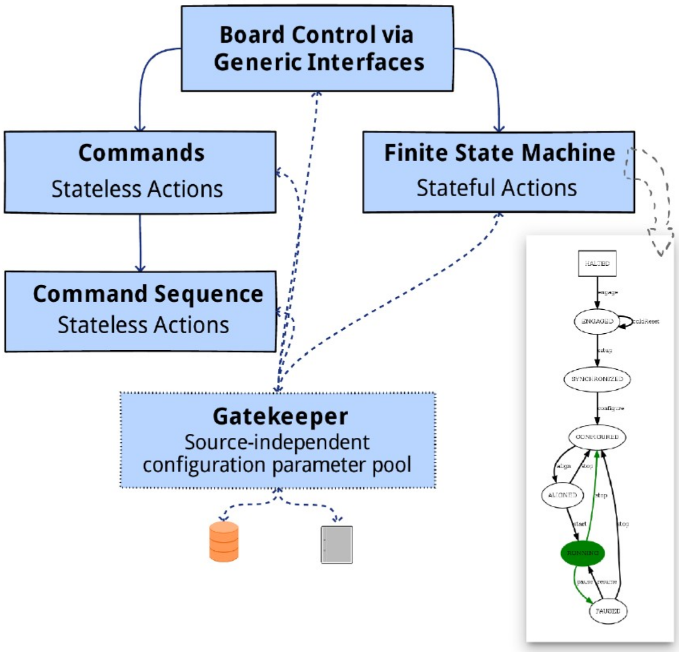

Figure 3.14: The SWATCH hardware configuration interfaces, including commands, command sequences, and FSMs. Figure taken from [129].

factors and physics-related thresholds, and “Run Settings” for hardware masks and monitoring settings. A schematic diagram of the hardware configuration interfaces is shown in Fig. 3.14.

The monitoring framework is composed of two types of classes: metrics and monitorable objects. Metrics represent individual items of monitored data retrieved from the hardware with their associated error and warning conditions which determine the state of the metric. Monitorable objects are classes that contain metrics and other monitorable objects as child nodes, whose overall state is determined by the cumulative status of all its child metrics and monitorable objects. These monitorable objects include processors, processor component interfaces, and subsystems. A schematic diagram of the hardware monitoring interfaces is shown in Fig. 3.15.

In order to operate the SWATCH system at the CMS control room, the Trigger Supervisor [130] framework is implemented in C++ and provides a way to handle the SWATCH system through online applications controlled via web graphical user interfaces. The Trig-

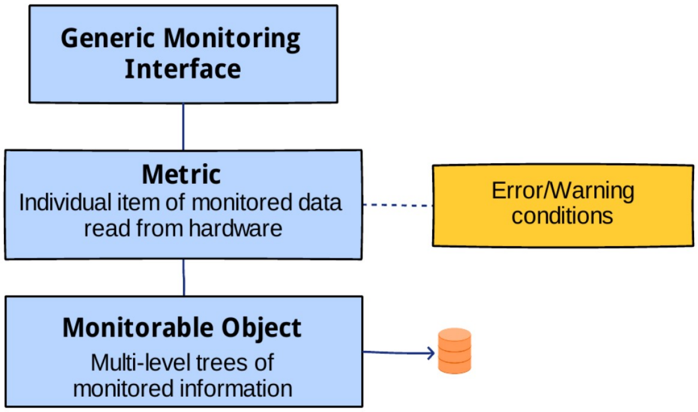

Figure 3.15: The SWATCH hardware monitoring interfaces, including metrics and monitorable objects. Figure taken from [129].

ger Supervisor also handles the configuration of the L1 Trigger components before and during data taking runs which is coordinated by the Central Cell application. The code for SWATCH itself is implemented in a C++ library that is independent from the Trigger Supervisor, with a basic SWATCH skeleton provided for each L1 Trigger subsystem to use as a baseline for further development. In particular, I was responsible for development and maintenance of the SWATCH system associated with the Calorimeter Layer-1 (CaloL1) subsystem, which includes input from both the ECAL and HCAL.

Chapter 4

Analysis Object Reconstruction and Identification

It is important for stable particles to be accurately identified and reconstructed at CMS for use in various physics analyses. This is done by what is known as the particle-flow (PF) algorithm. Section 4.1 provides an overview of the PF algorithm at CMS, while the other sections describe in more detail how specific objects relevant to the DM search are identified and reconstructed, including the primary vertex and pileup (4.2), muons (4.3), electrons (4.4), jets (4.5), b-jets (4.6), and missing transverse momentum (4.7). Finally, Section 4.8 gives a brief description of the Level 1 Phase 2 calorimeter-based jet and tau reconstruction algorithm which I contributed to.

4.1 Particle-flow event reconstruction

The PF algorithm combines global event information from all the different subdetectors at CMS in order to optimally reconstruct and identify stable particles produced in collisions. To do this, the PF algorithm performs correlation on tracks and clusters measured by the subdetectors to determine the primary vertex of the interaction as well as identify all particles in the event. Possible PF candidates include muons, electrons, charged hadrons, neutral hadrons, and photons. Once these PF candidates are identified, a link algorithm

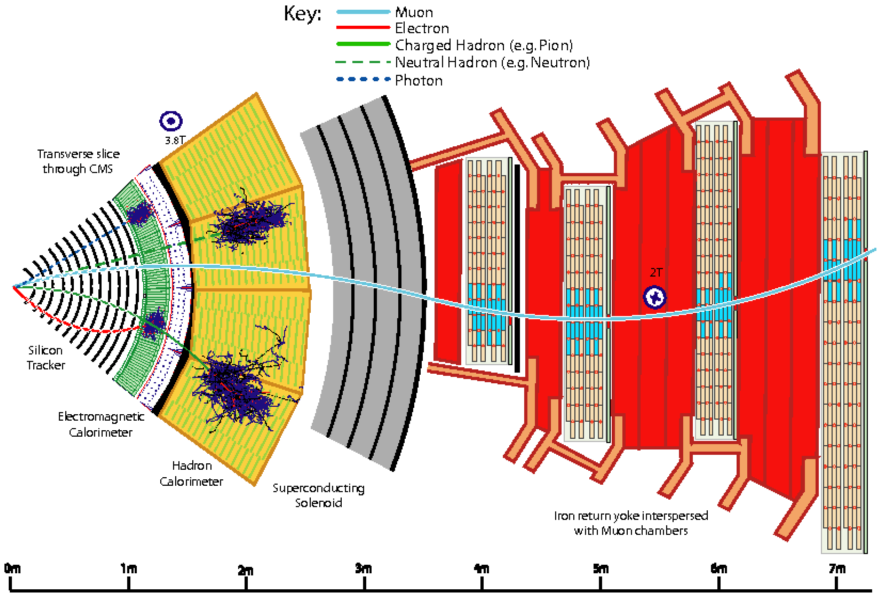

Figure 4.1: Schematic overview of a transverse slice of the CMS detector, showing the different subdetector systems as well as how several PF candidates would interact with these components. Figure taken from [131].

then connects the PF candidates into PF blocks that are then used to reconstruct particles produced in the collision. In each PF block, muon candidates are reconstructed first, followed by electrons, charged hadrons, neutral hadrons, and finally photons. At each step of the process, the corresponding PF elements are removed once they are identified with a reconstructed particle. A schematic overview of how these PF candidates would interact with the components of the CMS detector is shown in Fig. 4.1.

Charged-particle tracks are constructed from a combinatorial track finder based on the Kalman Filtering (KF) algorithm [132], which is separated into three stages: initial seed generation from hits compatible with the charged-particle trajectory, trajectory building from gathering hits from all tracker layers, and final fitting to determine the charged-particle properties such as origin, transverse momentum, and direction. These tracks must be seeded with two hits in consecutive layers in the pixel detector and are required to be reconstructed with at least eight hits in total and with at most one missing hit along the way. In addition, these tracks must be centered around the beam axis and have p_T larger than 0.9 GeV. To increase the tracking efficiency while maintaining the same misreconstructed track rate, the combinatorial track finder is also applied in several successive iterations, referred to as iterative tracking.

These tracks are then matched with calorimeter clusters from the ECAL and HCAL as well as hits from the muon system in order to extrapolate tracks from the tracker to energy deposits in the respective detector subsystem. For muons, tracks are produced in the inner tracker and produce hits in the muon system, leaving almost no trail in the calorimeters. Electrons also produce tracks in the inner tracker and deposit energy in the ECAL that is grouped into energy clusters. Charged hadrons which produce tracks in the inner tracker primarily deposit energy in the HCAL, though a small amount may be left in the ECAL from secondary electromagnetic particle showers produced from the hadron. Since neutral particles like neutral hadrons and photons do not leave tracks in the inner tracker, they are reconstructed last, being matched from energy deposits in the HCAL and ECAL, respectively.

The reconstructed stable particles from the PF algorithm are then used to reconstruct hadronic particle showers called jets, which are later used in algorithms to reconstruct higher-level objects like jets with flavor tagging and missing transverse momentum.

4.2 Primary vertex and pileup

Since the LHC collides multiple protons in bunches at intervals of 25 ns, many proton-proton interactions are produced in any given collision. These interactions produce many possible vertex candidates for where particles can be reconstructed from. In order to identify these vertex candidates, CMS uses a primary vertex (PV) reconstruction algorithm [133] that is divided into three steps: selection of the tracks, clustering of tracks appearing to originate from the same interaction vertex, and fitting for the vertex position using its associated tracks.

Tracks are selected by choosing tracks consistent with being produced promptly at the primary interaction region, which involves imposing requirements on the maximum value of significance of the transverse impact parameter relative to the beam spot center, the number of strip and pixel hits associated with the track, and the normalized χ^2 from a fit to the trajectory. No requirement on the minimum $\mathrm{p_T}$ of the tracks is imposed in order to ensure high reconstruction efficiency. Tracks are then clustered based on their $z-$coordinates at their point of closest approach to the beam spot center using a deterministic annealing (DA) algorithm [134], which allows for the reconstruction of any number of proton-proton interactions from the same bunch crossing. Candidate vertices containing at least two tracks are then fitted using an adaptive vertex fitter [135] to compute the best estimate of vertex parameters such as the x, y, and z position as well as the number of degrees of freedom (dof) for the vertex defined by

$$n_{\mathrm{dof}} = -3 + 2 \sum_{i=1}^{\#\mathrm{tracks}} w_i, \tag{4.1}$$

where w_i is the weight between 0 and 1 of the ith track that reflects the likelihood that it belongs to a genuine vertex. The vertex candidate with the highest value of $\sum_i \mathrm{p}^2_{\mathrm{T_i}}$ is then defined as the PV, where $\mathrm{p_{T_i}}$ is the transverse momentum of the ith track belonging to the vertex.

Interactions that result from the additional vertex candidates not identified as the PV are referred to as pileup (PU) events. The amount of PU in collisions depends on the luminosity of the collision, with higher luminosity leading to higher PU. Figure 4.2 shows the PU for different years of data taking at CMS, where one can see that PU has steadily increased with time as the luminosity of the LHC beam has increased. The HL-LHC aims to achieve an instantaneous luminosity of 5×10^{34} $\mathrm{cm^{-2}s^{-1}}$, a factor of 5–7 times higher than the luminosity achieved in Run 2, which correspond to PU conditions of 200 PU per event. To mitigate the effects of PU on the reconstruction of particle tracks and energy deposits in the detectors, various track-based and calorimeter-based algorithms are employed to subtract these contributions during the reconstruction of the event.

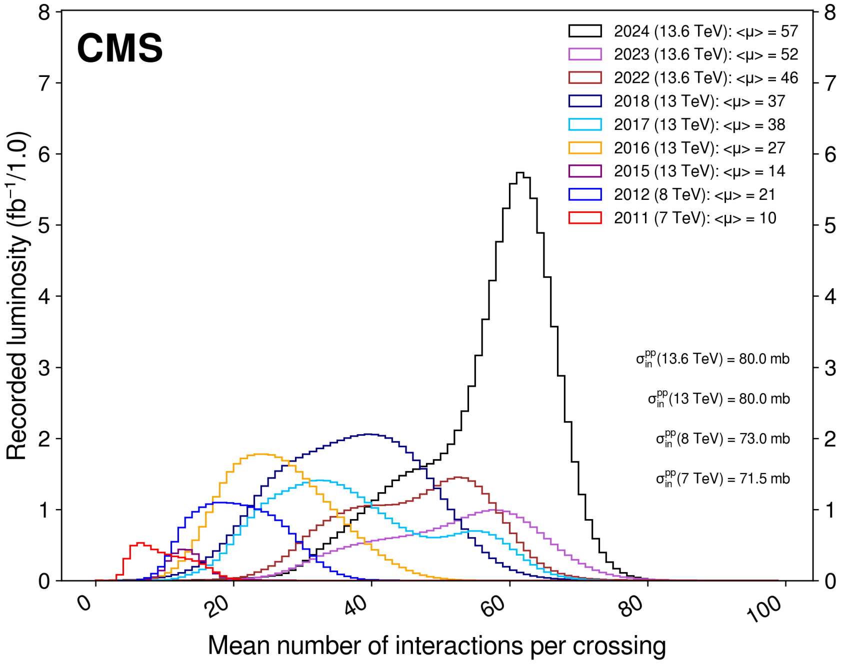

Figure 4.2: Distribution of pileup for proton-proton collisions during different years of data taking at CMS. Figure taken from [116].

4.3 Muons

Muons in the PF algorithm are selected based on both global and tracker muon properties, including tracks and hits in both the inner tracker and muon system. Tracks are first reconstructed independently in two ways: the inner tracker (tracker track) and in the muon system (standalone muon track). For global muon reconstruction, each standalone-muon track is matched to a tracker track. A global muon track is then fitted by combining hits from the tracker track and standalone muon track using the Kalman Filtering (KF) technique [132]. For tracker muons, all tracker tracks with $\mathrm{p_T} > 0.5$ GeV and total momentum $\mathrm{p} > 2.5$ GeV are considered as possible muon candidates and are extrapolated to the muon system. Any candidate with at least one muon segment in the muon system that matches the extrapolated track is considered to be a tracker muon. Though tracker muon reconstruction is more efficient than global muon reconstruction at low momentum ($p < 5$ GeV), global muon reconstruction is designed to have higher efficiency for muons that penetrate through more than one muon station.

Isolated global muons are then selected based on additional inner tracks and calorimeter energy deposits in the muon system that are a distance $\Delta R = \sqrt{\Delta\eta^2 + \Delta\phi^2} < 0.3$ to the muon direction in the (η, ϕ) plane. For these isolated muons, the sum of the $\mathrm{p_T}$ of the tracks and transverse energy ($\mathrm{E_T}$) of the deposits is required to be less than 10% of the muon $\mathrm{p_T}$. For non-isolated global muons, a minimum selection on the global-muon track fit is imposed, which includes the requirement that $\chi^2/\mathrm{dof} < 10$ and at least one muon chamber hit is included for the global-muon track fit. In addition, the non-isolated global muon is required to be matched to muon segments in at least two muon stations. Candidates that fail these selections can still be identified as non-isolated global muons if their standalone muon track or tracker track fit is associated with a large number of hits in the muon detectors.

Once these muon candidates are identified by the PF algorithm, additional quality requirements are also imposed depending on the type of muon considered in the analysis (see Section 5.3). Reconstruction and identification efficiency for muons can be measured using $J/\psi \to \mu^+\mu^-$ and $\mathrm{Z} \to \mu^+\mu^-$ events using a tag-and-probe technique. This technique involves selecting a “tag” muon with strict selection requirements while selecting a “probe” muon with a more relaxed selection such that it does not bias the efficiency one wants to measure. The efficiency is then estimated from the fraction of probe muons that pass a given selection. Tag-and-probe results using $\mathrm{Z} \to \mu^+\mu^-$ events in data compared to simulation are shown in Fig. 4.3. For muons with $\mathrm{p_T} > 10$ GeV, muon identification and reconstruction efficiency exceeds 98% in both barrel and endcap regions of the detector [121].

4.4 Electrons

Electrons in the PF algorithm are selected based on combining information from the inner tracker and the ECAL. Though isolated photon reconstruction is also performed together with electron reconstruction, this section will focus on electron reconstruction

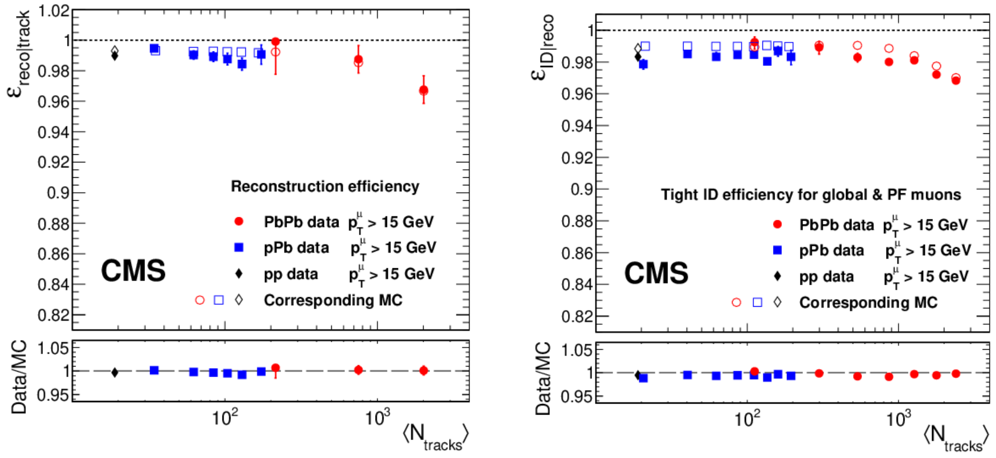

Figure 4.3: Tag-and-probe results for the PF muon reconstruction (left) and identification (right) efficiency in 2017 and 2018 data compared to simulation as a function of the number of muon tracks in pp, pPb, and PbPb collisions. Figure taken from [136].

only. Since electrons can produce a shower of electrons and photons through a combination of bremsstrahlung radiation and photon pair production, a dedicated algorithm is used to combine clusters from these shower particles into a single object in order to recover the energy of the original electron. To estimate the track parameters of the electron in the inner tracker, a dedicated algorithm based on the Gaussian sum filter (GSF) [137] is employed.

Electron reconstruction starts with the formation of clusters by grouping together ECAL crystals with energies exceeding a minimum threshold. The cluster with the highest energy is then defined as the seed cluster, with a minimum E_T requirement of 1 GeV. ECAL clusters around the seed cluster are then combined into superclusters (SCs) in order to include both photon conversions and losses from bremsstrahlung radiation. These SCs are then matched to seeds in the inner tracker compatible with the SC position and trajectory in order to seed the GSF tracking step. In parallel, generic tracks in the inner tracker are selected with $p_T > 2$ GeV and tested for compatibility with the electron trajectory, then used as additional seeds in the GSF tracking step. The ECAL clusters, SCs, GSF tracks, and generic tracks associated with electron are then combined with conversion

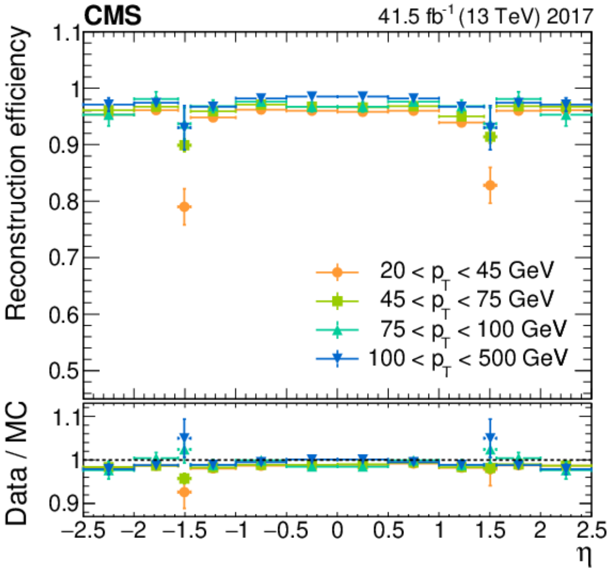

Figure 4.4: Tag-and-probe results for electron reconstruction efficiency in 2017 data compared to simulation as a function of electron η. Figure taken from [138].

tracks and associated clusters in the ECAL to form PF blocks, which are resolved into electron candidates originating from a GSF track.

Once these electron candidates are identified by the PF algorithm, additional quality requirements are also imposed depending on the type of electron considered in the analysis (see Section 5.3). Reconstruction and identification efficiency for electrons can be measured using $\mathrm{Z} \to e^+e^-$ events using the same tag-and-probe technique described in Section 4.3. Tag-and-probe results using $\mathrm{Z} \to e^+e^-$ events in data compared to simulation are shown in Fig. 4.4. For electrons with $\mathrm{p_T} > 20$ GeV, the combined electron identification and reconstruction efficiency exceeds 80–90% in both barrel and endcap regions [138].

4.5 Jets

In addition to leptons like electrons and muons, partons like quarks and gluons carrying color charge can also be produced in proton-proton collisions at the LHC. However, because of QCD confinement, only color-neutral configurations are observed in nature. As a result, these partons instead undergo hadronization and produce a collimated shower of particles called a jet. These jets are reconstructed using a dedicated jet clustering algorithm called the anti-k_t algorithm [139].

The anti-k_t algorithm takes as input either particles reconstructed by the PF algorithm (PF jets) or the sum of ECAL and HCAL energies deposited in the calorimeter towers (Calo jets). For the DM search, only PF jets are considered. For each PF candidate, distances d_{ij} between each candidate are defined:

$$d_{ij} = \min\left(k_{ti}^{-2}, k_{tj}^{-2}\right) \frac{\Delta_{ij}^2}{R^2}, \tag{4.2}$$

where $\Delta_{ij}^2 = (y_i - y_j)^2 + (\phi_i - \phi_j)^2$ and k_{ti}, y_i, and ϕ_i are the transverse momentum, rapidity, and azimuthal angle of particle i, respectively, and R is the radius parameter. The jets considered in the DM search have $R = 0.4$ and are referred to as AK4 jets, In addition, the distance d_{iB} between each PF candidate and the beam is also defined:

$$d_{iB} = k_{ti}^{-2}. \tag{4.3}$$

After calculating the distances d_{ij} and d_{iB} for each PF candidate, the algorithm then proceeds by identifying the smallest of these distances. If this smallest distance is a d_{ij}, then candidates i and j are recombined to form a single candidate and d_{ij} is recalculated. If the smallest distance is a d_{iB}, though, candidate i is identified as a jet and removed from the list of candidates. The distances are recalculated and the process is repeated until no candidates are left.

One important characteristic of the anti-k_t algorithm is that the distance d_{ij} between soft particles will in general be much larger than between a hard and soft particle that are similarly separated. As a result, soft particles will tend to cluster with hard ones before they cluster among themselves, and hard particles with no hard neighbors within distance $2R$ will tend to accumulate all the soft particles within a circle of radius R. Thus, the anti-k_t algorithm will tend to produce jets that are conical in shape, shown in Fig. 4.5.

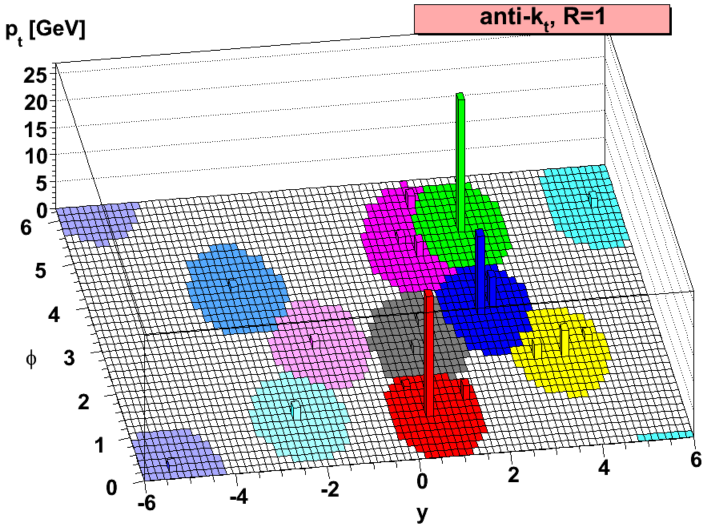

Figure 4.5: A sample parton-level event generated from Monte Carlo simulation illustrating the clustering of jet candidates for the anti-k_t algorithm. Figure taken from [139].

Once jets have been reconstructed, additional corrections are applied in order to take into account various factors. To calibrate jets to the correct energy scale, various jet energy scale (JES) corrections are applied. The JES corrections have several components that are applied sequentially to the jets in both data and simulation. First, a PU offset correction is estimated and subtracted from the jet to account for possible additional energy in the reconstructed jets from PF candidates resulting from PU vertices. Then, another set of corrections is applied to compensate for the non-linear response of the detector as a function of jet η and p_T based on studying dijet and Z/γ+jet events. In addition, residual corrections to correct for remaining differences in the jet response between data and simulation are applied to data only. Finally, flavor effects are compensated for with a set of flavor-based corrections in both data and simulation.

Differences in the energy resolution of reconstructed jets in data compared to simulation is also accounted for by applying jet energy resolution (JER) calibrations. These corrections are measured using Z/γ+jet events and applied to simulation only.

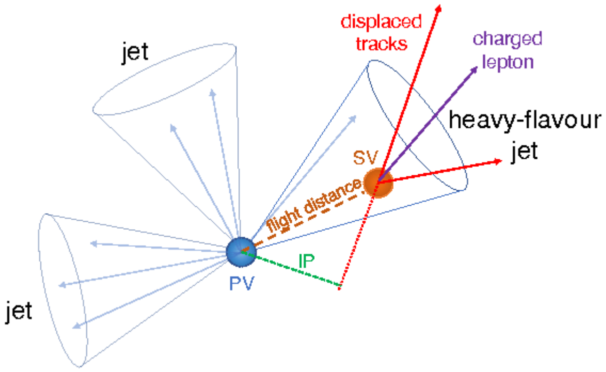

Figure 4.6: Illustration of a heavy-flavor jet with charged particle tracks that are displaced with respect to the PV. Figure taken from [141].

4.6 B-jets

One important type of jets in the DM search are those that originate from the hadronization of heavy-flavor quarks like the bottom (b) quark. Since heavy-flavor quarks have larger masses and longer lifetimes than light-flavor quarks, these jets tend to produce longer-lived particles than those originating from light-flavor quarks, resulting in decays that are displaced from the PV, shown in Fig. 4.6. The origins of these displaced tracks are called secondary vertices (SV), and they are an important component of algorithms used to classify heavy-flavor jets. These algorithms typically involve vertex-finding algorithms like the CSV [140] algorithm that aim to reconstruct SV candidates satisfying certain quality criteria in order to determine a continuous output between 0 and 1 for each jet that measures how likely the jet arises from a heavy-flavor quark.

In the DM search, the DeepCSV algorithm [142] is used to identify jets originating from a b quark (b-jets). Like the CSV algorithm, the DeepCSV algorithm takes into account both SV and track information such as the track impact parameter in order to produce an output between 0 and 1 measuring how likely the jet arises from a b quark. However, rather than a set of simple quality criteria, the DeepCSV algorithm employs a deep neural network (DNN) with 5 hidden layers of a width of 100 nodes each that is trained on Monte Carlo simulated datasets where the true origin of the jet is known using SV, track information, and jet information as input. Multiple output scores are produced for identifying bottom (b), charm (c), or other light flavor quarks (up, down, strange).

Different working points can then be defined based on the b-tagging efficiency and misidentification rate of the algorithm [141]. These working points are defined as “loose”, “medium”, and “tight”, corresponding to respective b-tagging efficiencies of 85%, 70%, and 55% and respective misidentification rates as light-flavor jets of 10%, 1%, and 0.1%.

4.7 Missing transverse momentum

Though the CMS detector is designed to measure as many different types of particles as possible, some particles do not interact or interact very weakly with the detector (i.e. neutrinos, DM). However, since the total transverse momentum of the colliding protons is effectively zero, then by conservation of energy and momentum the total transverse momentum of all particles produced by the collision should also be zero. Thus, if the total remaining transverse momentum of the measured particles in the detector is non-zero, then the presence of particles which do not interact with the detector can be inferred from the remaining transverse momentum that can be attributed to these invisible particles.

This quantity is referred to as missing transverse momentum ($\mathrm{p_T^{miss}}$) and is defined as the magnitude of the negative vectorial sum of the transverse momenta of all the PF candidates in the event:

$$\vec{\mathrm{p}}_{\mathrm{T,PF}}^{\mathrm{miss}}(\mathrm{raw}) = -\sum_{i=1}^{N_{\mathrm{particles}}} \vec{\mathrm{p}}_{\mathrm{T,i}}, \tag{4.4}$$

where $\vec{\mathrm{p}}_{\mathrm{T,i}}$ is the momentum vector of the ith PF candidate. In order to account for JES corrections applied to PF jets, an additional term is included to replace the raw momentum of each jet with its corrected value:

$$\vec{\mathrm{p}}_{\mathrm{T,PF}}^{\mathrm{miss}} = \vec{\mathrm{p}}_{\mathrm{T,PF}}^{\mathrm{miss}}(\mathrm{raw}) - \sum_{j=1}^{N_{\mathrm{PFjets}}} \left(\vec{\mathrm{p}}_{\mathrm{T,j}}^{\mathrm{corr}} - \vec{\mathrm{p}}_{\mathrm{T,j}}\right), \tag{4.5}$$

where $\vec{\mathrm{p}}_{\mathrm{T,j}}^{\mathrm{corr}}$ is the $\vec{\mathrm{p}}_{\mathrm{T}}$ for each PF jet with JES corrections applied, and the sum is over jets with $\vec{\mathrm{p}}_{\mathrm{T,j}} > 15$ GeV. Further corrections are applied to improve performance at large

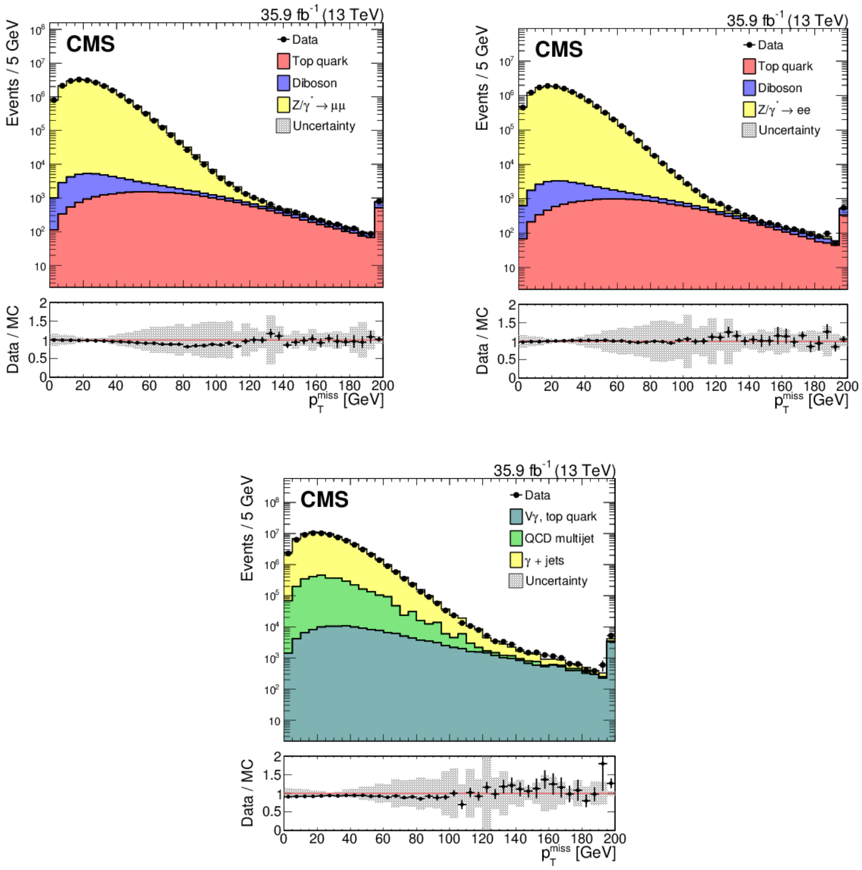

Figure 4.7: Distributions of $\mathrm{p}_{\mathrm{T}}^{\mathrm{miss}}$ in $\mathrm{Z} \rightarrow \mu^+\mu^-$ (top left), $\mathrm{Z} \rightarrow e^+e^-$ (top right), and γ+jets (bottom) events in data and simulation. The lower panel shows the ratio of data to simulation. The shaded band represents systematic uncertainties due to JES, JER, and variations in the energy scale of unclustered particles. Figure taken from [143].

PU conditions.

Performance of the $\mathrm{p}_{\mathrm{T}}^{\mathrm{miss}}$ reconstruction algorithm is evaluated using a combination of $\mathrm{Z} \rightarrow \mu^+\mu^-$, $\mathrm{Z} \rightarrow e^+e^-$, and γ+jets events, shown in Fig. 4.7. The $\mathrm{p}_{\mathrm{T}}^{\mathrm{miss}}$ resolution in these events are dominated by hadronic activity, with 5-20% uncertainty in the jet momentum resolution compared to $< 1.5\%$ for lepton and photon momentum resolution.

4.8 Level 1 Phase 2 calorimeter-based jets and taus

In addition to the PF reconstructed objects described in the previous sections, jet and tau objects can also be reconstructed using only L1 Trigger (L1T) calorimeter specific information from the ECAL and HCAL subsystems. These objects, referred to as GCTJets and GCTTaus, can be used by HLT algorithms to provide preliminary selections on events in combination with other algorithms. For Phase 2, upgrades to the calorimeter subdetectors are planned that include higher granularity and precision timing information to address the higher PU conditions expected for the HL-LHC [144]. In particular, the granularity in the barrel region is expected to increase by a factor of 25, while a new high granularity endcap system for the HCAL subdetector called the HGCal [145] will be installed. Both of these improvements require new firmware with much higher resource utilization compared to Phase 1. As a result, studies were performed to implement and test the performance of a Phase 2 version for the reconstruction algorithm for L1T GCTJets and GCTTaus [146].

The reconstruction algorithm for L1T GCTJets uses energy deposits in the barrel and endcap regions of the ECAL and HCAL to construct a 9×9 square geometry of tower objects to identify a jet. In order to meet resource utilization constraints for Phase 2, an intermediate step of constructing "supertower" objects from 3×3 clusters of tower objects is introduced, which is then used to define GCTJet objects. This reconstruction is initiated by using the supertower with the highest energy as the seed tower around which 3×3 supertower regions are constructed around. The energies contained in these supertowers are then removed from consideration and reconstruction proceeds to subleading supertower seeds until a total of 12 GCTJets are reconstructed for three separate η regions (6 for each positive and negative η half). A minimum seed energy threshold of 10 GeV is imposed, and the energies of the reconstructed jets are corrected for measured energy and PU at HL-LHC conditions.

Tau objects are then built from the GCTJet objects by using the energy of the seed supertower in each GCTJet to define a GCTTau object. As with the reconstructed jets, a total of 12 GCTTaus corresponding to the 12 GCTJets are reconstructed for three separate η regions (6 for each positive and negative η half), and the energies of the reconstructed taus are also corrected for measured energy and PU at HL-LHC conditions. Figure 4.8

I was responsible for both designing the GCTTau algorithm as well as validating the

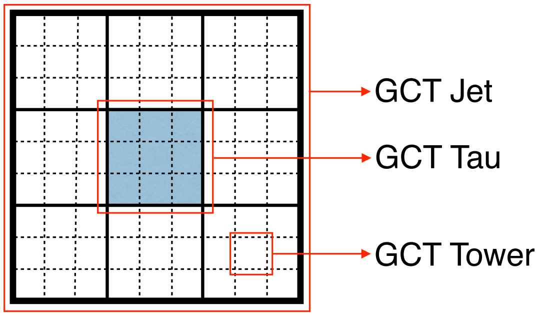

Figure 4.8: An illustration of the 9×9 square geometry of towers (GCT Tower) used to identify the GCTJet objects, as well as the 3×3 tower regions used to define the supertower objects. The supertower seed corresponding to the GCTTau object reconstructed is also shown. Figure taken from [146].

performance of both the GCTJet and GCTTau algorithms for Phase 2. Compared to Phase 1 versions of the algorithm, emulated performance of the Phase 2 L1T GCTJets and GCTTaus either matched or exceeded Run 2 performance, with similar resolutions, efficiencies, and rates observed. Emulated efficiencies and rates for the Phase 2 L1T GCTTaus are shown in Fig. 4.9.

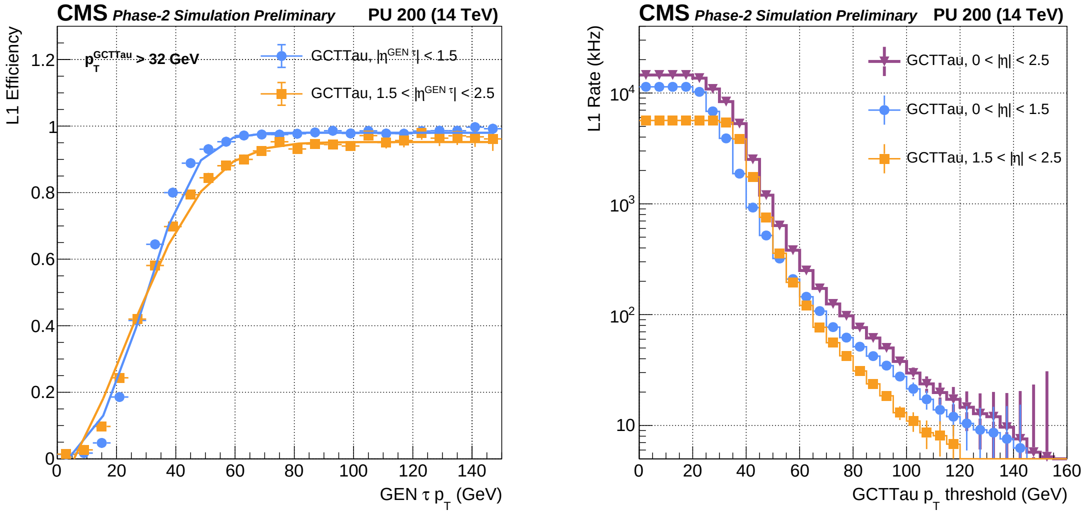

Figure 4.9: The L1 trigger + matching efficiencies of GCTTaus in the barrel and endcap regions as a function of generator-level tau p_T are shown for simulated VBF H→ $\tau\tau$ events at 200 average PU interactions (left). The L1 trigger rates of GCTTaus in the barrel, endcap, and central regions are also shown as functions of the single GCTTau p_T trigger thresholds, measured in a minimum bias MC sample at 200 average PU conditions (right). Figures taken from [146].

Chapter 5

Dark Matter Analysis

This chapter presents the main analysis I worked on, which is a search for dark matter (DM) produced in association with top quarks using data collected by the CMS detector during Run 2 (2016–2018) at the LHC [147]. Though the focus of my work has been on the all hadronic and single lepton channels of the analysis, the combined results with the dilepton channel are presented as well, which involves significant contribution from groups at CERN, Deutsches Elektronen-Synchrotron (DESY), and Instituto de Física de Cantabria (IFCA). Section 5.1 provides a brief overview of the theoretical signal models considered for the search. Section 5.2 describes the data and simulated samples used as well as how simulated samples are generated. Section 5.3 defines the main objects used and how they are selected in the analysis. Section 5.4 covers the selection requirements for events in the signal regions of each channel as well as the discriminating variables used for selection. Section 5.5 explains how the main backgrounds in each channel are estimated. Section 5.6 describes the systematic uncertainties considered in the analysis. Section 5.7 describes the statistical techniques used to extract the signal. Finally, Section 5.8 presents the results of the statistical analysis in Section 5.7.

5.1 Signal model

Although the origin of DM is unknown, its existence can be inferred from astrophysical observations based on its gravitational effects on galaxies and other large-scale objects. To explain DM, many models have been suggested in the context of particle physics [148]. In many of these models, DM is assumed to be made of weakly interacting massive particles (WIMPs) whose properties are constrained by astrophysical observations. WIMPs are predicted to have weak scale interactions with Standard Model (SM) particles and can interact with SM constituents through mediator particles, which allows WIMPs to be produced at high energy particle colliders such as the LHC at CERN. These DM particles, if produced at the LHC, would escape the CMS detector without leaving behind any reconstructible sign of its passage and be effectively invisible to the detectors. However, like neutrinos, one can still infer the presence of DM by the unbalanced momentum left behind in the plane transverse to the proton beams, referred to as missing transverse momentum ($\mathrm{p_T^{miss}}$). Since $\mathrm{p_T^{miss}}$ requires the presence of a visible particle to reconstruct, one way to observe DM is to look for production of DM recoiling against visible SM particles such as hadronic jets, vector bosons, and top quarks. These types of searches are known as "MET+X" searches.

Early MET+X searches at CMS during Run 1 [149–155] employed models which assumed the mediator of the interaction between DM and SM particles was very heavy, leading to the use of effective field theories (EFTs) where the production of DM is assumed to take place through contact interactions. If the mass of the mediator is low enough to be produced at the LHC, though, then models which explicitly take into account the kinematic features of the mediator are needed. These class of models are called simplified models, and a set of benchmark simplified models have been developed for use by the ATLAS/CMS Dark Matter Forum [156, 157].

In particular, the simplified model used in this search assumes the existence of either a new neutral scalar (ϕ) or pseudoscalar (a) spin-0 mediator particle that can interact with both the SM fermion sector and a new fermionic Dirac DM particle (χ). To ensure the model does not violate flavor constraints, it also assumes Minimal Flavor Violation (MFV) [158–161], which means that the flavor structure of the couplings between DM and SM particles follows the same structure in the SM. For couplings to SM fermions, this assumption implies that the coupling to DM is proportional to the SM Yukawa coupling between the fermion and the Higgs boson. This construction results in a model with a minimal set of four parameters: the mass of the DM particle (m_χ), the mass of the mediator ($m_{\phi/\mathrm{a}}$), the coupling between the mediator and SM fermions (g_q), and the coupling between the mediator and DM particle (g_χ).

The Lagrangian for this model can be expressed as

$$\mathcal{L}_\phi = \mathcal{L}_\mathrm{SM} + \frac{1}{2}(\partial_\mu \phi)^2 - \frac{1}{2} m_\phi^2 \phi^2 + i\bar{\chi}\not{\partial}\chi - m_\phi \bar{\chi}\chi - g_\chi \phi \bar{\chi}\chi - \frac{\phi}{\sqrt{2}} \sum_{\mathrm{q=u,d,s,c,b,t}} g_\mathrm{q} y_\mathrm{q} \bar{q} q \quad (5.1)$$

for the case of a scalar mediator and

$$\mathcal{L}_\mathrm{a} = \mathcal{L}_\mathrm{SM} + \frac{1}{2}(\partial_\mu \mathrm{a})^2 - \frac{1}{2} m_\mathrm{a}^2 \mathrm{a}^2 + i\bar{\chi}\not{\partial}\chi - m_\phi \bar{\chi}\chi - i g_\chi \mathrm{a} \bar{\chi}\gamma_5\chi - \frac{i\mathrm{a}}{\sqrt{2}} \sum_{\mathrm{q=u,d,s,c,b,t}} g_\mathrm{q} y_\mathrm{q} \bar{q}\gamma_5 q \quad (5.2)$$

for case of a pseudoscalar mediator, where $\mathcal{L}_\mathrm{SM}$ is the SM Lagrangian, $y_\mathrm{q} = \sqrt{2} m_\mathrm{q}/v$ is the SM Yukawa coupling normalized to the Higgs vacuum expectation value v, and the coupling g_q is assumed to be universal to all quarks. Since the coupling of the mediator is proportional to the mass of the fermion it couples to, the mediators under this model will preferentially couple to heavy third-generation quarks. Therefore, this search focuses on looking for DM particles produced in association with either a single top quark (t/$\bar{\mathrm{t}}$+DM events) or a top quark pair (t$\bar{\mathrm{t}}$+DM events) [162]. Feynman diagrams of the dominant processes involving the t/$\bar{\mathrm{t}}$+DM and t$\bar{\mathrm{t}}$ production in the context of this simplified model are shown in Fig. 5.1.

Depending on the decay of the top quark, the final states of the signal processes considered in Fig. 5.1 can be categorized into three channels based on the number of leptons present: the all-hadronic (AH) channel for zero leptons, the single lepton (SL) channel for one lepton, and the dileptonic (DL) channel for two leptons. Previous searches

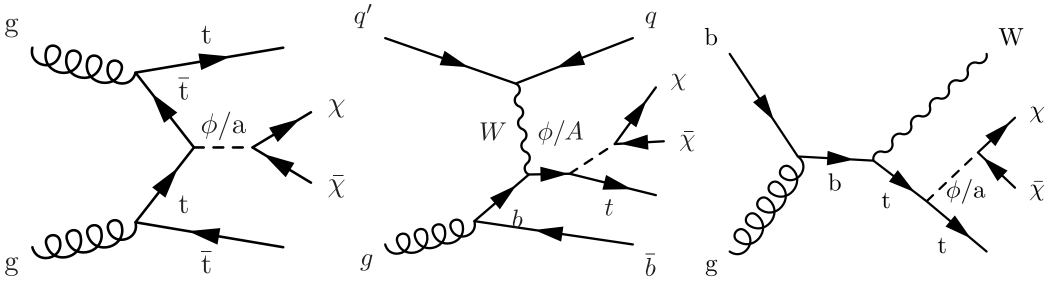

Figure 5.1: Feynman diagrams of the production of DM particles (χ) with a top quark pair (left) and a single top quark in both the t-channel (center) and tW-channel (right) production modes in the context of a simplified model with a scalar/pseudoscalar (ϕ/a) mediator. The additional quark q in the t-channel diagram is often produced at high pseudorapidity.

for DM produced in association with either a single top quark or top quark pair have been carried out at CMS in these channels using data collected at a center-of-mass energy of 13 TeV [106, 163]. Though the analysis described in this thesis probes similar signal topologies to these previous searches, there are considerable differences in strategy for some of these channels. In particular, lower jet multiplicities were considered, resulting in an increase in sensitivity to the t/t̄+DM signal process.

In the AH and SL channels, the main strategy is to look for an excess of events above the SM background in the p_T^{miss} spectrum, which is motivated by the expected decay of the top quark in the dominant t-channel and tW-channel production modes. In the DL channel, novel multivariate techniques are employed using characteristic features of the signal production modes. In all three channels considered, dedicated search strategies are used to further enhance the separation power of the signal against the SM background for both t/t̄+DM and tt̄ processes.

In addition to the simplified model considered above, other models involving axion-like particles (ALPs) can also provide a mediator to the dark sector. The ALPs are spin-0 particles which are not only promising candidates for mediators to the dark sector [164–167], but can also provide a solution to the strong-CP problem [55, 168–170]. They are spin-0 particles that do not interact with the SM gauge groups but emerge as pseudo-Nambu-Goldstone bosons due to an approximate axion shift symmetry. As a result of this symmetry, the masses of ALPs can be significantly smaller than the energy scale of the underlying ultraviolet model, which provides the opportunity to study couplings to these particles at the LHC. In particular, models involving ALPs typically have couplings to fermions that are proportional to the fermion masses, which motivates the focus on studying the ALP coupling to heavy third-generation quarks like the top quark.

Like the simplified model, the ALP model considered in this analysis features a Dirac fermionic DM candidate χ and a pseudoscalar ALP particle A which interacts with SM fermions and acts as a DM mediator using a Lagrangian of the form

$$\mathcal{L}_{\mathrm{A}} = \mathcal{L}_{\mathrm{SM}} + \frac{1}{2}(\partial_\mu A)(\partial^\mu A) + \frac{1}{2}m_{\mathrm{A}}^2 A^2 + i\bar{\chi}\not{\partial}\chi - m_\chi\bar{\chi}\chi - ic_{\mathrm{t}}\frac{m_{\mathrm{t}}}{f_{\mathrm{A}}}\bar{t}\gamma_5 t\mathrm{A} - ic_\chi\frac{m_\chi}{f_{\mathrm{A}}}\bar{\chi}\gamma_5\chi\mathrm{A}, \quad (5.3)$$

where t is top quark field, m_{t} is the mass of the top quark, f_{A} is the ALP decay constant, c_{t} is the coupling between the ALP and the top quark, and c_χ is the coupling between the ALP and DM fermion. Because of the similarity of this Lagrangian to the one in Eq. 5.2, the same processes shown in Fig. 5.1 can be considered.

5.2 Data sample and simulation

The data used in this search were collected by the CMS detector during Run 2 from 2016–2018, corresponding to an integrated luminosity of 138 fb^{-1}. Several different online trigger selections were used to collect the data depending on the channel considered. In the AH channel, $\mathrm{p}_{\mathrm{T}}^{\mathrm{miss}}$ triggers are used to select events that contain no leptons and have both $\mathrm{p}_{\mathrm{T}}^{\mathrm{miss}}$ and missing hadronic activity ($\mathrm{H}_{\mathrm{T}}^{\mathrm{miss}}$) above 120 GeV [171]. In the SL channel, a second set of triggers are used to select events containing at least one isolated electron (muon) with $\mathrm{p}_{\mathrm{T}} > 27$ (24) GeV. In the DL channel, a combination of both single lepton and dilepton triggers are used to select events with two leptons (e, μ). The efficiency of the $\mathrm{p}_{\mathrm{T}}^{\mathrm{miss}}$ triggers in the hadronic channel is nearly 100% for events with $\mathrm{p}_{\mathrm{T}}^{\mathrm{miss}} > 250$ GeV, while the efficiency of the triggers used in the SL channel is above 90% for leptons with $\mathrm{p}_{\mathrm{T}} > 30$ GeV. The average efficiency of the triggers used in the DL channel is 98% for events with two leptons with $p_T > 25$ (20) GeV.

To estimate both signal and SM background, Monte Carlo (MC) event generators are used to simulate events produced in proton-proton collisions at the LHC [172]. These simulations are divided into several steps. First, events are generated through hard scattering processes of initial state partons whose cross sections take into consideration Parton Density Functions (PDFs) as well as Feynman diagram matrix elements using perturbation theory at different fixed orders of approximation. The most commonly used orders of approximation are Leading Order (LO), which involve tree-level diagrams, and Next-to-Leading Order (NLO), which includes one-loop and real emission diagrams. Next, generators produce parton showers which undergo hadronization and decay into particles that can be reconstructed by the detector. Finally, the response of the detector is simulated for each particle, after which the same reconstruction of objects described in Chapter 4 is applied to simulation.

The `POWHEG v2` [173–178] event generator was used to generate events for both $t\bar{t}$+jets production and single top quark processes (t-, s-, and tW-channels) at NLO in quantum chromodynamics (QCD). For the $t\bar{t}$+jets process, corrections to reweight the top quark p_T distribution are applied to match next-to-NLO (NNLO) theoretical computations [179]. NLO matrix element (ME) calculations implemented in `MADGRAPH5_aMC@NLO` [180] are used to generate sample for the top quark pair associated production with a W boson ($t\bar{t}$+W) and a Z boson ($t\bar{t}$+Z) along with up to two additional partons, with the FxFx [181] prescription applied to merge multileg processes. `MADGRAPH5_aMC@NLO` is also used to generate samples of Z+jets and W+jets events (v2.2.2 in 2016, v2.4.2 in 2017 and 2018) at LO prediction with up to four partons in the final state, along with the MLM prescription [182] for matching jets from the ME calculation to the parton shower description. Dedicated electroweak [183–188] and QCD K factors, parameterized as functions of the generated boson p_T, to correct from LO to NLO are also applied to Z+jets and W+Jets events. Samples for QCD multijet events are produced using either `PYTHIA` [189] or `MADGRAPH5_aMC@NLO` plus MLM matching, while other processes with a smaller contribution to the SM background like diboson production are generated at NLO using either `MADGRAPH5_aMC@NLO` with FxFx matching or `POWHEG v2` and normalized to the most accurate cross section calculations available [190, 191].

The $\mathrm{t}/\bar{\mathrm{t}}$+DM and $\mathrm{t}\bar{\mathrm{t}}$ signal processes are simulated at LO with `MADGRAPH5_aMC@NLO` with either zero or one additional parton, respectively, in the ME calculations using the simplified model described in Section 5.1. Following the recommendations of the LHC Dark Matter Working Group [192], benchmark values of $g_{\mathrm{q}} = g_{\chi} = 1$ and $m_{\chi} = 1$ GeV are chosen, with the parameter scan of $m_{\phi/\mathrm{a}}$ from the following list of mass points for both types of mediators and for both $\mathrm{t}/\bar{\mathrm{t}}$+DM and $\mathrm{t}\bar{\mathrm{t}}$ production modes: 50, 100, 150, 200, 250, 300, 350, 400, 450, and 500 GeV. At these mediator mass points where the mediator is produced on-shell, the $\mathrm{p}_{\mathrm{T}}^{\mathrm{miss}}$ distribution of the signal does not depend strongly on m_{χ}, which motivates the choice to set $m_{\chi} = 1$ GeV. Cross sections for the signal processed are calculated at LO using `MADGRAPH5_aMC@NLO` v2.6.1, with zero or one additional parton for $\mathrm{t}/\bar{\mathrm{t}}$+DM and $\mathrm{t}\bar{\mathrm{t}}$ events, respectively.

For samples corresponding to 2016 data, the NNPDF 3.0 [193] PDF set was used, while the NNPDF 3.1 NNLO [194] PDF set was used for samples corresponding to 2017 and 2018 data. Parton shower and hadronization are simulated using `PYTHIA` v8.226 with the CUETP8M1(2) underlying event tune [195] for samples corresponding to 2016 data and the CP5 tune [196] for most samples corresponding to 2017 and 2018 data. The CMS detector simulation was performed using GEANT4 [197] for both signal and background samples. Pileup (PU) effects are also included in all simulated samples, and a reweighting procedure is implemented to match the simulated PU distribution with the one observed in data. In addition, corrections are applied to simulated samples to cover residual differences between data and simulation from lepton identification and reconstruction efficiencies, as well as from b-tagged jet (b-jet) identification efficiencies.

5.3 Object definitions

For the primary vertex, the number of associated tracks must be greater than zero, the number of degrees of freedom defined in Eq. 4.1 $n_{\mathrm{dof}} > 4$, the vertex position along the beampipe $|z_{\mathrm{vtx}}| < 24$ cm, and the vertex distance with respect to the beam pipe $d_0 < 2$ cm. In addition, MC simulated samples are reweighted to match the PU distribution in simulation to data, assuming a total inelastic cross section of $\sigma_{in} = 69.2$ mb.

For leptons, two categories are defined depending on whether the lepton is being selected ("Tight" or "Medium" electrons/muons) or vetoed ("Veto" electrons or "Loose" muons). In general, events containing exactly zero "Veto" leptons are categorized within the AH channel, events containing exactly one "Tight" lepton are categorized in the SL channel, and events containing exactly two "Medium" leptons are categorized within the DL channel.

In the AH and SL channels, electrons are selected or vetoed using the "Tight" and "Veto" cut-based identification working points (WP), respectively. "Tight" electrons are required to have $\mathrm{p_T} > 35$ GeV and $|\eta| < 2.1$. "Veto" electrons with $\mathrm{p_T} > 10$ GeV are used to reject events with extra leptons. For the DL channel, electrons are selected or vetoed using the "Medium" and "Loose" cut-based identification WP. "Medium" electrons are required to have $\mathrm{p_T} > 25(20)$ GeV for leading (trailing) leptons with $|\eta| < 2.4$, while "Loose" electrons are required to have $\mathrm{p_T} > 10$ GeV. For all channels, candidates in the barrel-endcap overlap region in $1.4442 < |\eta| < 1.566$ are removed. The variables and selection criteria defining the electron identification WPs for the different channels are listed in Tables 5.1–5.3.

Muons in the AH and SL channels are also selected or vetoed using "Tight" and "Loose" identification WPs. "Tight" muons are required to have $\mathrm{p_T} > 30$ GeV and $|\eta| < 2.4$, while "Loose" muons are required to have $\mathrm{p_T} > 10$ GeV. In the DL channel, muons are selected using the "Medium" identification WP, with "Medium" muons required to have $\mathrm{p_T} > 25(20)$ GeV for leading (trailing) leptons and $|\eta| < 2.4$. As with the AH and SL channels, a looser requirement of $\mathrm{p_T} > 10$ GeV is used to veto "Loose" muons.

Variable	Barrel ($\|\eta_{\text{sc}}\| < 1.4442$)	Endcap ($1.5660 < \|\eta_{\text{sc}}\| < 2.5$)
$\|\Delta\eta_{In}\|$	0.00463	0.00814
$\|\Delta\phi_{In}\|$	0.148	0.19
full 5×5 $\sigma_{I_\eta I_\eta}$	0.0126	0.0457
$\frac{h}{E}$	$0.05 + 1.16/E_{SC} + 0.0324 * \rho/E_{SC}$	$0.05 + 2.54/E_{SC} + 0.183 * \rho/E_{SC}$
$\frac{1}{E} - \frac{1}{p}$	0.209	0.132
relative electron isolation	$0.198 + 0.506/p_T$	$0.203 + 0.9.63/p_T$
expected missing inner hits	2	3
pass conversion veto	yes	yes

Table 5.1: "Veto" WP electron identification requirements for the AH and SL channels.

	Barrel ($\|\eta_{\text{sc}}\| < 1.4442$)	Endcap ($1.5660 < \|\eta_{\text{sc}}\| < 2.5$)
$\|\Delta\eta_{In}\|$	0.0032	0.00632
$\|\Delta\phi_{In}\|$	0.0547	0.0394
full 5×5 $\sigma_{I_\eta I_\eta}$	0.0106	0.0387
$\frac{h}{E}$	$0.046 + 1.16/E_{SC} + 0.0324 * \rho/E_{SC}$	$0.0275 + 2.52/E_{SC} + 0.183 * \rho/E_{SC}$
$\frac{1}{E} - \frac{1}{p}$	0.184	0.0721
relative electron isolation	$0.0478 + 0.506/p_T$	$0.0658 + 0.963/p_T$
expected missing inner hits	1	1
pass conversion veto	yes	yes

Table 5.2: "Medium" WP electron identification requirements for the DL channel.

Variable	Barrel ($\|\eta_{\text{sc}}\| < 1.4442$)	Endcap ($1.5660 < \|\eta_{\text{sc}}\| < 2.5$)
$\|\Delta\eta_{In}\|$	0.00255	0.00501
$\|\Delta\phi_{In}\|$	0.022	0.0236
full 5×5 $\sigma_{I_\eta I_\eta}$	0.0104	0.0353
$\frac{h}{E}$	$0.026 + 1.15/E_{SC} + 0.0324 * \rho/E_{SC}$	$0.0188 + 2.06/E_{SC} + 0.183 * \rho/E_{SC}$
$\frac{1}{E} - \frac{1}{p}$	0.159	0.0197
relative electron isolation	$0.0287 + 0.506/p_T$	$0.0445 + 0.963/p_T$
expected missing inner hits	1	1
pass conversion veto	yes	yes

Table 5.3: "Tight" WP electron identification requirements for the AH and SL channels.

Variable	“Loose” WP	“Tight” WP
PF-muon	true	true
global muon	-	true
global OR tracker muon	true	-
χ^2/ndof of global muon fit	-	< 10
No. of muon chamber hits in global muon fit	-	≥ 1
No. of muon stations with muon segments	-	≥ 2
$\lvert d_{xz} \rvert$ (cm)	-	< 0.2
$\lvert d_z \rvert$ (cm)	-	< 0.5
No. of pixel hits	-	> 0
No. of tracker layers with hits	-	> 5
relative isolation (separate from ID)	< 0.25	< 0.15

Table 5.4: “Loose” and “Tight” WP muon identification requirements for the AH and SL channels.

Variable	Tracker Muon	Tracker & Global Muon
valid hit fraction	> 0.8	> 0.8
segment compatibility	> 0.451	> 0.303
global fit ($\frac{\chi^2}{\text{dof}}$)	-	< 3
position match (χ^2)	-	< 12
kink (χ^2_{max})	-	< 20

Table 5.5: “Medium” WP muon identification requirements for the DL channel.

The variables and selection criteria defining the muon identification WPs for the different channels are listed in Tables 5.4–5.5.

For both electrons and muons, the relative isolation variable is defined as

$$I_{\text{Rel}}^{\text{PF}} = \frac{I_{\text{ch}} + \max(I_\gamma + I_{\text{nh}} - \rho A_{\text{eff}}, 0)}{\text{p}_{\text{T}}}, \tag{5.4}$$

where I_{ch}, I_γ, and I_{nh} are the respective energies of charged particles, photons, and neutral hadrons within a cone of radius $\Delta R = \sqrt{(\Delta\eta)^2 + (\Delta\phi)^2}$ around the lepton, ρ is the average energy density from PU, A_{eff} is the effective area used to account for PU contributions and background energy, and p_{T} is the transverse momentum of the lepton. This quantity is used to suppress misidentification of prompt leptons from non-prompt or fake leptons, and is used for both electron and muon identification WPs. For electrons, $\Delta R = 0.3$, while for muons, $\Delta R = 0.4$. Muons in all three channels are required to have $I_{\mathrm{Rel}}^{\mathrm{PF}} < 0.15$ while the requirement for electrons depends on their $\mathrm{p_T}$.

In order to account for differences between data and simulation, correction factors called scale factors for lepton reconstruction, identification, and isolation efficiencies are derived using the tag-and-probe method on either the $\mathrm{Z} \rightarrow ee$ (electrons) or $\mathrm{Z} \rightarrow \mu\mu$ (muons) mass peak for all working points separately, as a function of the $\mathrm{p_T}$ and η of the lepton. Corrections are also applied for lepton energy scale and smearing, as well as to match differences between trigger performance in data compared to simulation.

For jets, all three channels use PF AK4 jets (reconstructed with anti-k_t algorithm using $\Delta R = 0.4$) identified with the "TightLepVeto" identification WP, which includes a "Tight" jet PU ID for jets with $\mathrm{p_T} < 50$ GeV. In addition, jets are required to have $\Delta R > 0.$ from any selected leptons (e or μ) in the event to avoid misidentification of leptons as jets. Jet candidates are required to have $\mathrm{p_T} < 30$ GeV for the AH and SL channels and $\mathrm{p_T} > 20$ GeV in the DL channel, as well as $|\eta| < 2.4$ for all jets categorized as "central". In addition, for the AH and SL channels, another category of "forward" jets are defined with the same selections above but with $2.4 < |\eta| < 4.0$. For all channels, corrections are applied to both JES and JER.

For selecting b-tagged jets (b-jets), the medium identification WP of the DeepCSV algorithm is used (see Section 4.6). B-jets are required to have the same $\mathrm{p_T}$ threshold in each channel as central jets and to lie within $|\eta| < 2.4$.

Missing transverse momentum ($\mathrm{p_T^{miss}}$) is calculated and reconstructed based on the algorithm described in Section 4.7. Moreover, several filters are applied to both data and simulation to reject events with known $\mathrm{p_T^{miss}}$ problems. Corrections are applied in addition to the ones outlined in Section 4.7 to address issues during data taking. XY-shift corrections are applied to correct for modulations in the ϕ angular distribution of $\mathrm{p_T^{miss}}$ resulting from several effects, such as anisotropic detector responses, inactive calorimeters, and detector misalignment. Furthermore, noise in the endcap calorimeter of the ECAL (EE) resulted in an overestimation of $\mathrm{p_T^{miss}}$ at high $|\eta|$ during data taking in 2017. As a result, corrections are applied to reduce the effect of this noise on $\mathrm{p_T^{miss}}$.

5.4 Event selection

To search for the signal, this analysis defines several orthogonal signal regions (SRs) that are statistically combined in a simultaneous global fit of the $\mathrm{p_T^{miss}}$ spectrum of the events in those regions. The event selection for the AH and SL channels is based on a selection on discriminating variables in order to increase the signal to background ratio. For the DL channel, a different approach is used. The final state in the DL channel has relatively large $\mathrm{p_T^{miss}}$ in the SM $\mathrm{t\bar{t}}$ process due to the presence of two neutrinos and constitutes the main background in this channel. As a result, the $\mathrm{p_T^{miss}}$ distribution alone is not sufficient to separate signal from background. Instead, sophisticated Multi-Variate Analysis (MVA) techniques are employed to train a neutral network that uses discriminating variables as input to distinguish $\mathrm{t/\bar{t}}$+DM and $\mathrm{t\bar{t}}$ signal processes from SM background.

The SRs in all channels are divided based on the number of b-jets (n_b) identified. The SRs with exactly one b-jet (1b) target the $\mathrm{t/\bar{t}}$+DM process, while the SRs with exactly two or more b-jets (2b) target the $\mathrm{t\bar{t}}$+DM process. In addition, the AH and SL SRs are further subdivided into exactly zero or ≥ 1 forward jet regions (0FJ and 1FJ) to increase the sensitivity to the t-channel $\mathrm{t/\bar{t}}$+DM process, which tends to have a forward jet as shown in Fig. 5.1.

5.4.1 Discriminating variables

In order to separate signal from background, various discriminating variables are defined in the AH, SL, and DL channels:

- **$\mathbf{m_T^b}$ (AH and SL):** The m_T^b variable is defined as

$$m_\mathrm{T}^\mathrm{b} = \sqrt{2\mathrm{p_T^{miss}}p = \mathrm{p_T^b}(1 - \cos(\Delta\phi))}, \tag{5.5}$$

  where $\mathrm{p_T^b}$ is the transverse momentum of the b-jet and $\Delta\phi$ is the opening angle between the b-jet direction and the $\mathrm{p_T^{miss}}$ in the transverse plane. If there is more than one b-jet candidate, the b-jet with the highest DeepCSV discriminant value is chosen. For $\mathrm{t\bar{t}}$ background, m_T^b tends to have values below or around the top quark mass if the b-jet belongs to the top quark whose lepton is not identified.

- $\mathbf{p_T(j_1)/H_T}$ **(AH):** The $\mathrm{p_T(j_1)/H_T}$ variable is defined as the ratio of the leading $\mathrm{p_T}$ jet in the event to $\mathrm{H_T}$, the scalar $\mathrm{p_T}$ sum of all reconstructed jets in the event with $\mathrm{p_T} > 30$ GeV within $|\eta| < 2.4$. The $\mathrm{t\bar{t}}$+DM process, which has six jets at the ME level, tends to have lower values of this observable compared to $\mathrm{t\bar{t}(1l)}$ and $\mathrm{Z} \to \nu\bar{\nu}$ backgrounds, which have fewer jets.

- $\mathbf{min\Delta}\phi\mathbf{(j_{1,2}, p_T^{miss})}$ **(AH and SL):** The $\min\Delta\phi(\mathrm{j_{1,2}}, \mathrm{p_T^{miss}})$ variable is given by the minimum opening angle in the transverse plane between the first two leading $\mathrm{p_T}$ jets and $\mathrm{p_T^{miss}}$. The jets and the $\mathrm{p_T^{miss}}$ vector tend to be more separated in the transverse plane in signal events compared to $\mathrm{t\bar{t}}$ background. In addition, QCD multijet events should not have any intrinsic $\mathrm{p_T^{miss}}$, so the observed $\mathrm{p_T^{miss}}$ in these events is mostly the result of jet measurements where $\mathrm{p_T^{miss}}$ is often aligned with one of the leading jets.

- $\mathbf{m_T}$ **(SL):** The transverse W mass m_T is defined as

$$m_\mathrm{T} = \sqrt{2\mathrm{p_T^{miss}}\mathrm{p_T}^{\ell}(1 - \cos(\Delta\phi))}, \tag{5.6}$$

where $\mathrm{p_T}^{\ell}$ is the transverse momentum of the lepton and $\Delta\phi$ is the opening angle between the lepton and the $\mathrm{p_T^{miss}}$ vector in the transverse plane. The transverse W mass is constrained by kinematic properties to be less than the W boson mass of around 80 GeV for leptonic on-shell W decays in $\mathrm{t\bar{t}}$ and W+jets events. For signals and off-shell W decays or fully leptonic decays of $\mathrm{t\bar{t}}$, m_T is expected to exceed the W mass since the $\mathrm{p_T^{miss}}$ represents more than just one neutrino escaping detection.

- $\mathbf{m_{T2}^W}$ **(SL):** The m_T2^W variable [198] is defined as the minimal value of the mass of a particle assumed to be pair produced and to decay to a W boson and a b quark jet. The W bosons are assumed to be produced on-shell and to decay leptonically, where one of the two leptons is not detected. The calculation of $m_{\mathrm{T2}}^{\mathrm{W}}$ requires two b-jets from the decay of the top quarks, where one of the b-jets comes from the same decay chain as the reconstructed lepton. If only one b-jet is identified in the event, each of the first three (or two in three-jet events) leading non-b-tagged jets is considered as the second b-jet in the calculation. If two or more b-jets are identified in the event, all b-jets are considered and all possible jet-lepton combinations are used to calculate the $m_{\mathrm{T2}}^{\mathrm{W}}$ value. The $m_{\mathrm{T2}}^{\mathrm{W}}$ is then evaluated for all possible jet-lepton combinations and the minimum $m_{\mathrm{T2}}^{\mathrm{W}}$ value is considered to discriminate between signal and background events. Based on the variable definition, in $\mathrm{t\bar{t}(2l)}$ events the $m_{\mathrm{T2}}^{\mathrm{W}}$ has a kinematic end point at the top quark mass, assuming perfect detector response, which is not the case for signal events where two additional DM particles are present.

- **modified topness (SL):** The modified topness variable t[199] minimizes the reconstructed center-of-mass energy of the event, subject to the conditions that both top quarks and W bosons are on-shell. It is defined as

$$t = \ln(\min S), \tag{5.7}$$

where

$$S(\mathrm{p_W}, \mathrm{p}_\nu, \mathrm{z}) = \frac{(m_{\mathrm{W}}^2 - (\mathrm{p}_\nu + \mathrm{p}_1)^2)^2}{a_{\mathrm{W}}^4} + \frac{(m_{\mathrm{t}}^2 - (\mathrm{p_b} + \mathrm{p_W})^2)^2}{a_{\mathrm{t}}^4}, \tag{5.8}$$

where p and m denote the momentum and mass of the particles involved, respectively. The sum in the last term runs over all five assumed final state particles from the top quark and W boson decays. The parameters $a_{\mathrm{W}} = 5$ GeV, $a_{\mathrm{t}} = 15$ GeV, and $a_{\mathrm{CM}} = 1$ GeV determine the relative weighting of the mass shell conditions and correspond to typical resolutions of these particles at LHC conditions. The inputs to the calculation of S are two jets, a lepton, and the $\mathrm{p_T^{miss}}$. The value of t quantifies how well an event is compatible with the $\mathrm{t\bar{t}(2l)}$ hypothesis.

- $\mathbf{m_{T2}^{ll}}$ **(DL):** The $m_{\mathrm{T2}}^{\mathrm{ll}}$ variable [200, 201] is defined as

$$m_{\mathrm{T2}}^{\mathrm{ll}} = \min_{\vec{\mathrm{p}}_{\mathrm{T},\bar{\nu}}+\vec{\mathrm{p}}_{\mathrm{T},\nu}=\vec{\mathrm{p}}_{\mathrm{T}}^{\mathrm{miss}}} \left[\max\{M_{\mathrm{T}}(m_1, m_{\bar{\nu}}, \vec{\mathrm{p}}_{\mathrm{T},1}, \vec{\mathrm{p}}_{\mathrm{T},\bar{\nu}}), M_{\mathrm{T}}(m_{\bar{1}}, m_{\nu}, \vec{\mathrm{p}}_{\mathrm{T},\bar{1}}, \vec{\mathrm{p}}_{\mathrm{T},\nu})\}\right] \quad (5.9)$$

where

$$M_{\mathrm{T}}(m_1, m_{\bar{\nu}}, \vec{\mathrm{p}}_{\mathrm{T},1}, \vec{\mathrm{p}}_{\mathrm{T},\bar{\nu}}) = \sqrt{m_1^2 + m_2^2 + 2(E_{\mathrm{T},1}E_{\mathrm{T},2} - \vec{\mathrm{p}}_{\mathrm{T},1} \cdot \vec{\mathrm{p}}_{\mathrm{T},2})}, \quad (5.10)$$

where m_i, $\vec{\mathrm{p}}_{\mathrm{T,i}}$, and $E_{\mathrm{T,i}}$ correspond to the mass, transverse momentum vector, and transverse energy of the particle i respectively, while $\vec{\mathrm{p}}_{\mathrm{T}}^{\mathrm{miss}}$ is the measured missing transverse momentum vector. This variable offers information on the mass of pair-produced particles in situations where both particles decay to a final state with undetected particles, as in the case of two leptonically decaying W bosons produced from top quark pairs. If the visible components in the decay chain are measured correctly, this variable has a kinematic endpoint at the W boson mass for the $\mathrm{t\bar{t}}$ processes but not for signal, because of the additional $\mathrm{p}_{\mathrm{T}}^{\mathrm{miss}}$ from DM.

In addition to the discriminating variables above, separate variables were used as input to the neural network (NN) trained in the DL channel as well as a separate $\mathrm{t\bar{t}}$ reconstruction algorithm. These inputs include the following:

- $|\Delta\phi(\mathrm{l},\bar{\mathrm{l}})|$, the opening angle between the two leptons.
- $|\Delta\phi(\mathrm{p}_{\mathrm{T}}^{\mathrm{miss}}, \mathrm{l\bar{l}b})|$, the opening angle between the two lepton plus b-jet system and $\mathrm{p}_{\mathrm{T}}^{\mathrm{miss}}$.
- $\mathrm{p}_{\mathrm{T}}^{\mathrm{dark}}$, the amount of $\mathrm{p}_{\mathrm{T}}^{\mathrm{miss}}$ that cannot be assigned to the neutrinos in the top quark kinematic reconstruction algorithm used in the DL channel (see Section 5.4.4).
- c_{hel}, the angle between the two leptons when boosted back into the rest frame of their parent top quarks.

- $|\Delta\phi(\mathrm{t},\bar{\mathrm{t}})|$, the opening angle between the top quark and antiquark.

5.4.2 All hadronic signal regions

In the AH channel, a pre-selection is applied which includes the requirement of no "Veto" or "Loose" electrons or muons, at least one identified b-jet, at least three central jets, and $\mathrm{p}_{\mathrm{T}}^{\mathrm{miss}} > 250$ GeV. To reduce the dominant $\mathrm{t}\bar{\mathrm{t}}$(1l) background, we require the transverse mass $m_{\mathrm{T}}^{\mathrm{b}} > 140$ GeV. To further reduce both $\mathrm{t}\bar{\mathrm{t}}$(1l) and $\mathrm{Z} \to \nu\bar{\nu}$ background events, we also require $\mathrm{p}_{\mathrm{T}}(\mathrm{j}_1)/\mathrm{H}_{\mathrm{T}} < 0.5$ in the $n_{\mathrm{b}} \geq 2$ SRs. No requirement on $\mathrm{p}_{\mathrm{T}}(\mathrm{j}_1)/\mathrm{H}_{\mathrm{T}}$ is applied in the $n_{\mathrm{b}} = 1$ SRs since $\mathrm{t}/\bar{\mathrm{t}}$+DM events have fewer central jets, and therefore tend to exhibit a distribution similar to that of the background. To reduce QCD multijet background, a minimum selection of $\min\Delta\phi(\mathrm{j}_{1,2}, \mathrm{p}_{\mathrm{T}}^{\mathrm{miss}}) > 0.8$ radians is also applied.

Final SR event selections for the AH channel are summarized in Table 5.6, while the $\mathrm{p}_{\mathrm{T}}^{\mathrm{miss}}$ distributions of the AH SRs after the fit described in Section 5.7 are shown in Fig. 5.2. The lower panels show the ratio of data and the SM prediction after the maximum likelihood fit is performed. The hatched uncertainty bands represent the total combined statistical and systematic uncertainties in the prediction.

	All hadronic SRs		
	0l, 1b, 0FJ	0l, 1b, 1FJ	0l, 2b
n_{lep}		= 0	
n_{jet}		≥3	
n_{b}	=1	=1	≥2
Forward jets	=0	≥1	—
$\mathrm{p}_{\mathrm{T}}(\mathrm{j}_1)/\mathrm{H}_{\mathrm{T}}$	—		<0.5
$\mathrm{p}_{\mathrm{T}}^{\mathrm{miss}}$ [GeV]		>250	
m_{T} [GeV]		—	
$m_{\mathrm{T2}}^{\mathrm{W}}$ [GeV]		—	
$\min\Delta\phi(\mathrm{j}_{1,2}, \mathrm{p}_{\mathrm{T}}^{\mathrm{miss}})$ [rad.]		>0.8	
$m_{\mathrm{T}}^{\mathrm{b}}$ [GeV]		>140	

Table 5.6: Final event selections for the AH channel SRs.

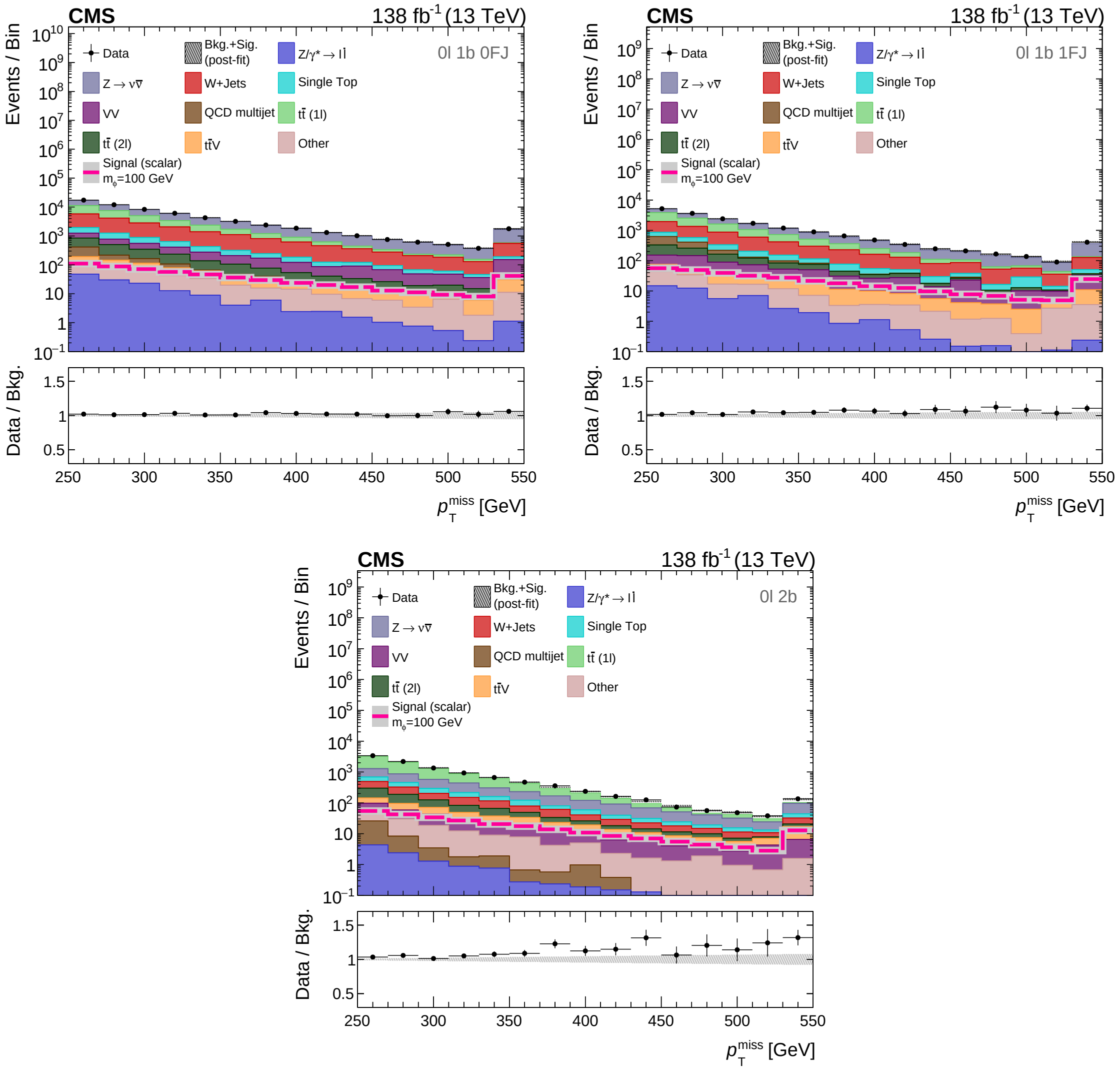

Figure 5.2: The p_T^{miss} distributions for the 1b 0FJ (top left), 1b 1FJ (top right), and 2b (bottom) AH SRs. The last bin contains overflow events. A representative signal model distribution is shown. The gray dashed area in the upper panel represents the total uncertainty in all of the backgrounds and the chosen signal model, while in the lower panel it represents only the total uncertainty in the backgrounds.

5.4.3 Single lepton signal regions

In the SL channel, a pre-selection is applied which includes the requirement of exactly one "Tight" lepton (e or μ), at least one identified b-jet, at least two central jets, and $\mathrm{p_T^{miss}} > 250$ GeV. To reduce the dominant $\mathrm{t\bar{t}}$ and W+jets background, we require that the transverse mass $m_\mathrm{T} > 140$ GeV. After the m_T selection, the remaining $\mathrm{t\bar{t}}$(2l) background is further reduced by requiring $m_\mathrm{T2}^\mathrm{W} > 180$ GeV and $m_\mathrm{T}^\mathrm{b} > 140$ GeV. Like with the AH channel SRs, a requirement of $\min\Delta\phi(\mathrm{j}_{1,2}, \mathrm{p_T^{miss}}) > 0.8$ radians is also applied to help separate signal from $\mathrm{t\bar{t}}$ background events. Finally, separate SR categories are defined based on the value of the modified topness variable t. Rather than defining a single selection criterion on this variable, we split the SRs in the SL channel into two further categories $t \leq 0$ (T1) and $t > 0$ (T2).

Final SR event selections for the SL channel are summarized in Table 5.7, while the $\mathrm{p_T^{miss}}$ distributions of the SL SRs after the fit described in Section 5.7 are shown in Fig. 5.3. The lower panels show the ratio of data and the SM prediction after the maximum likelihood fit is performed. The hatched uncertainty bands represent the total combined statistical and systematic uncertainties in the prediction.

	Single lepton SRs		
	1l, 1b, 0FJ	1l, 1b, 1FJ	1l, 2b
n_lep		= 1	
n_jet		≥2	
n_b	=1	=1	≥2
Forward jets	=0	≥1	—
$\mathrm{p_T(j_1)/H_T}$		—	
$\mathrm{p_T^{miss}}$ [GeV]		>250	
m_T [GeV]		>140	
m_T2^W [GeV]		>180	
$\min\Delta\phi(\mathrm{j}_{1,2}, \mathrm{p_T^{miss}})$ [rad.]		>0.8	
m_T^b [GeV]		>140	

Table 5.7: Final event selections for the SL channel SRs. For the SL channel, a categorization in terms of modified topness, with bins of $t \leq 0$ and $t > 0$, is also applied after the event selection.

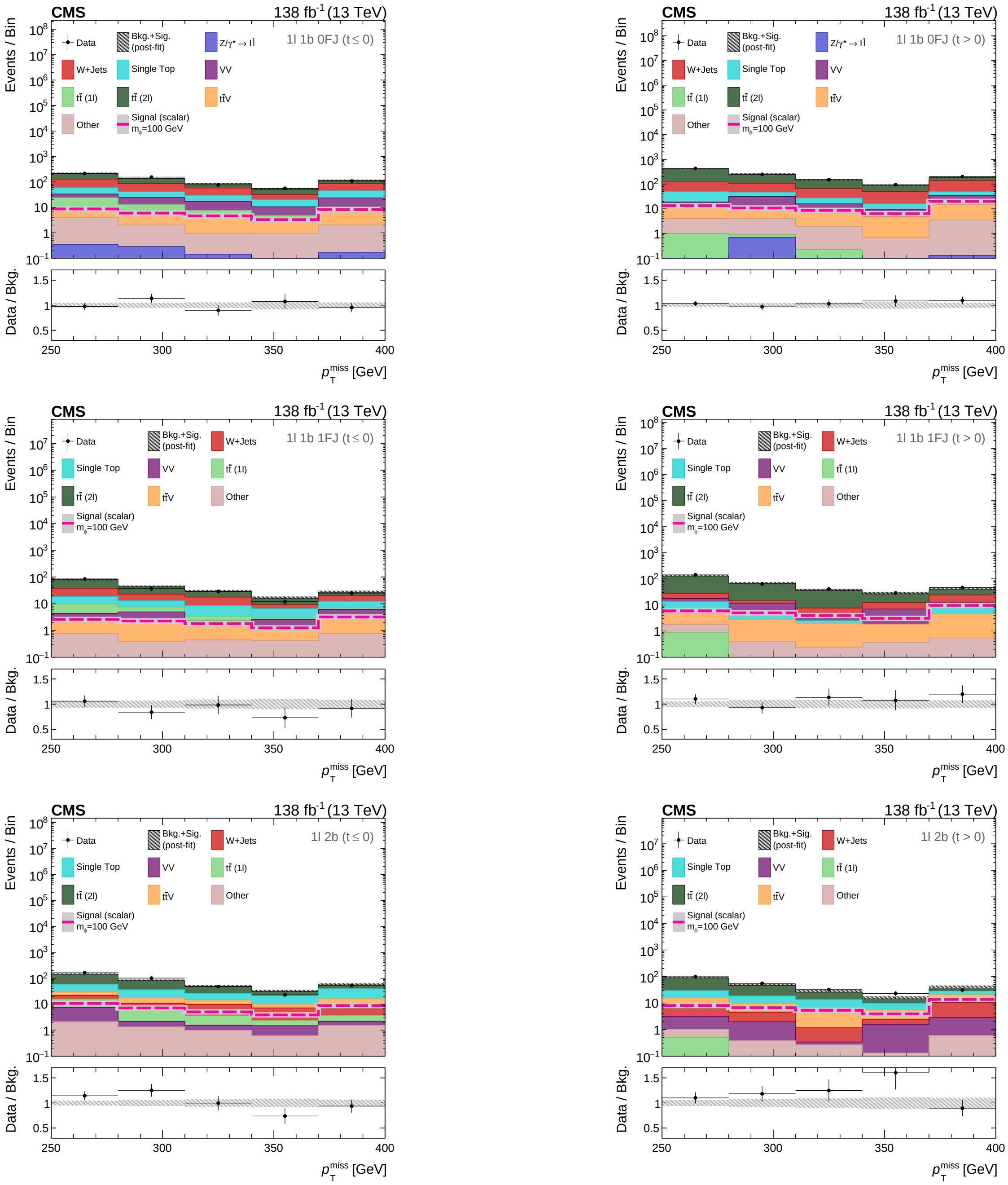

Figure 5.3: The p_T^{miss} distributions for the 1b 0FJ ($t \leq 0$) (top left), 1b 0FJ ($t > 0$) (top right), 1b 1FJ ($t \leq 0$) (center left), 1b 1FJ ($t > 0$) (center right), 1l 2b ($t \leq 0$) (bottom left), and 1l 2b ($t > 0$) (bottom right) SL SRs. The last bin contains overflow events. A representative signal model distribution is shown. The gray dashed area in the upper panel represents the total uncertainty in all of the backgrounds and the chosen signal model, while in the lower panel it represents only the total uncertainty in the backgrounds.

5.4.4 Dilepton signal regions

In the DL channel, a pre-selection is applied which includes the requirement of exactly two "Medium" leptons (e or μ), at least one b-jet, and $m_{\mathrm{ll}} > 20$ GeV for the invariant mass m_{ll} of the two leptons in order to suppress light resonances. The region $76 < m_{\mathrm{ll}} < 106$ GeV is also excluded to suppress Drell-Yan (DY) production. Since this channel is also dominated by $\mathrm{t}\bar{\mathrm{t}}$ background events, a selection of $m_{\mathrm{T2}}^{\mathrm{ll}} > 80$ GeV is imposed. Though most of the remaining background is well modeled by MC simulation, the DY process is particularly difficult to model as it normally only enters the selection if the $\mathrm{p}_{\mathrm{T}}^{\mathrm{miss}}$ and hence the $m_{\mathrm{T2}}^{\mathrm{ll}}$ is significantly mismodeled. Thus, the SRs in the DL channel are further split by lepton flavor into same flavor (SF) regions with either two electrons or two muons, that will be relatively enriched in the DY process, and different flavor (DF) regions with one electron and one muon, that will be depleted in DY events. A method is then used to estimate the DY background in the more enriched $\mathrm{t}/\bar{\mathrm{t}}$+DM SF region based on control samples in data (see Section 5.5.3).

As mentioned previously, a separate NN is trained on a number of discriminating variables in each of the 1b and 2b regions for the combined SF and DF lepton regions for both scalar and pseudoscalar mediator hypotheses in order to distinguish signal from background. Only one NN is trained for all mediator mass hypotheses since the performance of the NN did not seem to significantly improve when training on a single mass point compared to the ensemble of all mass points. In the 2b region, a $\mathrm{t}\bar{\mathrm{t}}$ reconstruction algorithm [202] is also applied, which takes as input the top quark kinematic properties $p_{\mathrm{T}}^{\mathrm{dark}}$, c_{hel}, and $|\Delta\phi(\mathrm{t},\bar{\mathrm{t}})|$. The NNs were trained using Keras [203] with a Tensorflow [204] backend, with three densely connected hidden layers using the rectified linear unit (ReLU) activation function and an output layers with nodes for signal and background using the "softmax" activation function. The distributions of the output of the NN score were used for signal extraction.

Final SR event selections for the DL channel are summarized in Table 5.8, while the NN output distributions of the SL SRs after the fit described in Section 5.7 are shown in Fig. 5.4. The lower panels show the ratio of data and the SM prediction after the maximum likelihood fit is performed. The hatched uncertainty bands represent the total combined statistical and systematic uncertainties in the prediction.

	Dilepton SRs	
	2l, 1b	2l, 2b
n_{lep}	= 2	
n_{jet}	≥ 1	
n_{b}	=1	≥ 2
Forward jets	—	—
$\mathrm{p_T}(\mathrm{j}_1)/\mathrm{H_T}$	—	
$\mathrm{p_T^{miss}}$ [GeV]	—	
m_{T} [GeV]	—	
$m_{\mathrm{T2}}^{\mathrm{W}}$ [GeV]	—	
$\min \Delta\phi(\mathrm{j}_{1,2}, \mathrm{p_T^{miss}})$ [rad.]	—	
$m_{\mathrm{T}}^{\mathrm{b}}$ [GeV]	—	
m_{ll} [GeV]	>20	
$\lvert m_{\mathrm{ll}} - m_{\mathrm{Z}} \rvert$ [GeV]	> 15 (SF)	
$m_{\mathrm{T2}}^{\mathrm{ll}}$ [GeV]	>80	
Pass $\mathrm{t\bar{t}}$ reco	—	yes

Table 5.8: Final event selections for the DL channel SRs. For the DL channel, an additional selection is also applied after event selection into same flavor (SF) $e^+e^-/\mu^+\mu^-$ and different flavor (DF) $e^\pm\mu^\pm$ regions.

5.5 Background estimation

After the event selections described in Section 5.4, we can focus on the main SM backgrounds in the different search regions. For the AH channel, the main backgrounds arise from single lepton $\mathrm{t\bar{t}}$(1l) events where the lepton is lost, W+jets events, and $\mathrm{Z} \to \nu\nu$ events where the two neutrinos leads to background with genuine $\mathrm{p_T^{miss}}$. For the SL channel, the main backgrounds are dileptonic $\mathrm{t\bar{t}}$(2l) events where one lepton is lost, and W+jets events. For the DL channel, the main backgrounds are $\mathrm{t\bar{t}}$(2l) and tW events, DY production, and $\mathrm{t\bar{t}Z} \to \mathrm{t\bar{t}}\nu\bar{\nu}$ processes.

Different strategies are employed to improve or verify the modeling of these backgrounds based on data driven control methods. For the AH and SL channels, signal depleted control regions are defined which are enhanced in the different background sources.

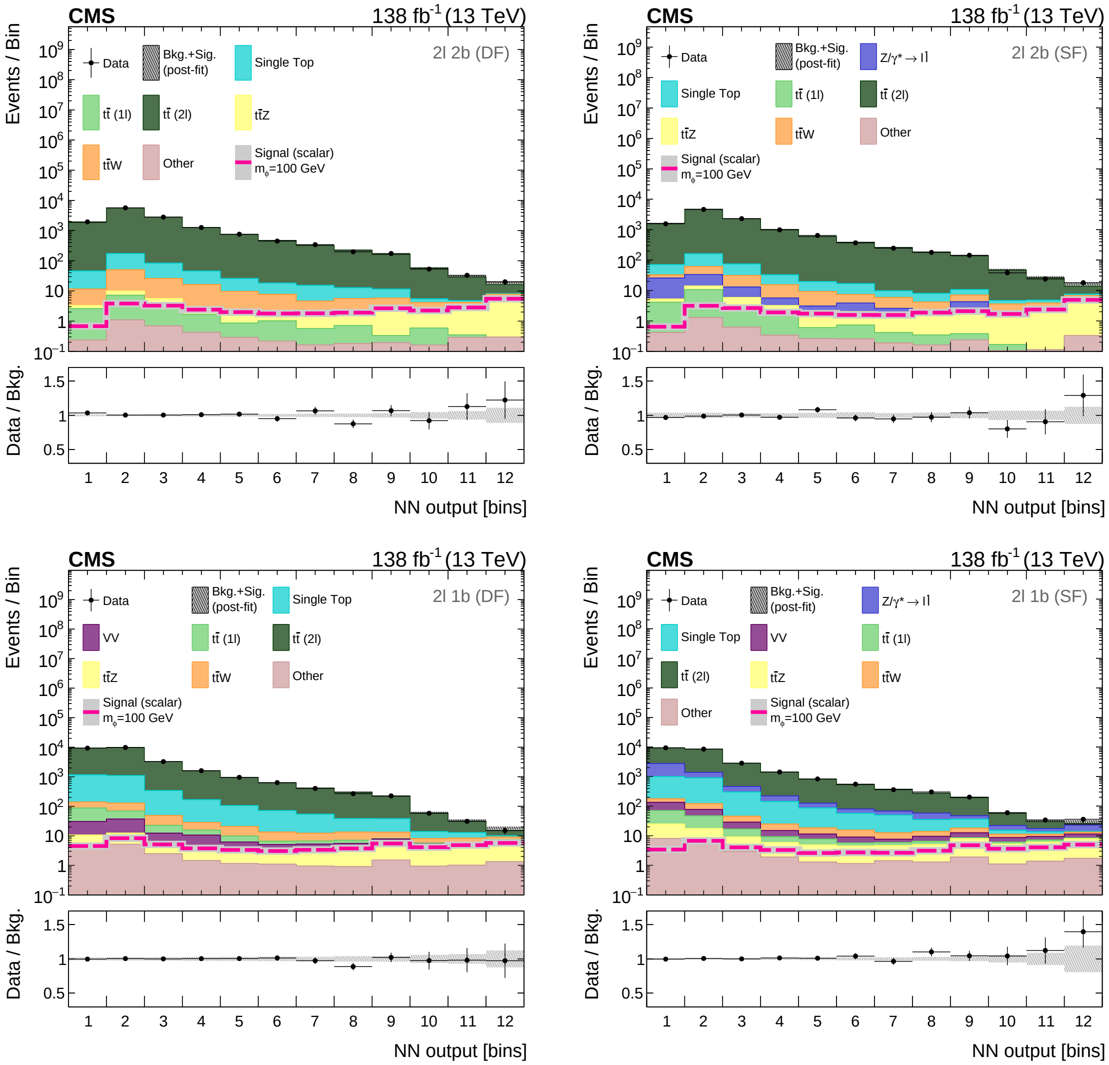

Figure 5.4: The NN output distributions for the 2b (DF) (top left), 2b (SF) (top right), 1b (DF) (bottom left), and 1b (SF) (bottom right) DL SRs. The last bin contains overflow events. A representative signal model distribution is shown. The gray dashed area in the upper panel represents the total uncertainty on all of the backgrounds and the chosen signal model, while in the lower panel it represents only the total uncertainty on the backgrounds.

If necessary, correction factors are then derived on a bin-by-bin basis that depends on the ratio of data to MC prediction. These correction factors are then extracted simultaneously across the CRs and SRs for a given channel in the context of a global fit (see Section 5.7). The remaining SM backgrounds are estimated from MC simulation.

For the DL channel, dedicated CRs are also defined for the DY and $\mathrm{t\bar{t}Z} \rightarrow \mathrm{t\bar{t}}\nu\bar{\nu}$ processes. For the DY process, correction factors are derived as a function of the NN score in a similar way to the AH and SL channels, while for $\mathrm{t\bar{t}Z} \rightarrow \mathrm{t\bar{t}}\nu\bar{\nu}$, only an overall normalization factor is derived. In addition, a validation region (VR) enriched in both $\mathrm{t\bar{t}}$ and tW events is defined in order to verify that these events are correctly modeled for all the input variables used in the NN. These distributions show good agreement between data and simulation within uncertainties for all variables, so no further correction factor is applied.

5.5.1 All hadronic control regions

In the AH channel, four independent sets of CRs are defined. The first set of CRs is designed to be enhanced in $\mathrm{t\bar{t}}$(1l) events by selecting events with exactly one "Tight" lepton, at least three central jets, at least one b-jet, $\mathrm{p_T^{miss}} > 250$ GeV, and $\min \Delta\phi(\mathrm{j}_{1,2}, \mathrm{p_T^{miss}}) \geq 0.8$ radians. In addition, a selection of $m_\mathrm{T} < 140$ GeV is applied to avoid overlap with the SL SRs. A second set of CRs is designed to be enhanced in single lepton W+Jets events by selecting events with exactly one "Tight" lepton, at least three central jets, no b-jets, $\mathrm{p_T^{miss}} > 250$ GeV, and $m_\mathrm{T} < 140$ GeV in order to avoid overlap with the SL W+jets CR.

A third set of CRs are designed to model background originating from Z→ $\nu\nu$ processes, where Z boson decays to an opposite sign SF dilepton pair (Z→ll) are used as proxy events to emulate the kinematic properties of the Z→ $\nu\nu$ process. To reproduce the $\mathrm{p_T}$ spectrum of Z→ $\nu\nu$ events, the two leptons in the Z→ll event are added to the $\mathrm{p_T^{miss}}$ vector to compute a quantity referred to as hadronic recoil, whose magnitude is required to be greater than 250 GeV. In addition, events are also required to have exactly two "Tight" leptons with SF and opposite signs (e^+e^- or $\mu^+\mu^-$) that satisfy the requirement $60 < m_\mathrm{ll} < 120$ GeV on their invariant mass, at least three central jets, and no b-jets.

The final set of CRs is designed to be enhanced in QCD multijet events. Though QCD multijet events are not a dominant background in the AH SRs, they are poorly modeled in simulation due to the fact that to pass the minimum p_T^{miss} requirement, these events need to have significant jet mismeasurements. This mismodeling leads to large systematic uncertainties, so a dedicated CR is defined for QCD multijet background in order to reduce their associated uncertainties by estimating their yield from data. Events in this CR must have no "Veto" leptons, at least three central jets, at least one b-jet, and $p_T^{miss} > 250$ GeV. We also require $\min\Delta\phi(j_{1,2}, p_T^{miss}) < 0.8$ radians since events with significant jet mismeasurement tend to have the p_T^{miss} vector aligned with one of the leading jets.

Final CR event selections for the AH channel are summarized in Table 5.9, while the p_T^{miss} distributions of the AH CRs after the fit described in Section 5.7 are shown in Fig. 5.5. The lower panels show the ratio of data and the SM prediction after the maximum likelihood fit is performed. The hatched uncertainty bands represent the total combined statistical and systematic uncertainties in the prediction.

	AH CRs			
	$t\bar{t}(1l)$ CR	$W(l\nu)$ CR	$Z(2l)$ CR	QCD CR
n_b	≥ 1	$= 0$	$= 0$	≥ 1
n_{lep}	$= 1$	$= 1$	$= 2$	$= 0$
n_{jet}	≥ 3	≥ 3	≥ 3	≥ 3
p_T^{miss} [GeV]	≥ 250	≥ 250	≥ 250	≥ 250
m_T [GeV]	≤ 140	≤ 140	—	—
$\min\Delta\phi(j_{1,2}, p_T^{miss})$ [rad.]	≥ 0.8	—	—	< 0.8
m_{ll} [GeV]	—	—	$[60, 120]$	—
$\lvert m_{ll} - m_Z\rvert$ [GeV]	—	—	—	—
m_{T2}^{ll} [GeV]	—	—	—	—
Included in fit?	Yes	Yes	Yes	Yes

Table 5.9: CRs defined for the main backgrounds of the AH SRs ($t\bar{t}(1l)$, W+jets, Z→ll, QCD). Some selection criteria applied in the SRs are removed in the corresponding CRs to increase the event counts and are therefore not listed. The p_T^{miss} selection for the Z→ll CR refers to the hadronic recoil.

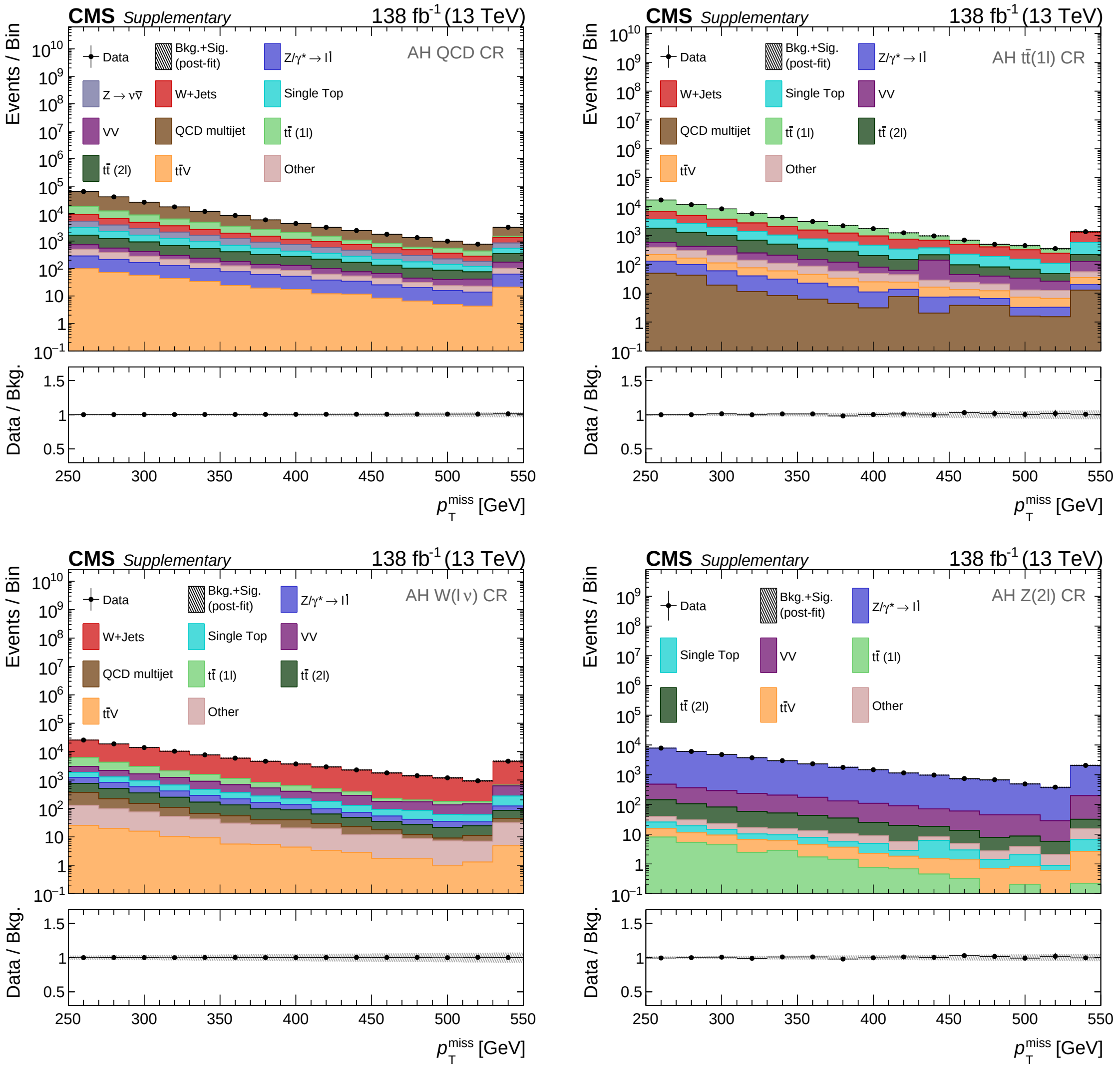

Figure 5.5: The p_T^{miss} distributions for the QCD (top left), $t\bar{t}$(1l) (top right), W(lν) (bottom left), and Z(2l) (bottom right) AH CRs. The last bin contains overflow events. The gray dashed area in the upper panel represents the total uncertainty on all of the backgrounds and the chosen signal model, while in the lower panel it represents only the total uncertainty on the backgrounds.

5.5.2 Single lepton control regions

In the SL channel, two independent sets of CRs are defined. The first set of CRs is designed to isolate $\mathrm{t\bar{t}(2l)}$ events by selecting events with exactly two "Tight" leptons, at least 2 central jets, at least one b-jet, and $\mathrm{p_T^{miss}} > 250$ GeV. In addition, events are required to have $m_{\mathrm{T2}}^{\mathrm{ll}} < 80$ GeV to avoid overlap with the DL SRs. The m_{T}, $m_{\mathrm{T2}}^{\mathrm{W}}$, and forward jet selections are also removed to increase the statistical power of this CR. The second set of CRs is designed to isolate W+jets events by selecting events with exactly one "Tight" lepton, at least two central jets, no b-jets, $\mathrm{p_T^{miss}} > 250$ GeV, and $m_{\mathrm{T}} > 140$ GeV. The zero b-jet requirement is imposed to avoid overlap with the SL SRs.

Final CR event selections for the SL channel are summarized in Table 5.10, while the $\mathrm{p_T^{miss}}$ distributions of the SL CRs after the fit described in Section 5.7 are shown in Fig. 5.6. The lower panels show the ratio of data and the SM prediction after the maximum likelihood fit is performed. The hatched uncertainty bands represent the total combined statistical and systematic uncertainties in the prediction.

	SL CRs	
	$\mathrm{t\bar{t}(2l)}$ CR	$\mathrm{W(l\nu)}$ CR
n_{b}	≥ 1	$= 0$
n_{lep}	$= 2$	$= 1$
n_{jet}	≥ 2	≥ 2
$\mathrm{p_T^{miss}}$ [GeV]	≥ 250	≥ 250
m_{T} [GeV]	—	≥ 140
$\min \Delta\phi(\mathrm{j_{1,2}}, \mathrm{p_T^{miss}})$ [rad.]	—	—
m_{ll} [GeV]	—	—
$\lvert m_{\mathrm{ll}} - m_{\mathrm{Z}} \rvert$ [GeV]	—	—
$m_{\mathrm{T2}}^{\mathrm{ll}}$ [GeV]	≤ 80	≤ 80
Included in fit?	Yes	Yes

Table 5.10: CRs defined for the main backgrounds of the SL SRs ($\mathrm{t\bar{t}(2l)}$ and W+jets). Some selection criteria applied in the SRs are removed in the corresponding CRs to increase the event counts and are therefore not listed. The $\mathrm{p_T^{miss}}$ selection for the Z→ll CR refers to the hadronic recoil.

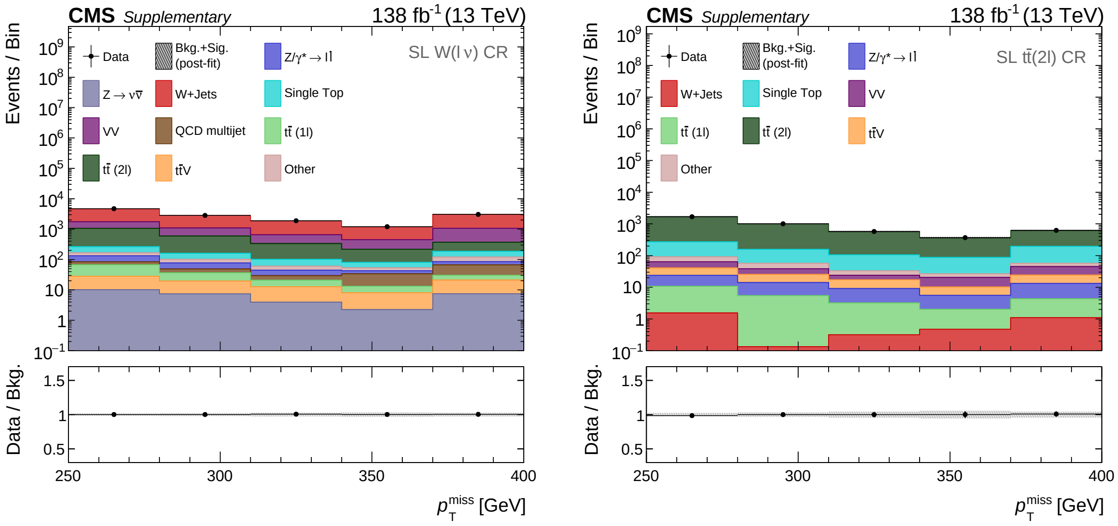

Figure 5.6: The $\mathrm{p_T^{miss}}$ distributions for the $\mathrm{W(l}\nu)$ (left) and $\mathrm{t\bar{t}(2l)}$ (right) SL CRs. The last bin contains overflow events. The gray dashed area in the upper panel represents the total uncertainty on all of the backgrounds and the chosen signal model, while in the lower panel it represents only the total uncertainty on the backgrounds.

5.5.3 Dilepton control regions

In the DL channel, one VR and two independent CRs are defined. The VR is designed to be enhanced in $\mathrm{t\bar{t}(2l)}$ events by selecting events with exactly two "Medium" leptons, at least one jet, at least one b-tagged jet, $m_{\mathrm{ll}} > 20$ GeV with $m_{\mathrm{ll}} < 76$ or $m_{\mathrm{ll}} > 106$ GeV for SF leptons, and $m_{\mathrm{T2}}^{\mathrm{ll}} \leq 80$ GeV to avoid overlap with the DL SRs. The first CR is designed to be enhanced in DY events by selecting events with exactly two SF "Medium" leptons, at least one jet, at least one b-jet, $76 < m_{\mathrm{ll}} > 106$ GeV, and $m_{\mathrm{T2}}^{\mathrm{ll}} > 80$ GeV. Since the 2b SRs were found to not be dominated by DY events even inside the Z boson mass window, a single CR requiring exactly 1 b-jet is used to predict the rate of DY in the 1b SF SR as a function of the NN score.

The second CR is designed to be enhanced in $\mathrm{t\bar{t}Z}$ events by selecting events with exactly three "Medium" leptons with $\mathrm{p_T} > 25, 20, 20$ GeV respectively, at least three jets with $\mathrm{p_T} > 30$ GeV for the leading jet and $\mathrm{p_T} > 20$ GeV for all others, and at least one b-jet. In addition, events are required to have an OS SF lepton pair with $|m_{\mathrm{ll}} - m_{\mathrm{Z}}| < 10$ GeV, with the remaining lepton having $\mathrm{p_T} > 35$ GeV to suppress DY events with a misidentified lepton. Events are binned in terms of jet and b-jet multiplicity in order to maximize the discrimination of $\mathrm{t\bar{t}Z}$ processes from the remaining backgrounds.

Final VR and CR event selections for the DL channel are summarized in Table 5.11, while the NN output distributions of the DL CRs after the fit described in Section 5.7 are shown in Fig. 5.7. The lower panels show the ratio of data and the SM prediction after the maximum likelihood fit is performed. The hatched uncertainty bands represent the total combined statistical and systematic uncertainties in the prediction.

	DL CRs		
	$\mathrm{t\bar{t}}$(2l) VR	DY CR	$\mathrm{t\bar{t}Z}$ CR
n_b	≥ 1	$= 1$	≥ 1
n_lep	$= 2$	$= 2$ (SF)	$= 3$
n_jet	≥ 1	≥ 1	≥ 3
$\mathrm{p_T^{miss}}$ [GeV]	—	—	—
m_T [GeV]	—	—	—
$\min\Delta\phi(\mathrm{j}_{1,2}, \mathrm{p_T^{miss}})$ [rad.]	—	—	—
m_ll [GeV]	> 20	—	—
$\lvert m_\mathrm{ll} - m_\mathrm{Z}\rvert$ [GeV]	> 15 (SF)	< 15	< 10 (OS SF)
$m_\mathrm{T2}^\mathrm{ll}$ [GeV]	≤ 80	≥ 80	—
Included in fit?	No	Yes	Yes

Table 5.11: CRs defined for the main backgrounds of the DL SRs ($\mathrm{t\bar{t}}$(2l) and $\mathrm{t\bar{t}Z}$). Some selection criteria applied in the SRs are removed in the corresponding CRs to increase the event counts and are therefore not listed. The $\mathrm{p_T^{miss}}$ selection for the Z→ll CR refers to the hadronic recoil.

5.6 Systematic uncertainties

The systematic uncertainties in this analysis can arise from various sources and affect both signal and background processes. Two types of systematic uncertainties are considered; those that only affect the total overall yield of a process (normalization uncertainties), and those that in addition affect its distribution (shape uncertainties). Normalization uncertainties include the following:

- **Luminosity:** Uncertainties of 1.2%, 2.3%, and 2.5% are applied for 2016, 2017, and 2018 data taking years in order to account for uncertainties in the actual integrated

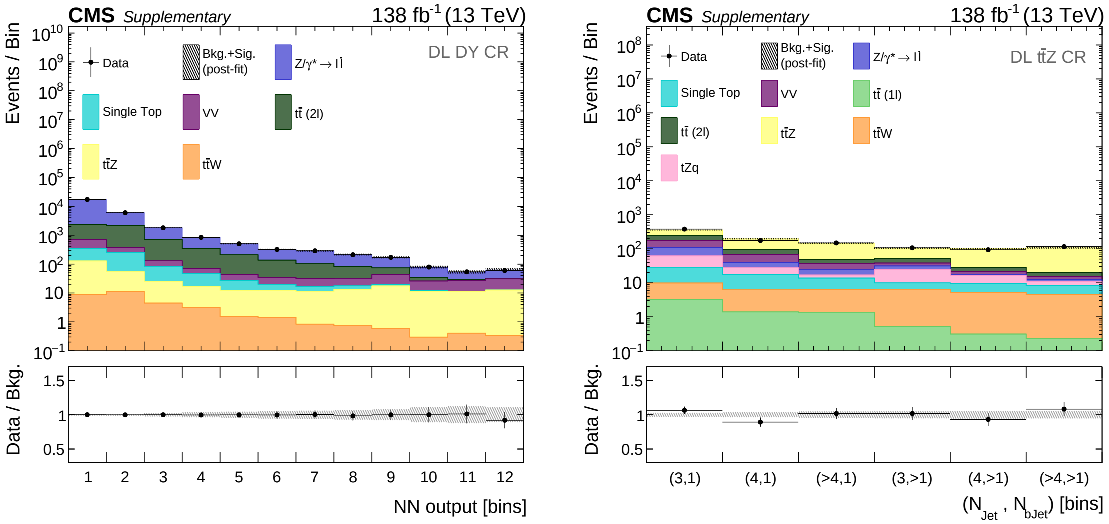

Figure 5.7: The NN output distributions for the DY (left) and $t\bar{t}Z$ (right) DL CRs. The last bin contains overflow events. The gray dashed area in the upper panel represents the total uncertainty on all of the backgrounds and the chosen signal model, while in the lower panel it represents only the total uncertainty on the backgrounds.

luminosity for these years [205–207].

- **Single top quark background normalization (AH and SL):** An uncertainty of 20% is applied on the normalization for single top quark processes considered in order to account for uncertainty from varying the factorization and renormalization scales as well as in the PDF.

The shape uncertainties considered in the analysis include the following:

- **PDF:** Uncertainties on the choice of PDF and α_s are estimated by reweighting the samples with the relevant PDF replicas according to PDF4LHC recommendations for the LHC Run 2 [208].

- **Factorization and renormalization scales:** Uncertainties due to the renormalization scale μ_R and the factorization scale μ_F in simulation ME generators are taken into account by applying a set of weights that represent a change of these scales by a factor of 2 or 0.5. For processes where the rate is estimated from data in a CR, these are normalized to cover only the acceptance effects.

- **Parton shower modeling:** Variations in the parton shower initial and final state radiation (ISR and FSR) scales are also considered by independently varying these up and down by a factor of 2.

- **Pileup modeling:** Systematic uncertainties due to PU modeling are taken into account by varying the minimum bias cross section of 69 mb used to calculate the PU distributions in data by ±4.6% [209].

- **Trigger:** Separate uncertainties are considered for the triggers used in each channel. These are estimated using cross-checks of the methods used to compute them from control samples in data.

- **Lepton reconstruction and selection:** Uncertainties on the order of $\sim$2% are applied to MC processes where scale factors have been applied to mimic lepton reconstruction and selection efficiencies in data.

- **Jet energy scale and resolution:** The full uncertainty for the JES is split into 27 uncorrelated sources, which are propagated to all discriminating variables affected. In addition, the $\mathrm{p_T}$ of the jets is stochastically varied within the resolution of the detector and also propagated to all discriminating variables affected, such as $\mathrm{p_T^{miss}}$.

- **$\mathbf{p_T^{miss}}$ mismodeling:** The uncertainties on jets, electrons, and muons that are used to reconstruct $\mathrm{p_T^{miss}}$ are applied to the respective objects, while the $\mathrm{p_T^{miss}}$ is recalculated with the same variations. In addition, any unclustered energy not assigned to any object is also varied within its uncertainties, and the impact of these variations is propagated to $\mathrm{p_T^{miss}}$.

- **B-tagging efficiency scale factors:** In order to account for differences in b-tagging efficiency in data and simulation, $\mathrm{p_T}$, η, and flavor dependent scale factors are applied to MC samples. The uncertainties associated with these scale factors are also propagated to the analysis, including components that are either fully correlated across years or fully uncorrelated across years. Furthermore, these uncertainties are treated as uncorrelated between the AH/SL and DL channels due to differences in the phase space targeted by the SR selections.

- **Simulation sample size:** Each bin of the distributions used in the signal extraction are allowed to fluctuate independently according to their statistical uncertainties which arise from the limited size of simulated signal and background samples [210].

- **Uncertainty related to ECAL mistiming:** Partial mistiming of signals in the forward regions of the ECAL endcaps led to a reduction in the L1 trigger efficiency in 2016 and 2017. Corrections are applied to simulation to mimic the behavior in data and the uncertainty of these corrections are propagated to the final distributions used for signal extraction.

- **Electroweak and QCD K factors (AH and SL)** Shape uncertainties for the NLO/LO K factors calculated for W+jets and Z+jets processes are considered to account for missing higher order corrections. For QCD processes, these uncertainties come from variations due to factorization and normalization scales. For electroweak processes, an estimate of the size of the missing higher-order corrections is obtained by taking the difference between applying and not applying the NLO/LO electroweak K factors.

- **W/Z+heavy-flavor fraction (AH and SL):** The relative contribution of W/Z+heavy-flavor (HF) jets in W+jets and Z+jets events is allowed to vary within 20% separately and independently for the 1b and 2b regions in order to estimate the uncertainty in the fraction of W/Z+HF jets in these events.

- **B-tagged jet multiplicity normalization:** Normalization scale factors are applied to both W+jets and Z+jets processes in 2017 and 2018 to correct the b-jet multiplicity distributions in the AH and SL channels. An uncertainty of 5% is applied to account for systematic variations in these scale factors.

- **Top quark $\mathrm{p_T}$ reweighting (DL):** In the DL channel, $\mathrm{p_T}$ dependent scale factors are applied to correct for differences in the top quark p_T spectrum in NNLO QCD simulation compared to NLO simulation [211]. The uncertainty associated with this reweighting is estimated by taking the difference between applying and not applying the reweighting.

Theory-related uncertainties such as the variation in the factorization and renormalization scales, the PDF choice, the parton showering scales, the uncertainty in the inelastic cross section, and others, are treated as fully correlated across all channels and years of data taking. In addition, experimental sources of uncertainties such as lepton identification and isolation efficiencies, trigger efficiencies, and ECAL mistiming are considered fully correlated, along with a subgroup of 13 nuisance parameters affecting the JES. Some nuisance parameters are considered in the signal extraction with a partial correlation scheme, including uncertainties from sources such as b-tagging efficiency, which is split into subsources that are either considered fully correlated or completely uncorrelated across data taking periods. The remaining 14 parameters of the JES subsources are also treated as decorrelated between different years but correlated across the different channels. Similarly, the uncertainty associated with the integrated luminosity is kept uncorrelated across different years, but fully correlated between channels. The rest of the systematics are treated as fully uncorrelated, except for uncertainties associated with JER and the unclustered component of p_T^{miss}, which are kept correlated across the different channels.

5.7 Signal extraction

To extract the signal, a simultaneous maximum likelihood fit [212] to the p_T^{miss} and NN output distributions in the AH/SL and DL channels, respectively, is performed using the CMS statistical analysis tool `COMBINE` [213], which is based on the `ROOFIT` [214] and `ROOSTATS` [215] frameworks. From the fit, parameters for the signal strength can be estimated. To perform the fit, we first construct a binned likelihood function given by

$$\mathcal{L}(\text{data}|\mu,\theta) = \text{Poisson}(\text{data}|\mu \cdot s(\theta) + b(\theta)) \cdot p(\tilde{\theta}|\theta). \tag{5.11}$$

In Eq. 5.11, μ is a parameter representing the signal strength modifier, while θ represents all the nuisance parameters corresponding to the uncertainties considered in the fit. The terms $s(\theta)$ and $b(\theta)$ represent the signal and background event yields per bin and are functions of the nuisance parameters. The probability density functions (PDF) $p(\tilde{\theta}|\theta)$ are related to the systematic error PDFs $\rho(\theta|\tilde{\theta})$ by Bayes' theorem

$$\rho(\theta|\tilde{\theta}) \sim p(\tilde{\theta}|\theta) \cdot \pi_\theta(\theta), \tag{5.12}$$

where $\tilde{\theta}$ is the default value of the nuisance parameter and $\pi_\theta(\theta)$ are functions representing the hyper-priors for the nuisance parameters. The term "data" represents the actual event yields observed in data and is used to construct the sampling distributions later on in the fit. The Poisson terms represent the product of Poisson probabilities to observe n_i events in bins i and is given by

$$\text{Poisson}(\text{data}|\mu \cdot s + b) = \prod_i \frac{(\mu s_i + b_i)^{n_i}}{n_i!} e^{-\mu s_i - b_i}, \tag{5.13}$$

where s_i and b_i are the respective signal and background yields per bin.

We can then compare the compatibility of the data to the background-only and signal+background hypotheses by constructing a test statistic $\tilde{q}_\mu$ based on the profile likelihood ratio in Eq. 5.11:

$$\tilde{q}_\mu = -2 \ln \frac{\mathcal{L}(\text{data}|\mu, \hat{\theta}_\mu)}{\mathcal{L}(\text{data}|\hat{\mu}, \hat{\theta})}, \tag{5.14}$$

where $\hat{\mu}$ and $\hat{\theta}$ are the parameter values corresponding to the global maximum of the likelihood, and $\hat{\theta} + \mu$ refers to the conditional maximum likelihood estimators of θ given the data and signal strength parameter μ. Since the global maximum of the likelihood corresponds to the global minimum of $\tilde{q}_\mu$, we instead perform a fit over the nuisance parameters θ in order to minimize $\tilde{q}_\mu$ and determine the best fit value of μ. Note that μ is allowed to vary based on the fit, and the signal strength estimator $\hat{\mu}$ is constrained by $0 \leq \hat{\mu} \leq \mu$ in order to guarantee a one-sided confidence interval. This constraint is imposed so that upward fluctuations of data where $\hat{\mu} > \mu$ are not considered as evidence against the signal hypothesis.

To account for statistical and systematic uncertainties, we can construct a PDF $\rho(\theta|\tilde{\theta})$ for each nuisance parameter based on the type of uncertainty it is associated with. In this analysis, nuisance parameters associated with normalization uncertainties are assigned a log-normal PDF given by

$$\rho(\theta|\tilde{\theta}) = \frac{1}{\sqrt{2\pi}\theta\ln(\kappa)}\exp\left(-\frac{(\ln\theta - \ln\hat{\theta})^2}{2(\ln\kappa)^2}\right), \tag{5.15}$$

where κ characterizes the width of the distribution. Nuisance parameters associated with shape uncertainties are instead assigned a Gaussian PDF that can be modified through a "morphing" technique [216]. This technique is used to smoothly interpolate between different systematic templates by considering fractional event yields per bin, where interpolation can be performed either directly on the fractional yield or on its logarithm.

To determine the distribution of $\tilde{q}_\mu$, one normally requires the PDFs $f(\tilde{q}_\mu|\mu, \hat{\theta}_\mu^{\text{obs}})$ and $f(\tilde{q}_\mu|\mu, \hat{\theta}_0^{\text{obs}})$ for both the signal+background and background only hypothesis ($\mu = 0$) for a given signal strength μ. However, for large datasets, one can use Wilks' theorem to show that the distribution of $\tilde{q}_\mu$ asymptotically approximates a chi-squared distribution [217]. We use this asymptotic approximation to then compute two p-values p_μ and p_b or the signal+background and background-only hypotheses, respectively.

These $p-$values are given by

$$p_\mu = P(\tilde{q}_\mu \geq \tilde{q}_\mu^{\text{obs}}|\text{signal+background}) = \int_{\tilde{q}_\mu^{\text{obs}}}^{\infty} f(\tilde{q}_\mu|\mu, \hat{\theta}_\mu^{\text{obs}})d\tilde{q}_\mu \tag{5.16}$$

and

$$1 - p_b = P(\tilde{q}_\mu \geq \tilde{q}_\mu^{\text{obs}}|\text{background-only}) = \int_{\tilde{q}_0^{\text{obs}}}^{\infty} f(\tilde{q}_\mu|0, \hat{\theta}_0^{\text{obs}})d\tilde{q}_\mu \tag{5.17}$$

and quantify how well the data agrees with the corresponding hypothesis, with lower $p-$values indicating worse agreement. The $p-$value is related to the significance Z by the relation

$$Z = \Phi^{-1}(1-p), \tag{5.18}$$

where Φ^{-1} is the inverse of the cumulative distribution of the single sided standard Gaussian. A minimum significance of $Z = 5\sigma$ is commonly used at the LHC as a requirement to claim discovery of a signal.

If no discovery can be claimed, we can instead use the $p-$values to construct the variable $CL_s(\mu)$ [218, 219] defined as

$$CL_s(\mu) = \frac{p_\mu}{1 - p_b}. \tag{5.19}$$

We then use the CLs criterion to determine whether the signal+background hypothesis can be excluded at a certain confidence level. In general, for $CL_s \leq \alpha$ and $\mu = 1$, the criterion states that we can exclude the signal+background hypothesis with $(1 - \alpha)$ CLs confidence level. Thus, we can determine the 95% confidence level upper limit on the signal strength μ by adjusting μ until we reach $CL_s = 0.05$. The CLs criterion is defined such that it gives more conservative limits than the actual confidence level would imply. In particular, the CLs criterion avoids cases where signal is excluded due to large fluctuations in the background.

To characterize the sensitivity of the experiment, one can also compute the expected 95% confidence level upper limit on the signal strength by using what is known as the "Asimov data set". The Asimov data set is defined such that when one uses it to evaluate the estimators for all parameters, one obtains the true parameter values. This is done by setting the Asimov data parameters equal to their expectation values. The expected limit is then computed by using the corresponding Asimov profile likelihood ratio to calculate the 95% confidence level upper limit on the signal strength according to the CLs criterion. The expected limits represent the limits that would be set on the median value of the test statistic if the data were consistent with the background-only hypothesis, and therefore provide a baseline representation of the sensitivity of the experiment to the signal being considered.

In addition to the normalization and shape systematic uncertainties described in Section 5.6, unconstrained multiplicative nuisance parameters are assigned separately to each background for each bin of the p_T^{miss} distribution in the AH and SL channels to improve estimation of the main backgrounds. These multiplicative parameters scale the normalization of the associated background process as a function of p_T^{miss} simultaneously in the SRs and CRs for a given channel. For example, there is a single multiplicative parameter per p_T^{miss} bin associated with $t\bar{t}$ background in the SL channel that links the yield of $t\bar{t}$ in the $t\bar{t}$ enhanced 2l CR, the W+jets enhanced 1l CR, and the SL SRs. Similarly, unconstrained multiplicative nuisance parameters link the rates of the DY process in each NN bin between the DY CR and the DL 1b SF SR, while an overall normalization parameter links the total rate of $\mathbf{t\bar{t}}$Z between the $\mathbf{t\bar{t}}$Z CR and the DL SRs. Potential contributions from signal is included in all CRs and SRs, and is scaled by the ratio between the measured and theoretical cross sections for the signal.

5.8 Results

For the DM search, the results are interpreted using the signal model described in Section 5.1 for both scalar and pseudoscalar mediators with masses ranging from 50–500 GeV, with $m_\chi = 1$ GeV and $g_q = g_\chi = 1$. For the signal extraction, the signal strength parameter μ is defined as the ratio between the measured and the LO theoretical cross sections for the sum of the $t/\bar{t}$+DM and $t\bar{t}$+DM production modes. Upper limits at 95% confidence level (CL) are computed following the approach outlined in Section 5.7, and the results are shown in Fig. 5.8 in terms of model-independent 95% CL limits on the production cross section for new physics processes for the DM scalar and pseudoscalar models. Depending on the mass and type of the mediator considered, DM production cross section values ranging from 0.02–1 pb are probed.

The leading contribution to the signal sensitivity at low mediator masses (i.e. below 200 (300) GeV for the scalar (pseudoscalar) model) stems from the $t\bar{t}$+DM process because of their larger cross sections with respect to the $t/\bar{t}$+DM process. However, at higher mediator masses, the relative contribution of the $t/\bar{t}$+DM process to the signal sensitivity increases since the cross section for the $t/\bar{t}$+DM process drops less rapidly as a function

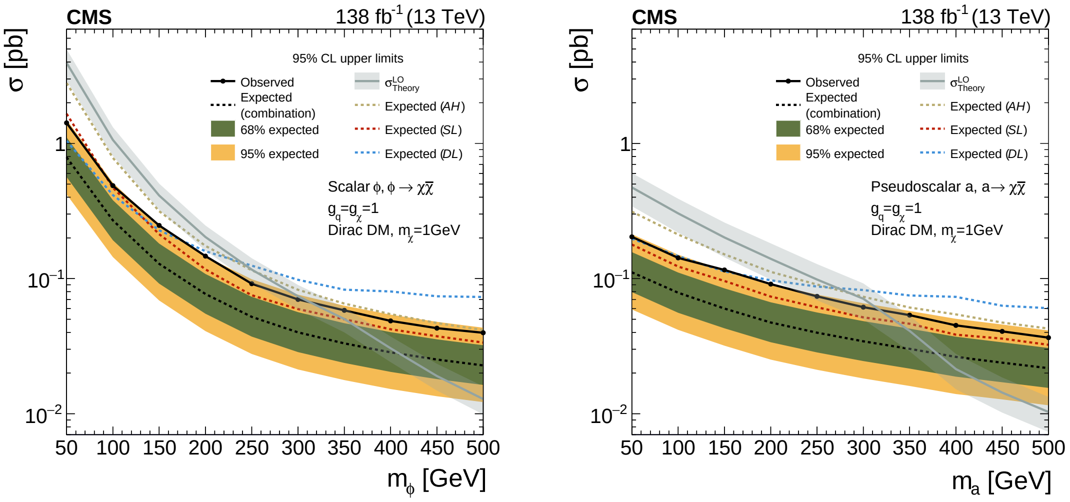

Figure 5.8: The model-independent 95% CL limits on production cross section for new physics processes for the DM scalar (left) and pseudoscalar (right) models. The black dashed line shows the expected limit with the 68 and 95% CL uncertainty bands shown in green and yellow, respectively, while the observed limit is shown by the solid black line. The gray line shows the theoretical LO cross section values for the DM model, with their associated uncertainties shown by the band in gray.

of the mediator mass compared to the $t\bar{t}$+DM process. Overall, from Fig. 5.8, we expect to exclude mediator masses below 410 (380) GeV for the benchmark cross sections of the scalar (pseudoscalar) hypothesis.

Since the signal kinematic properties are not very sensitive to the mass of the mediator, any signal-like excess in data will appear at all mediator mass points considered. However, the largest excess for all mediator hypotheses is within two standard deviations of the expected limits, so no significant excess above the SM background-only prediction was observed for all mediator hypotheses. Because of the observed excess, though, we only exclude mediator masses below 310 (320) GeV for the scalar (pseudoscalar mediator).

In addition to the DM model, these signatures can also be interpreted in terms of models with an ALP mediator A described in Section 5.1. Since the additional pseudoscalar mediator in Eq. 5.2 and the ALP in Eq. 5.3 exhibit the same coupling structure, then the existing upper limits on the production cross section for pseudoscalar interactions presented in Fig. 5.8 can be directly translated into upper limits on the ALP coupling to

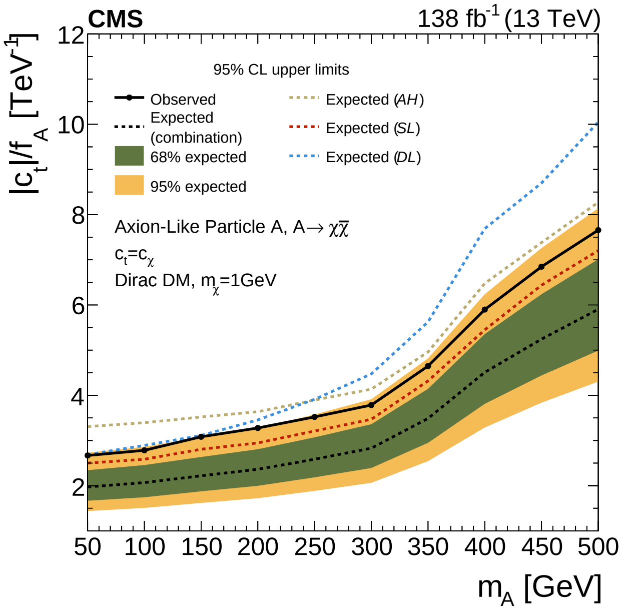

Figure 5.9: The 95% CL limits on the ratio of ALP-top coupling to the ALP scale, $|c_{\mathrm{t}}|/f_{\mathrm{A}}$, as a function of mediator mass for the ALP mediator model. The black dashed line shows the expected limit with the 68 and 95% CL uncertainty bands shown in green and yellow, respectively, whereas the observed limit is shown by the solid black line.

the top quark c_{t}, assuming the ALP does not have non-vanishing couplings to the gluon or electroweak gauge bosons [220]. However, for ALP masses above twice the top mass ($\sim$ 350 GeV), it becomes possible for the mediator to decay back into top quarks. Thus, varying c_{t} will change the branching ratio of the ALP to DM above this mass point, so we set the coupling to DM equal to the coupling to top quarks ($c_\chi = c_{\mathrm{t}}$). Upper limits on the ratio of the top coupling c_{t} to the ALP scale f_{A} are shown in Fig. 5.9 as a function of the ALP mass m_{A} assuming $c_{\mathrm{t}} = c_\chi$.

Chapter 6

Future Prospects

With Run 3 and the upcoming Phase-2 HL-LHC, the amount of data collected by the CMS experiment is expected to significantly increase. In addition, upgrades to both the detector and reconstruction algorithms can potentially lead to improvements in BSM searches that were previously carried out on Run 2 data. Thus, it is important to not only consider improvements that can be made to existing analyses, but also opportunities to explore new signatures. Section 6.1 will describe possible efforts to improve the DM analysis described in Chapter 5, while Section 6.2 will cover contributions to another search for BSM physics involving vector-like leptons.

6.1 Improvements to dark matter search

Though the search strategy for the AH and SL channels in the DM analysis employed a selection-based approach, the results of the DL channel demonstrate that significant improvements can be made by employing machine learning (ML) techniques. Machine learning is a tool that has already been frequently employed by CMS in both particle reconstruction and MC simulation [221, 222] in addition to analyses like the DM search. In the DL channel, frameworks like Keras [203] and Tensorflow [204] were used to train NNs to discriminate signal from SM background. This approach led to significant improvement in signal sensitivity compared to previous searches [154, 223]. This improvement motivates studies of whether ML techniques can also be applied to the other channels of the DM search as well to further improve signal sensitivity.

From the results presented in Section 5.8 and Fig. 5.8, the SL channel has the highest overall sensitivity to the signal due to a combination of signal cross section versus background rejection from selections applied. In addition, the DL channel seems to perform well at lower mediator masses where the p_T^{miss} distribution of the signal is softer, and therefore less sensitive to a search strategy focused on separating signal from background using a minimum p_T^{miss} selection. In comparison, the AH channel does perform relatively better at higher mediator masses where the signal p_T^{miss} spectrum is harder, but overall it remains the least sensitive channel. Thus, any improvement in signal discrimination in the AH channel could potentially translate to significant gains in overall search sensitivity for the analysis.

In particular, studies have been performed on developing and training a NN using Tensorflow to discriminate both $t/\bar{t}$+DM and $t\bar{t}$+DM signal from the dominant backgrounds in the AH channel using existing discriminating variables as input along with additional kinematic variables. The main backgrounds in the AH channel include $t\bar{t}$, W+jets, and $Z \to \nu\nu$ processes, which together comprise over 90–95% of the total SM background. For signal, only the scalar mediator model was considered, and for the $t/\bar{t}$+DM production mode, only the t-channel process was used for training.

Other ML techniques like boosted decision trees (BDTs) implemented using the TMVA package [224] in the ROOT framework [225] were also explored by training on MC samples corresponding to the 2016 data taking period at CMS. Parameters such as the number of trees, tree depth, type of signal sample, and node weights were adjusted in order to optimize performance, but the performance of the BDTs was quickly surpassed by early implementations of NNs. As a result, focus of the studies switched to the NN implementation in Tensorflow.

Different values for the parameters of the NN model were considered, which includes the number of features in the input layer, the number of hidden layers, the number of nodes in each layer, the number of epochs used for training, as well as the features used as input. The input variables included existing discriminating variables defined in Section 5.4.1 such as $\mathrm{p_T^{miss}}$, $\min\Delta\phi(\mathrm{j}_{1,2}, \mathrm{p_T^{miss}})$, and $\mathbf{p_T(j_1)/H_T}$. Additional kinematic variables were also computed and used as input to the NN to explore whether these variables could improve its performance. These variables include, but are not limited to, the leading jet $\mathrm{p_T}$, the leading b-jet $\mathrm{p_T}$, the opening angle between the leading jet and the $\mathrm{p_T^{miss}}$ vector, and the opening angle between the leading b-jet and the $\mathrm{p_T^{miss}}$ vector.

Training was performed separately for the $\mathrm{t/\bar{t}}$+DM and $\mathrm{t\bar{t}}$+DM signals, with only the mediator mass hypothesis $m_\phi = 100$ GeV included. However, for testing and validation, all mediator mass hypothesis ranging from 50–500 GeV were included. Performance was found to be relatively similar across the full mediator mass range even when training on a single mass point, which is expected given the similar signal kinematics when the DM particles are produced on-shell as is the case when its mass m_χ is set to 1 GeV. The performance of the NN was evaluated by applying the SR event selections for the AH channel described in Section 5.4.2, with the discriminating variable selections removed, and comparing the expected limits obtained from using the NN output in the signal extraction fit compared to $\mathrm{p_T^{miss}}$.

The procedure for the signal extraction fit is described in Section 5.7 and was performed using the `COMBINE` [213] tool. Expected limits were computed and compared for both the case where the NN output was used directly in the fit, and for the case where a simple minimum selection on the NN output was applied to the $\mathrm{p_T^{miss}}$ distribution (optimized and applied to each SR individually as well as for the combination of all SRs). The minimum selection chosen for each SR was optimized based on the figure-of-merit (FOM) given by $\mathrm{FOM} = \frac{s}{\sqrt{s+b}}$, where s and b are the total signal and background yields after selection, respectively. Preliminary results show significant improvement in signal sensitivity compared to the default selection for both cases, with the strongest constraints being set in the case where the NN output was used directly in the fit like in the DL channel, shown in Fig. 6.1.

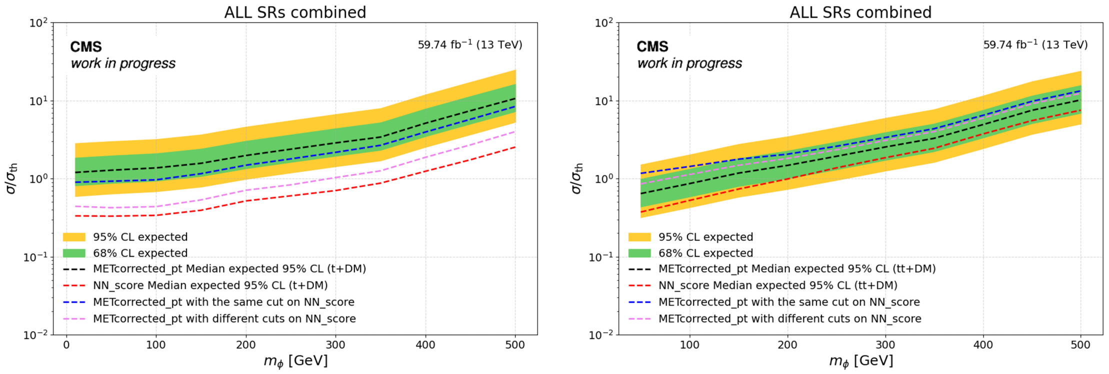

Figure 6.1: Comparison of the 95% CL limits on the ratio of the expected production cross section to LO theoretical cross section for DM scalar models for the $\mathrm{t}/\bar{\mathrm{t}}$+DM (left) and $\mathrm{t}\bar{\mathrm{t}}$+DM (right) signal processes, considering only the AH channel SRs. The black dashed line shows the expected limit using the default selection used in the DM analysis with the 68 and 95% CL uncertainty bands shown in green and yellow, respectively. The red dashed line shows the expected limit using the output of a NN instead of $p_{\mathrm{T}}^{\mathrm{miss}}$ in the signal extraction. The dashed blue and purple lines show the respective expected limits where a minimum selection on the NN output was applied to the $p_{\mathrm{T}}^{\mathrm{miss}}$ distribution for all SRs simultaneously and for each SR individually. Figure produced by Mitanshu Thakore.

However, several caveats apply to the results. For example, the fit did not include CRs, only statistical uncertainty was included, only the dominant backgrounds were considered, and several correction factors were not applied. Nonetheless, the results of this study demonstrate that there is significant potential for increasing the sensitivity of the DM search by employing the use of NNs in the AH channel. In combination with the additional data collected by the CMS detector during Run 3, higher signal sensitivity to DM can be reached for new physics analyses searching for DM at CMS.

6.2 Search for vector-like leptons

Though the nature of DM is an important open question that cannot be answered by the SM, it is not the only open question. One of the most important assumptions in the SM is lepton flavor universality (LFU), which describes the fact that electroweak couplings to the three lepton families are universal. This accidental flavor symmetry is only broken in the SM by the different masses of the charged leptons. However, recent measurements of

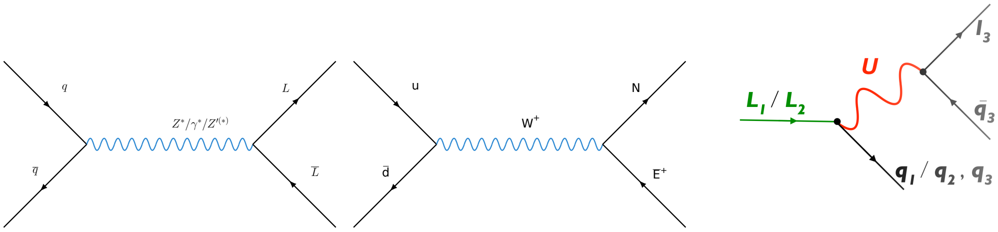

Figure 6.2: Example Feynman diagrams showing production of VLL pairs through an s-channel Z/γ boson (left) and an s-channel W boson (middle), as well as VLL decays into third generation fermions through an intermediate leptoquark U (right). Figure taken from [229].

B hadron decays [226–228] point to anomalies that suggest the possibility of lepton flavor violation (LFV).

To explain LFV, models have been proposed that extend the SM gauge groups to a larger $SU(4) \times SU(3)' \times SU(2)_L \times U(1)'$ group [229, 230]. This "4321" model provides a possible explanation for the LFV observed in the B anomalies while satisfying constraints set by other measurements in agreement with SM expectations and LFU [231–234]. In particular, the "4321" model predicts the existence of vector-like leptons (VLLs) with masses on the weak scale (500 GeV – 1 TeV) that can be produced at the LHC. VLLs can be produced at the LHC through electroweak couplings with s-channel W or Z bosons, or with an s-channel Z' boson. Like SM leptons, VLLs can be either charged (E) or neutral (N). However, in the "4321" model they form an $SU(2)_L$ doublet, with the masses of the pair being nearly degenerate. Thus, VLLs can be produced in pairs from either an s-channel Z boson ($Z \rightarrow E^+E^-$, $Z \rightarrow N\bar{N}$) or an s-channel W boson ($W \rightarrow E^+N$, $W \rightarrow E^-\bar{N}$). In addition, VLLs can also decay via a virtual leptoquark U that can further decay into leptons and quarks. Due to constraints from the B anomalies, leptoquarks are expected to decay almost entirely to third generation fermions. Figure 6.2 shows example Feynman diagrams of the possible production modes of VLL pairs as well as the decay of VLLs into third generation fermions.

In particular, VLL decays can produce top quarks which can further decay into leptons, as was the case for the DM search. Therefore, studying the leptonic decays of top quarks provides an avenue to not only look for DM, but also to look for other BSM physics like VLLs. The specific channel under consideration is the dilepton final state, where a search for VLLs is performed in final states with four b-jets and two leptons (e or μ) produced by the top quark decay. This search is motivated by a previous search at CMS which was performed in final states with four b-jets and up to two tau (τ) leptons which decayed hadronically [235]. Upper limits derived on the VLL production cross section for this analysis resulted in an observed excess of 2.8 standard deviations over the SM background-only hypothesis for a representative VLL mass point of 600 GeV, indicating the possible presence of signal. As a result, a search for VLLs is being performed in the dilepton final state in order to validate these results.

Like with the DM analysis, the dominant background in the dilepton channel is $\mathrm{t\bar{t}}$ background. In order to discriminate signal from background, a variable called S_T is used, defined as

$$S_T = \sum_i \mathrm{p_T}^i \tag{6.1}$$

where i is summed over all reconstructed jets, leptons, and $\mathrm{p_T^{miss}}$. This variable tends to peak at higher values for signal compared to $\mathrm{t\bar{t}}$, so it is used as the main discriminating variable for which the signal extraction fit is performed. However, due to the small cross section of the signal in the dilepton channel, the total statistical power of the S_T variable is quite limited, even after applying several selections to improve the signal to background ratio. Thus, a study was performed to investigate the use of ML techniques to further enhance sensitivity to the signal.

This study was based on the ML technique used in the previous VLL search, called ABCNet [236]. This model uses a graph neural network (GNN) that takes as input the final state objects, represented as nodes on a graph. The nodes are connected with edges that are characterized by distances of the objects in the $\eta - -\phi$ plane. Only the $k-$nearest neighbors for each node are considered, with $k = 10$ for the VLL analysis.

Each particle in the graph is represented by a set of features $\vec{x}_i$ that can be defined as

$$\vec{x}_i' = \sigma\left(\sum_j \alpha_{ij} y_{ij}\right), \tag{6.2}$$

where σ represents a non-linear transformation that is applied to the linear combination of attention coefficients α_{ij} and edges y_{ij} between nodes i and j. The GNN is constructed by combining graph pooling layers (GAPLayers) that consists of trainable coefficients assigned to each particle and neighbor given by

$$x_i' = h(x_i, \theta_i, F) \tag{6.3}$$

and

$$y_{ij}' = h(y_{ij}, \theta_{ij}, F), \tag{6.4}$$

where x_i are the values of the node features for node i, $y_{ij} = x_i - x_j$ is the value of the edge connecting nodes i and j, θ_i are the trainable coefficients, and F is the node size. The trainable parameters are introduced through a single-layer NN with the rectified linear unit (ReLU) activation function and are then combined with the node and edge values to form coefficients

$$c_{ij} = \mathrm{ReLu}(h(x_i', \theta_i', 1) + h(y_{ij}', \theta_{ij}', 1)), \tag{6.5}$$

where another fully connect layer operation with output size of 1 is applied to both encoded nodes and edges prior to the ReLu activation function being applied. These coefficients are then used to compute

$$\alpha_{ij} = \frac{\exp(c_{ij}}{\sum_k \exp(c_{ij}}, \tag{6.6}$$

where α_{ij} determine the relative importance of each connection to other particles in the graph. These updated node values as well as the set of graph features defined as

$$y_i' = \frac{1}{k}\sum_k Y_{ij} \tag{6.7}$$

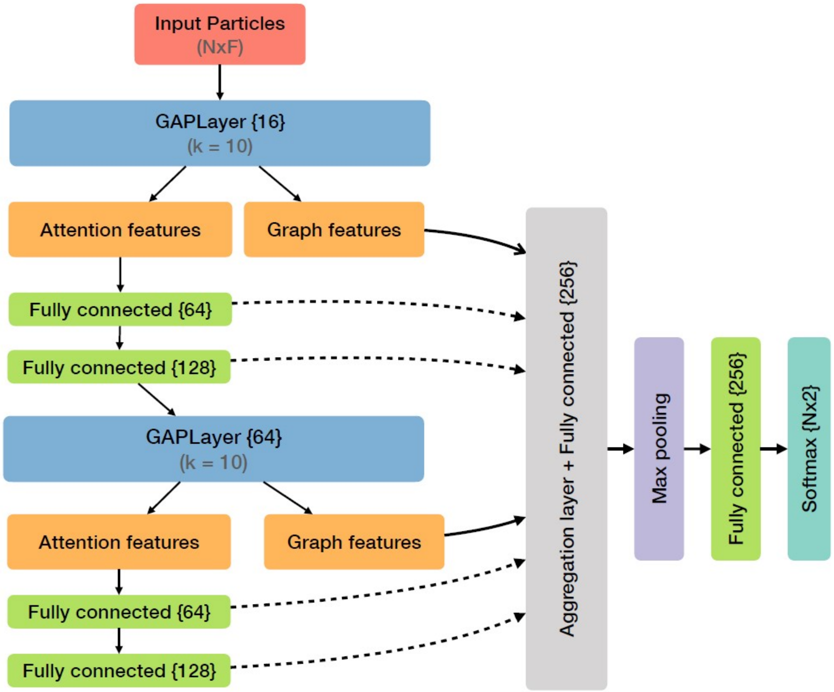

Figure 6.3: Schematic diagram of the ABCNet architecture used for VLL classification. Numbers inside the curly brackets represent the node size of fully connected layers, while k represents the number of neighbors associated to each particle. Figure taken from [237].

and can be passed as input to another GAPLayer or multilayer perceptron (MLP). Since only information of the nearest neighbors is used to associate nodes and vertices, all operations used in the GAPLayer are invariant to permutations of the input.

The graph features and node values are eventually concentrated and transformed to compute a single value output representing the likelihood that the event is signal versus background. The architecture of the ABCNet model used for the VLL analysis is shown in Fig. 6.3.

The same ABCNet model in the hadronic τ VLL search was adapted for use in the dilepton channel by replacing the input τ candidates with the two leptons instead. Preliminary studies were performed to evaluate the performance of using the output of this ABCNet model in the signal extraction fit compared to using the S_T distribution. Though preliminary limits corresponding to 2018 data on the expected VLL cross section were produced, more work is required to validate that the ABCNet model is performing correctly so that a valid comparison can be made to the default approach used in the main VLL analysis. In addition, these preliminary results did not include several components from the main analysis, including but not limited to the absence of systematic uncertainties, correction factors, and samples for 2016 and 2017 data taking periods. However, early results do suggest that the ABCNet employed in the hadronic τ VLL search can also be applied to the dileptonic channel in order to further increase signal sensitivity once more work is done to adapt the model.

Chapter 7

Summary

A search for dark matter (DM) produced in association with top quarks is presented. This search is motivated by astrophysical observations which provide evidence for the existence of DM through its gravitational interaction on visible matter. Though no explanation for DM is provided by the Standard Model (SM), various models involving physics beyond the Standard Model (BSM) have been proposed. Some of the models predict DM to have weak scale interactions with the SM, which would provide the opportunity to search for DM at high energy colliders like the LHC. Thus, a search for DM was performed using data corresponding to an integrated luminosity of 138 fb^{-1} collected by the CMS experiment between 2016–2018.

This search considers a simplified model where a scalar or pseudoscalar mediator particle couples to the top quark and subsequently decays into two DM particles. Various decay channels of the top quark are probed, depending on the number of leptons in the final state. These channels include the all hadronic (zero leptons), single lepton (one lepton), and dileptonic (two lepton) channels. The search strategy in the all hadronic and single lepton channels is to look for an excess in the missing transverse momentum distribution over SM background prediction in dedicated signal regions enhanced in signal. The dileptonic channel instead employs the use of a neural network that is trained to discriminate signal from background based on various kinematic variables. The SM backgrounds in each channel are either estimated from a data driven approach using dedicated control regions, or from Monte Carlo simulation.

A simultaneous fit to data is then performed in all three channels simultaneously to the final kinematic distribution considered, and the results are interpreted as constraints on the DM production cross section. Scalar and pseudoscalar mediator masses below 410 and 380 GeV, respectively, are expected to be excluded at 95% confidence level (CL) assuming a DM particle mass of 1 GeV and mediator couplings to fermions and DM particles equal to unity. Though a signal-like excess is observed in data, this excess is consistent with all mediator mass hypotheses, with the largest excess observed to be within two standard deviations of SM predictions. As a result, mediator masses are only excluded below 310 (32) GeV for the scalar (pseudoscalar) mediator. The upper limits for the pseudoscalar mediator hypothesis are also directly translated into limits on the coupling of an axion-like particle (ALP) to top quarks in a model where the ALP couples to the SM quarks as a mediator between a fermionic DM particle and the SM.

This search is the first performed by the CMS Collaboration to look for associated production of DM with both a single top quark and top quark pair across all possible lepton final states. With the ongoing Run 3 and the upcoming HL-LHC era at the LHC, there will be opportunities in the future to not only further improve the sensitivity of the DM search, but also to explore similar signatures involving top quarks to look for other BSM physics like vector-like leptons.

Bibliography

1. Glashow, S. L. Partial-symmetries of weak interactions. *Nuclear Physics* **22,** 579–588 (1961).
2. Weinberg, S. A Model of Leptons. *Phys. Rev. Lett.* **19,** 1264–1266 (21 1967).
3. Salam, A. & Ward, J. Electromagnetic and weak interactions. *Physics Letters* **13,** 168–171 (1964).
4. 't Hooft, G. & Veltman, M. Regularization and renormalization of gauge fields. *Nuclear Physics B* **44,** 189–213 (1972).
5. Einstein, A. The Foundation of the General Theory of Relativity. *Annalen der Physik* **49,** 769–822 (1916).
6. Noether, E. Invariante Variationsprobleme. ger. *Nachrichten von der Gesellschaft der Wissenschaften zu Göttingen, Mathematisch-Physikalische Klasse* **1918,** 235–257 (1918).
7. Einstein, A. On the electrodynamics of moving bodies. *Annalen der Physik* **17,** 891–921 (1905).
8. Pauli, W. Über den Zusammenhang des Abschlusses der Elektronengruppen im Atom mit der Komplexstruktur der Spektren. *Zeitschrift für Physik* **31,** 765–783 (1925).
9. Fukuda, Y. *et al.* Evidence for Oscillation of Atmospheric Neutrinos. *Phys. Rev. Lett.* **81,** 1562–1567 (8 1998).
10. Ahmad, Q. R. *et al.* Direct Evidence for Neutrino Flavor Transformation from Neutral-Current Interactions in the Sudbury Neutrino Observatory. *Phys. Rev. Lett.* **89,** 011301 (1 2002).
11. Higgs, P. W. Broken Symmetries and the Masses of Gauge Bosons. *Phys. Rev. Lett.* **13,** 508–509 (16 1964).
12. Englert, F. & Brout, R. Broken Symmetry and the Mass of Gauge Vector Mesons. *Phys. Rev. Lett.* **13,** 321–323 (9 1964).
13. Kibble, T. W. B. Symmetry breaking in nonAbelian gauge theories. *Phys. Rev.* **155** (ed Taylor, J. C.) 1554–1561 (1967).
14. Yang, C. N. & Mills, R. L. Conservation of Isotopic Spin and Isotopic Gauge Invariance. *Phys. Rev.* **96,** 191–195 (1 1954).
15. Ellis, J. *Higgs Physics* in *2013 European School of High-Energy Physics* (2015), 117–168. arXiv: `1312.5672 [hep-ph]`.

16. Santamaria, A. Masses, mixings, Yukawa couplings and their symmetries. *Phys. Lett. B* **305,** 90–97 (1993).

17. Workman, R. L., Burkert, V. D., Crede, V. & Klempt, E. Review of Particle Physics. *Progress of Theoretical and Experimental Physics* **2022,** 083C01 (Aug. 2022).

18. Chatrchyan, S. *et al.* Observation of a new boson at a mass of 125 GeV with the CMS experiment at the LHC. *Physics Letters B* **716,** 30–61 (2012).

19. Aad, G. *et al.* Observation of a new particle in the search for the Standard Model Higgs boson with the ATLAS detector at the LHC. *Physics Letters B* **716,** 1–29 (2012).

20. Chatrchyan, S. *et al.* Observation of a New Boson with Mass Near 125 GeV in pp Collisions at $\sqrt{s} = 7$ and 8 TeV. *JHEP* **06,** 081. arXiv: `1303.4571 [hep-ex]` (2013).

21. Altarelli, G. *The Standard electroweak theory and beyond* in *Zuoz Summer School on Phenomenology of Gauge Interactions* (Aug. 2000), 1–59. arXiv: `hep-ph/0011078`.

22. Tumasyan, A. *et al.* A portrait of the Higgs boson by the CMS experiment ten years after the discovery. *Nature* **607.** [Erratum: Nature 623, (2023)], 60–68. arXiv: `2207.00043 [hep-ex]` (2022).

23. Aad, G. *et al.* A detailed map of Higgs boson interactions by the ATLAS experiment ten years after the discovery. *Nature* **607.** [Erratum: Nature 612, E24 (2022)], 52–59. arXiv: `2207.00092 [hep-ex]` (2022).

24. Bilenky, S. M. Neutrino masses, mixing and oscillations. *Phys. Usp.* **46,** 1137–1152 (2003).

25. Abazajian, K. N. *et al. Light Sterile Neutrinos: A White Paper* 2012. arXiv: `1204.5379 [hep-ph]`. `https://arxiv.org/abs/1204.5379`.

26. Kisslinger, L. S. Review of neutrino oscillations with sterile and active neutrinos. *International Journal of Modern Physics A* **31,** 1630037. eprint: `https://doi.org/10.1142/S0217751X16300374` (2016).

27. Donoghue, J. F. *The effective field theory treatment of quantum gravity* in *AIP Conference Proceedings* (AIP, 2012). `http://dx.doi.org/10.1063/1.4756964`.

28. Witten, E. String theory dynamics in various dimensions. *Nuclear Physics B* **443,** 85–126 (1995).

29. Ranyard, A. Structure of the Milky Way. *Knowledge* **17,** 253 (1894).

30. Kelvin, L. (T. *Baltimore lectures on molecular dynamics and the wave theory of light* (C.J. Clay and Sons, Cambridge University Press, London, 1904).

31. Poincaré, H. & Vergne, H. *Leçons sur les hypothèses cosmogoniques: professées à la Sorbonne* (Gauthier-Villars, Paris, 1911).

32. Kapteyn, J. C. First Attempt at a Theory of the Arrangement and Motion of the Sidereal System. *Astrophysical Journal* **55,** 302–327 (1922).

33. Oort, J. H. The force exerted by the stellar system in the direction perpendicular to the galactic plane and some related problems. *Bulletin of the Astronomical Institutes of the Netherlands* **6,** 249 (1932).

34. Zwicky, F. Die Rotverschiebung von extragalaktischen Nebeln. *Helv. Phys. Acta* **6,** 110–127 (1933).
35. Rubin, V. C. & Ford, W. K. J. Rotation of the Andromeda Nebula from a Spectroscopic Survey of Emission Regions. *The Astrophysical Journal* **159,** 379 (1970).
36. NASA/IPAC Extragalactic Database (NED). *NASA/IPAC Extragalactic Database (NED)* `https://ned.ipac.caltech.edu`. Accessed: 2024-09-19. 2024.
37. Adelman-McCarthy, J. K. *et al.* The Fourth Data Release of the Sloan Digital Sky Survey. *The Astrophysical Journal Supplement Series* **162,** 38–48 (2006).
38. Clowe, D. *et al.* A direct empirical proof of the existence of dark matter. *The Astrophysical Journal Letters* **648,** L109–L113 (2006).
39. Milgrom, M. A modification of the Newtonian dynamics as a possible alternative to the hidden mass hypothesis. *The Astrophysical Journal* **270,** 365–370 (1983).
40. Chandra X-ray Observatory. *Gravitational Lensing of the Bullet Cluster (1E 0657-56)* Accessed: 2024-09-19. 2006. `https://chandra.harvard.edu/photo/2006/1e0657/more.html`.
41. Penzias, A. A. & Wilson, R. W. A measurement of excess antenna temperature at 4080 Mc/s. *The Astrophysical Journal* **142,** 419–421 (1965).
42. Seager, S., Sasselov, D. D. & Scott, D. How exactly did the universe become neutral? *The Astrophysical Journal Supplement Series* **128,** 407–430 (2000).
43. Planck Collaboration. *Planck Picture Gallery* Accessed: 2024-09-19. 2024. `https://www.cosmos.esa.int/web/planck/picture-gallery`.
44. Hu, W., Sugiyama, N. & Silk, J. The Physics of microwave background anisotropies. *Nature* **386,** 37–43 (1997).
45. Hu, W. & Dodelson, S. Cosmic microwave background anisotropies. *Annual Review of Astronomy and Astrophysics* **40,** 171–216 (2002).
46. Primack, J. Dark Matter and Structure Formation in the Universe. *arXiv preprint astro-ph/9707285.* `https://arxiv.org/abs/astro-ph/9707285` (1997).
47. Planck Collaboration. Planck 2018 results. VI. Cosmological parameters. *Astronomy & Astrophysics* **641,** A6. eprint: `arXiv:1807.06209`. `https://doi.org/10.1051/0004-6361/201833910` (2020).
48. Clowe, D. *et al.* A direct empirical proof of the existence of dark matter. *Astrophys. J. Lett.* **648,** L109–L113. arXiv: `astro-ph/0608407` (2006).
49. Springel, V., Frenk, C. S. & White, S. D. M. The large-scale structure of the Universe. *Nature* **440,** 1137. arXiv: `astro-ph/0604561` (2006).
50. Ibarra, A., Tran, D. & Weniger, C. Indirect Searches for Decaying Dark Matter. *International Journal of Modern Physics A* **28,** 1330040. eprint: `https://doi.org/10.1142/S0217751X13300408` (2013).
51. Dodelson, S., Gates, E. I. & Turner, M. S. Cold dark matter models. *Science* **274,** 69–75. arXiv: `astro-ph/9603081` (1996).

52. Lemson, G. & Consortium, T. V. Halo and Galaxy Formation Histories from the Millennium Simulation: Public release of a VO-oriented and SQL-queryable database for studying the evolution of galaxies in the LambdaCDM cosmogony. *arXiv preprint astro-ph/0608019.* `https://arxiv.org/abs/astro-ph/0608019` (2006).

53. Ellis, J. R., Hagelin, J. S., Nanopoulos, D. V., Olive, K. A. & Srednicki, M. Supersymmetric Relics from the Big Bang. *Nucl. Phys. B* **238** (ed Srednicki, M. A.) 453–476 (1984).

54. Dodelson, S. & Widrow, L. M. Sterile-neutrinos as dark matter. *Phys. Rev. Lett.* **72,** 17–20. arXiv: `hep-ph/9303287` (1994).

55. Peccei, R. D. & Quinn, H. R. CP Conservation in the Presence of Instantons. *Phys. Rev. Lett.* **38,** 1440–1443 (1977).

56. Preskill, J., Wise, M. B. & Wilczek, F. Cosmology of the Invisible Axion. *Phys. Lett. B* **120** (ed Srednicki, M. A.) 127–132 (1983).

57. Abbott, L. F. & Sikivie, P. A Cosmological Bound on the Invisible Axion. *Phys. Lett. B* **120** (ed Srednicki, M. A.) 133–136 (1983).

58. Holdom, B. Two U(1)'s and Epsilon Charge Shifts. *Phys. Lett. B* **166,** 196–198 (1986).

59. Arkani-Hamed, N., Finkbeiner, D. P., Slatyer, T. R. & Weiner, N. A Theory of Dark Matter. *Phys. Rev. D* **79,** 015014. arXiv: `0810.0713 [hep-ph]` (2009).

60. Jungman, G., Kamionkowski, M. & Griest, K. Supersymmetric dark matter. *Phys. Rept.* **267,** 195–373. arXiv: `hep-ph/9506380` (1996).

61. Bertone, G., Hooper, D. & Silk, J. Particle dark matter: Evidence, candidates and constraints. *Phys. Rept.* **405,** 279–390. arXiv: `hep-ph/0404175` (2005).

62. Feng, J. L. Dark Matter Candidates from Particle Physics and Methods of Detection. *Ann. Rev. Astron. Astrophys.* **48,** 495–545. arXiv: `1003.0904 [astro-ph.CO]` (2010).

63. Arcadi, G. *et al.* The waning of the WIMP? A review of models, searches, and constraints. *Eur. Phys. J. C* **78,** 203. arXiv: `1703.07364 [hep-ph]` (2018).

64. Aprile, E. *et al.* Dark Matter Search Results from a One Ton-Year Exposure of XENON1T. *Phys. Rev. Lett.* **121,** 111302. arXiv: `1805.12562 [astro-ph.CO]` (2018).

65. Aalbers, J. *et al.* First Dark Matter Search Results from the LUX-ZEPLIN (LZ) Experiment. *Phys. Rev. Lett.* **131,** 041002. arXiv: `2207.03764 [hep-ex]` (2023).

66. Wang, Q. *et al.* Results of dark matter search using the full PandaX-II exposure. *Chin. Phys. C* **44,** 125001. arXiv: `2007.15469 [astro-ph.CO]` (2020).

67. Circiello, A. *et al.* Constraining Dark Matter Annihilation with Fermi-LAT Observations of Ultra-Faint Compact Stellar Systems. arXiv: `2404.01181 [astro-ph.HE]` (Apr. 2024).

68. Kopp, J. Constraints on dark matter annihilation from AMS-02 results. *Phys. Rev. D* **88,** 076013. arXiv: `1304.1184 [hep-ph]` (2013).

69. Boveia, A. *et al.* Snowmass 2021 Cross Frontier Report: Dark Matter Complementarity (Extended Version). arXiv: `2210.01770 [hep-ph]` (Oct. 2022).

70. Duda, G., Kemper, A. & Gondolo, P. Model Independent Form Factors for Spin Independent Neutralino-Nucleon Scattering from Elastic Electron Scattering Data. *JCAP* **04,** 012. arXiv: `hep-ph/0608035` (2007).

71. Bednyakov, V. A. & Simkovic, F. Nuclear spin structure in dark matter search: The Finite momentum transfer limit. *Phys. Part. Nucl.* **37,** S106–S128. arXiv: `hep-ph/0608097` (2006).

72. Schnee, R. W. *Introduction to dark matter experiments* in *Theoretical Advanced Study Institute in Elementary Particle Physics: Physics of the Large and the Small* (2011), 775–829. arXiv: `1101.5205 [astro-ph.CO]`.

73. Meng, Y. *et al.* Dark Matter Search Results from the PandaX-4T Commissioning Run. *Phys. Rev. Lett.* **127,** 261802. arXiv: `2107.13438 [hep-ex]` (2021).

74. Akerib, D. S. *et al.* Results from a search for dark matter in the complete LUX exposure. *Phys. Rev. Lett.* **118,** 021303. arXiv: `1608.07648 [astro-ph.CO]` (2017).

75. Ajaj, R. *et al.* Search for dark matter with a 231-day exposure of liquid argon using DEAP-3600 at SNOLAB. *Phys. Rev. D* **100,** 022004. arXiv: `1902.04048 [astro-ph.CO]` (2019).

76. Alves, A., Berlin, A., Profumo, S. & Queiroz, F. S. Dark Matter Complementarity and the Z' Portal. *Phys. Rev. D* **92,** 083004. arXiv: `1501.03490 [hep-ph]` (2015).

77. Amole, C. *et al.* Dark matter search results from the PICO-60 CF_3I bubble chamber. *Phys. Rev. D* **93,** 052014. arXiv: `1510.07754 [hep-ex]` (2016).

78. Amole, C. *et al.* Improved dark matter search results from PICO-2L Run 2. *Phys. Rev. D* **93,** 061101. arXiv: `1601.03729 [astro-ph.CO]` (2016).

79. Behnke, E. *et al.* Final Results of the PICASSO Dark Matter Search Experiment. *Astropart. Phys.* **90,** 85–92. arXiv: `1611.01499 [hep-ex]` (2017).

80. Felizardo, M. *et al.* The SIMPLE Phase II Dark Matter Search. *Phys. Rev. D* **89,** 072013. arXiv: `1404.4309 [hep-ph]` (2014).

81. Aartsen, M. G. *et al.* Search for annihilating dark matter in the Sun with 3 years of IceCube data. *Eur. Phys. J. C* **77.** [Erratum: Eur.Phys.J.C 79, 214 (2019)], 146. arXiv: `1612.05949 [astro-ph.HE]` (2017).

82. Tanaka, T. *et al.* An Indirect Search for WIMPs in the Sun using 3109.6 days of upward-going muons in Super-Kamiokande. *Astrophys. J.* **742,** 78. arXiv: `1108.3384 [astro-ph.HE]` (2011).

83. Frankiewicz, K. *Searching for Dark Matter Annihilation into Neutrinos with Super-Kamiokande* in *Meeting of the APS Division of Particles and Fields* (Oct. 2015). arXiv: `1510.07999 [hep-ex]`.

84. *Search for dark matter in final states with an energetic jet, or a hadronically decaying W or Z boson using* 12.9 fb^{-1} *of data at* $\sqrt{s} = 13$ TeV tech. rep. (CERN, Geneva, 2016). `https://cds.cern.ch/record/2205746`.

85. Giroux, G. *Dark Matter Search Results from the PICO-60 C3F8 Bubble Chamber* in *52nd Rencontres de Moriond on EW Interactions and Unified Theories* (2017), 315–322.

86. Abdalla, H. *et al.* Search for Dark Matter Annihilation Signals in the H.E.S.S. Inner Galaxy Survey. *Phys. Rev. Lett.* **129,** 111101. arXiv: `2207.10471 [astro-ph.HE]` (2022).

87. Abe, S. *et al.* Dark matter line searches with the Cherenkov Telescope Array. *JCAP* **07,** 047. arXiv: `2403.04857 [hep-ph]` (2024).

88. Chau, N. T. *et al.* Indirect dark matter search in the Galactic Centre with IceCube. *PoS* **ICRC2023,** 1394. arXiv: `2308.06729 [astro-ph.HE]` (2023).

89. Abe, K. *et al.* Indirect search for dark matter from the Galactic Center and halo with the Super-Kamiokande detector. *Phys. Rev. D* **102,** 072002. arXiv: `2005.05109 [hep-ex]` (2020).

90. Albert, A. *et al.* Search for dark matter towards the Galactic Centre with 11 years of ANTARES data. *Phys. Lett. B* **805,** 135439. arXiv: `1912.05296 [astro-ph.HE]` (2020).

91. Aartsen, M. G. *et al.* All-flavour Search for Neutrinos from Dark Matter Annihilations in the Milky Way with IceCube/DeepCore. *Eur. Phys. J. C* **76,** 531. arXiv: `1606.00209 [astro-ph.HE]` (2016).

92. Aartsen, M. G. *et al.* Search for Neutrinos from Dark Matter Self-Annihilations in the center of the Milky Way with 3 years of IceCube/DeepCore. *Eur. Phys. J. C* **77,** 627. arXiv: `1705.08103 [hep-ex]` (2017).

93. Abbasi, R. *et al.* Search for neutrino lines from dark matter annihilation and decay with IceCube. *Phys. Rev. D* **108,** 102004. arXiv: `2303.13663 [astro-ph.HE]` (2023).

94. Ageron, M. & Collaboration, K. KM3NeT: Neutrino astronomy at the cubic-kilometer scale. *PoS ICRC2021* **537.** Presented at the 37th International Cosmic Ray Conference (ICRC 2021). `https://pos.sissa.it/395/537/pdf` (2021).

95. Steigman, G., Dasgupta, B. & Beacom, J. F. Precise Relic WIMP Abundance and its Impact on Searches for Dark Matter Annihilation. *Phys. Rev. D* **86,** 023506. arXiv: `1204.3622 [hep-ph]` (2012).

96. Goodman, J. *et al.* Constraints on Light Majorana dark Matter from Colliders. *Phys. Lett. B* **695,** 185–188. arXiv: `1005.1286 [hep-ph]` (2011).

97. Bai, Y., Fox, P. J. & Harnik, R. The Tevatron at the Frontier of Dark Matter Direct Detection. *JHEP* **12,** 048. arXiv: `1005.3797 [hep-ph]` (2010).

98. Goodman, J. *et al.* Constraints on Dark Matter from Colliders. *Phys. Rev. D* **82,** 116010. arXiv: `1008.1783 [hep-ph]` (2010).

99. Rajaraman, A., Shepherd, W., Tait, T. M. P. & Wijangco, A. M. LHC Bounds on Interactions of Dark Matter. *Phys. Rev. D* **84,** 095013. arXiv: `1108.1196 [hep-ph]` (2011).

100. Busoni, G., De Simone, A., Morgante, E. & Riotto, A. On the Validity of the Effective Field Theory for Dark Matter Searches at the LHC. *Phys. Lett. B* **728,** 412–421. arXiv: `1307.2253 [hep-ph]` (2014).
101. Alves, A., Profumo, S., Queiroz, F. S. & Shepherd, W. Effective field theory approach to the Galactic Center gamma-ray excess. *Phys. Rev. D* **90,** 115003. arXiv: `1403.5027 [hep-ph]` (2014).
102. Busoni, G., De Simone, A., Jacques, T., Morgante, E. & Riotto, A. On the Validity of the Effective Field Theory for Dark Matter Searches at the LHC Part III: Analysis for the t-channel. *JCAP* **09,** 022. arXiv: `1405.3101 [hep-ph]` (2014).
103. De Simone, A. & Jacques, T. Simplified models vs. effective field theory approaches in dark matter searches. *Eur. Phys. J. C* **76,** 367. arXiv: `1603.08002 [hep-ph]` (2016).
104. Aad, G. *et al.* Constraints on dark matter models involving an s-channel mediator with the ATLAS detector in pp collisions at $\sqrt{s} = 13$ TeV. arXiv: `2404.15930 [hep-ex]` (Apr. 2024).
105. Tumasyan, A. *et al.* Search for new particles in events with energetic jets and large missing transverse momentum in proton-proton collisions at $\sqrt{s} = 13$ TeV. *JHEP* **11,** 153 (2021).
106. Tumasyan, A. *et al.* Combined searches for the production of supersymmetric top quark partners in proton–proton collisions at $\sqrt{s} = 13\,$TeV. *Eur. Phys. J. C* **81,** 970 (2021).
107. Sirunyan, A. M. *et al.* Search for dark matter produced in association with a leptonically decaying Z boson in proton-proton collisions at $\sqrt{s} = 13$ TeV. *Eur. Phys. J. C* **81.** [Erratum: Eur.Phys.J.C 81, 333 (2021)], 13 (2021).
108. LHC Machine. *JINST* **3** (eds Evans, L. & Bryant, P.) S08001 (2008).
109. Chatrchyan, S. *et al.* The CMS Experiment at the CERN LHC. *JINST* **3,** S08004 (2008).
110. Bayatian, G. L. *et al.* CMS Physics: Technical Design Report Volume 1: Detector Performance and Software (2006).
111. Aad, G. *et al.* The ATLAS experiment at the CERN Large Hadron Collider: a description of the detector configuration for Run 3. *JINST* **19,** P05063 (2024).
112. Aamodt, K. *et al.* The ALICE experiment at the CERN LHC. *JINST* **3,** S08002 (2008).
113. Alves Jr., A. A. *et al.* The LHCb Detector at the LHC. *JINST* **3,** S08005 (2008).
114. Lopienska, E. The CERN accelerator complex, layout in 2022. Complexe des accélérateurs du CERN en janvier 2022. General Photo. `https://cds.cern.ch/record/2800984` (2022).
115. High-Luminosity LHC Collaboration. *High-Luminosity LHC Project* `https://hilumilhc.web.cern.ch/content/hl-lhc-project`. last update October 2024.
116. CMS Collaboration. *CMS Public Luminosity Results* `https://twiki.cern.ch/twiki/bin/view/CMSPublic/LumiPublicResults`. last update October 2024.

117. Hayrapetyan, A. *et al.* Development of the CMS detector for the CERN LHC Run 3. *JINST* **19,** P05064 (2024).

118. James, T. *A hardware track-trigger for CMS at the High Luminosity LHC* PhD thesis (Imperial Coll., London, 2018).

119. Chatrchyan, S. *et al.* Precise Mapping of the Magnetic Field in the CMS Barrel Yoke using Cosmic Rays. *JINST* **5,** T03021 (2010).

120. Sirunyan, A. M. *et al.* Calibration of the CMS hadron calorimeters using proton-proton collision data at $\sqrt{s} = 13$ TeV. *JINST* **15,** P05002 (2020).

121. Sirunyan, A. M. *et al.* Performance of the CMS muon detector and muon reconstruction with proton-proton collisions at $\sqrt{s} = 13$ TeV. *JINST* **13,** P06015 (2018).

122. Sirunyan, A. M. *et al.* Performance of the CMS Level-1 trigger in proton-proton collisions at $\sqrt{s} = 13$ TeV. *JINST* **15,** P10017 (2020).

123. Adam, W. *et al.* The CMS high level trigger. *Eur. Phys. J. C* **46,** 605–667 (2006).

124. Roland, C. Triggering on Hard Probes in Heavy-Ion Collisions with the CMS Experiment at the LHC. *Nucl. Phys. A* **830** (eds Stankus, P., Silvermyr, D., Sorensen, S. & Greene, V.) 523C–526C (2009).

125. CMS: The TriDAS project. Technical design report, Vol. 2: Data acquisition and high-level trigger (ed Sphicas, P.) (Dec. 2002).

126. LHC computing Grid. Technical design report (eds Bird, I. *et al.*) (June 2005).

127. Azzolini, V. *et al.* The Data Quality Monitoring software for the CMS experiment at the LHC: past, present and future. *EPJ Web Conf.* **214** (eds Forti, A., Betev, L., Litmaath, M., Smirnova, O. & Hristov, P.) 02003 (2019).

128. Hazen, E. *et al.* The AMC13XG: a new generation clock/timing/DAQ module for CMS MicroTCA. *JINST* **8,** C12036 (2013).

129. Bologna, S. *et al.* SWATCH: Common software for controlling and monitoring the upgraded CMS Level-1 trigger. *J. Phys. Conf. Ser.* **898** (eds Mount, R. & Tull, C.) 032040 (2017).

130. Magrans de Abril, I., Wulz, C. E. & Varela, J. Concept of the CMS trigger supervisor. *IEEE Trans. Nucl. Sci.* **53,** 474–483 (2006).

131. Sirunyan, A. M. *et al.* Particle-flow reconstruction and global event description with the CMS detector. *JINST* **12,** P10003 (2017).

132. Adam, W., Mangano, B., Speer, T. & Todorov, T. Track reconstruction in the CMS tracker (Dec. 2005).

133. Chatrchyan, S. *et al.* Description and performance of track and primary-vertex reconstruction with the CMS tracker. *JINST* **9,** P10009 (2014).

134. Rose, K. Deterministic annealing for clustering, compression, classification, regression, and related optimization problems. *IEEE Proc.* **86,** 2210–2239 (1998).

135. Fruhwirth, R., Waltenberger, W. & Vanlaer, P. Adaptive vertex fitting. *J. Phys. G* **34,** N343 (2007).

136. Hayrapetyan, A. *et al.* Performance of CMS muon reconstruction from proton-proton to heavy ion collisions. *JINST* **19,** P09012 (2024).

137. Adam, W., Frühwirth, R., Strandlie, A. & Todor, T. Reconstruction of Electrons with the Gaussian-Sum Filter in the CMS Tracker at the LHC (Jan. 2005).

138. Sirunyan, A. M. *et al.* Electron and photon reconstruction and identification with the CMS experiment at the CERN LHC. *JINST* **16,** P05014 (2021).

139. Cacciari, M., Salam, G. P. & Soyez, G. The anti-k_t jet clustering algorithm. *JHEP* **04,** 063 (2008).

140. Identification of b quark jets at the CMS Experiment in the LHC Run 2 (2016).

141. Sirunyan, A. M. *et al.* Identification of heavy-flavour jets with the CMS detector in pp collisions at 13 TeV. *JINST* **13,** P05011. arXiv: `1712.07158 [physics.ins-det]` (2018).

142. Guest, D. *et al.* Jet Flavor Classification in High-Energy Physics with Deep Neural Networks. *Phys. Rev. D* **94,** 112002. arXiv: `1607.08633 [hep-ex]` (2016).

143. Sirunyan, A. M. *et al.* Performance of missing transverse momentum reconstruction in proton-proton collisions at $\sqrt{s} = 13$ TeV using the CMS detector. *JINST* **14,** P07004 (2019).

144. Zabi, A., Berryhill, J. W., Perez, E. & Tapper, A. D. The Phase-2 Upgrade of the CMS Level-1 Trigger (2020).

145. Wiehe, M. The CMS high granularity calorimeter for the High Luminosity LHC. *Nucl. Instrum. Meth. A* **1041,** 167312 (2022).

146. Standalone barrel e/γ and calorimeter based jet and tau reconstruction in the Level-1 Phase-2 Calorimeter Trigger. `https://cds.cern.ch/record/2904693` (2024).

147. Search for dark matter produced in association with a single top quark or a top quark pair in proton-proton collisions at $\sqrt{s} = 13$ TeV (2024).

148. Bertone, G., Hooper, D. & Silk, J. Particle dark matter: Evidence, candidates and constraints. *Phys. Rept.* **405,** 279–390. arXiv: `hep-ph/0404175` (2005).

149. Khachatryan, V. *et al.* Search for dark matter, extra dimensions, and unparticles in monojet events in proton–proton collisions at $\sqrt{s} = 8$ TeV. *Eur. Phys. J. C* **75,** 235 (2015).

150. Khachatryan, V. *et al.* Search for new phenomena in monophoton final states in proton-proton collisions at $\sqrt{s} = 8$ TeV. *Phys. Lett. B* **755,** 102–124 (2016).

151. Khachatryan, V. *et al.* Search for physics beyond the standard model in final states with a lepton and missing transverse energy in proton-proton collisions at sqrt(s) = 8 TeV. *Phys. Rev. D* **91,** 092005 (2015).

152. Khachatryan, V. *et al.* Search for Monotop Signatures in Proton-Proton Collisions at $\sqrt{s} = 8$ TeV. *Phys. Rev. Lett.* **114,** 101801 (2015).

153. Khachatryan, V. *et al.* Search for the production of dark matter in association with top-quark pairs in the single-lepton final state in proton-proton collisions at sqrt(s) = 8 TeV. *JHEP* **06,** 121 (2015).

154. Search for the Production of Dark Matter in Association with Top Quark Pairs in the Di-lepton Final State in pp collisions at $\sqrt{s} = 8$ TeV (2014).

155. Search for dark matter direct production using razor variables in events with two or more jets in pp collisions at 8 TeV (2015).

156. Abercrombie, D. *et al.* Dark Matter benchmark models for early LHC Run-2 Searches: Report of the ATLAS/CMS Dark Matter Forum. *Phys. Dark Univ.* **27** (eds Boveia, A., Doglioni, C., Lowette, S., Malik, S. & Mrenna, S.) 100371 (2020).

157. Buckley, M. R., Feld, D. & Goncalves, D. Scalar Simplified Models for Dark Matter. *Phys. Rev. D* **91,** 015017. eprint: `1410.6497` (2015).

158. Chivukula, R. S. & Georgi, H. Composite Technicolor Standard Model. *Phys. Lett. B* **188,** 99–104 (1987).

159. Hall, L. J. & Randall, L. Weak scale effective supersymmetry. *Phys. Rev. Lett.* **65,** 2939–2942 (1990).

160. Buras, A. J., Gambino, P., Gorbahn, M., Jager, S. & Silvestrini, L. Universal unitarity triangle and physics beyond the standard model. *Phys. Lett. B* **500,** 161–167 (2001).

161. D'Ambrosio, G., Giudice, G. F., Isidori, G. & Strumia, A. Minimal flavor violation: An Effective field theory approach. *Nucl. Phys. B* **645,** 155–187 (2002).

162. Pinna, D., Zucchetta, A., Buckley, M. R. & Canelli, F. Single top quarks and dark matter. *Phys. Rev. D* **96,** 035031. arXiv: `1701.05195 [hep-ph]` (2017).

163. Sirunyan, A. M. *et al.* Search for dark matter produced in association with a single top quark or a top quark pair in proton-proton collisions at $\sqrt{s} = 13$ TeV. *JHEP* **03,** 141 (2019).

164. Dolan, M. J., Kahlhoefer, F., McCabe, C. & Schmidt-Hoberg, K. A taste of dark matter: Flavour constraints on pseudoscalar mediators. *JHEP* **03.** [Erratum: JHEP 07, 103 (2015)], 171 (2015).

165. Bharucha, A., Brümmer, F., Desai, N. & Mutzel, S. Axion-like particles as mediators for dark matter: beyond freeze-out. *JHEP* **02,** 141 (2023).

166. Allen, S. *et al.* Electroweak Axion Portal to Dark Matter. arXiv: `2405.02403 [hep-ph]` (May 2024).

167. Blasi, S. *et al.* Top-philic ALP phenomenology at the LHC: the elusive mass-window. *JHEP* **06,** 077 (2024).

168. Peccei, R. D. & Quinn, H. R. Constraints Imposed by CP Conservation in the Presence of Instantons. *Phys. Rev. D* **16,** 1791–1797 (1977).

169. Weinberg, S. A New Light Boson? *Phys. Rev. Lett.* **40,** 223–226 (1978).

170. Wilczek, F. Problem of Strong P and T Invariance in the Presence of Instantons. *Phys. Rev. Lett.* **40,** 279–282 (1978).

171. Khachatryan, V. *et al.* The CMS trigger system. *JINST* **12,** P01020 (2017).

172. Buckley, A. *et al.* General-purpose event generators for LHC physics. *Phys. Rept.* **504,** 145–233 (2011).

173. Nason, P. A New method for combining NLO QCD with shower Monte Carlo algorithms. *JHEP* **11,** 040 (2004).

174. Frixione, S., Nason, P. & Oleari, C. Matching NLO QCD computations with Parton Shower simulations: the POWHEG method. *JHEP* **11,** 070 (2007).

175. Alioli, S., Nason, P., Oleari, C. & Re, E. A general framework for implementing NLO calculations in shower Monte Carlo programs: the POWHEG BOX. *JHEP* **06,** 043 (2010).

176. Alioli, S., Nason, P., Oleari, C. & Re, E. NLO single-top production matched with shower in POWHEG: s- and t-channel contributions. *JHEP* **09.** [Erratum: JHEP 02, 011 (2010)], 111 (2009).

177. Re, E. Single-top Wt-channel production matched with parton showers using the POWHEG method. *Eur. Phys. J. C* **71,** 1547 (2011).

178. Frixione, S., Nason, P. & Ridolfi, G. A Positive-weight next-to-leading-order Monte Carlo for heavy flavour hadroproduction. *JHEP* **09,** 126 (2007).

179. Frederix, R. & Frixione, S. Merging meets matching in MC@NLO. *JHEP* **12,** 061. arXiv: `1209.6215 [hep-ph]` (2012).

180. Alwall, J. *et al.* The automated computation of tree-level and next-to-leading order differential cross sections, and their matching to parton shower simulations. *JHEP* **07,** 079. arXiv: `1405.0301 [hep-ph]` (2014).

181. Frederix, R. & Frixione, S. Merging meets matching in MC@NLO. *JHEP* **12,** 061 (2012).

182. Mangano, M. L., Moretti, M., Piccinini, F. & Treccani, M. Matching matrix elements and shower evolution for top-quark production in hadronic collisions. *JHEP* **01,** 013 (2007).

183. Denner, A., Dittmaier, S., Kasprzik, T. & Muck, A. Electroweak corrections to W + jet hadroproduction including leptonic W-boson decays. *JHEP* **08,** 075 (2009).

184. Denner, A., Dittmaier, S., Kasprzik, T. & Muck, A. Electroweak corrections to dilepton + jet production at hadron colliders. *JHEP* **06,** 069 (2011).

185. Denner, A., Dittmaier, S., Kasprzik, T. & Mück, A. Electroweak corrections to monojet production at the LHC. *Eur. Phys. J. C* **73,** 2297 (2013).

186. Kuhn, J. H., Kulesza, A., Pozzorini, S. & Schulze, M. Electroweak corrections to hadronic photon production at large transverse momenta. *JHEP* **03,** 059 (2006).

187. Kallweit, S., Lindert, J. M., Maierhöfer, P., Pozzorini, S. & Schönherr, M. NLO electroweak automation and precise predictions for W+multijet production at the LHC. *JHEP* **04,** 012 (2015).

188. Kallweit, S., Lindert, J. M., Maierhofer, P., Pozzorini, S. & Schönherr, M. NLO QCD+EW predictions for V + jets including off-shell vector-boson decays and multijet merging. *JHEP* **04,** 021 (2016).

189. Sjöstrand, T. *et al.* An introduction to PYTHIA 8.2. *Comput. Phys. Commun.* **191,** 159–177 (2015).

190. Gehrmann, T. *et al.* W^+W^- Production at Hadron Colliders in Next to Next to Leading Order QCD. *Phys. Rev. Lett.* **113,** 212001 (2014).

191. Campbell, J. M. & Ellis, R. K. An Update on vector boson pair production at hadron colliders. *Phys. Rev. D* **60,** 113006 (1999).

192. Boveia, A. *et al.* Recommendations on presenting LHC searches for missing transverse energy signals using simplified s-channel models of dark matter. *Phys. Dark Univ.* **27** (eds Buchmueller, O. *et al.*) 100365. arXiv: `1603.04156 [hep-ex]` (2020).

193. Ball, R. D. *et al.* Parton distributions for the LHC Run II. *JHEP* **04,** 040 (2015).

194. Ball, R. D. *et al.* Parton distributions from high-precision collider data. *Eur. Phys. J. C* **77,** 663 (2017).

195. Khachatryan, V. *et al.* Event generator tunes obtained from underlying event and multiparton scattering measurements. *Eur. Phys. J. C* **76,** 155 (2016).

196. Sirunyan, A. M. *et al.* Extraction and validation of a new set of CMS PYTHIA8 tunes from underlying-event measurements. *Eur. Phys. J. C* **80,** 4 (2020).

197. Agostinelli, S. *et al.* GEANT4–a simulation toolkit. *Nucl. Instrum. Meth. A* **506,** 250–303 (2003).

198. Bai, Y., Cheng, H.-C., Gallicchio, J. & Gu, J. Stop the Top Background of the Stop Search. *JHEP* **07,** 110 (2012).

199. Graesser, M. L. & Shelton, J. Hunting Mixed Top Squark Decays. *Phys. Rev. Lett.* **111,** 121802. eprint: `1212.4495` (2013).

200. Lester, C. G. & Summers, D. J. Measuring masses of semiinvisibly decaying particles pair produced at hadron colliders. *Phys. Lett. B* **463,** 99–103 (1999).

201. Khachatryan, V. *et al.* Searches for Supersymmetry using the M_{T2} Variable in Hadronic Events Produced in pp Collisions at 8 TeV. *JHEP* **05,** 078 (2015).

202. Betchart, B. A., Demina, R. & Harel, A. Analytic solutions for neutrino momenta in decay of top quarks. *Nucl. Instrum. Meth. A* **736,** 169–178 (2014).

203. Chollet, F. *Keras* `https://keras.io`. 2015.

204. Abadi, M. *et al.* *TensorFlow: Large-Scale Machine Learning on Heterogeneous Systems* `https://www.tensorflow.org/`. 2015.

205. Sirunyan, A. M. *et al.* Precision luminosity measurement in proton-proton collisions at $\sqrt{s} = 13$ TeV in 2015 and 2016 at CMS. *Eur. Phys. J. C* **81,** 800 (2021).

206. CMS luminosity measurement for the 2017 data-taking period at $\sqrt{s} = 13$ TeV (2018).

207. CMS luminosity measurement for the 2018 data-taking period at $\sqrt{s} = 13$ TeV (2019).

208. Butterworth, J. *et al.* PDF4LHC recommendations for LHC Run II. *J. Phys. G* **43,** 023001. arXiv: `1510.03865 [hep-ph]` (2016).

209. Sirunyan, A. M. *et al.* Measurement of the inelastic proton-proton cross section at $\sqrt{s} = 13$ TeV. *JHEP* **07,** 161 (2018).

210. Barlow, R. J. & Beeston, C. Fitting using finite Monte Carlo samples. *Comput. Phys. Commun.* **77,** 219–228 (1993).

211. Khachatryan, V. *et al.* Measurement of differential cross sections for top quark pair production using the lepton+jets final state in proton-proton collisions at 13 TeV. *Phys. Rev. D* **95,** 092001. arXiv: `1610.04191 [hep-ex]` (2017).

212. Procedure for the LHC Higgs boson search combination in Summer 2011 (Aug. 2011).

213. Hayrapetyan, A. *et al.* The CMS Statistical Analysis and Combination Tool: COMBINE. arXiv: `2404.06614 [physics.data-an]` (Apr. 2024).

214. Verkerke, W. & Kirkby, D. P. The RooFit toolkit for data modeling. *eConf* **C0303241** (eds Lyons, L. & Karagoz, M.) MOLT007. arXiv: `physics/0306116` (2003).

215. Moneta, L. *et al.* The RooStats Project. *PoS* **ACAT2010** (eds Speer, T. *et al.*) 057. arXiv: `1009.1003 [physics.data-an]` (2010).

216. Conway, J. S. *Incorporating Nuisance Parameters in Likelihoods for Multisource Spectra* in *PHYSTAT 2011* (2011), 115–120.

217. Cowan, G., Cranmer, K., Gross, E. & Vitells, O. Asymptotic formulae for likelihood-based tests of new physics. *Eur. Phys. J. C* **71.** [Erratum: Eur.Phys.J.C 73, 2501 (2013)], 1554. arXiv: `1007.1727 [physics.data-an]` (2011).

218. Junk, T. Confidence level computation for combining searches with small statistics. *Nucl. Instrum. Meth. A* **434,** 435–443. arXiv: `hep-ex/9902006` (1999).

219. Read, A. L. Presentation of search results: The CL_s technique. *J. Phys. G* **28** (eds Whalley, M. R. & Lyons, L.) 2693–2704 (2002).

220. Anuar, A. *et al.* ALP-ine quests at the LHC: hunting axion-like particles via peaks and dips in $t\bar{t}$ production. arXiv: `2404.19014 [hep-ph]` (Apr. 2024).

221. Pata, J. *et al.* Machine Learning for Particle Flow Reconstruction at CMS. *J. Phys. Conf. Ser.* **2438,** 012100 (2023).

222. Reweighting of simulated events using machine learning techniques in CMS (2024).

223. Sirunyan, A. M. *et al.* Search for dark matter produced in association with a single top quark or a top quark pair in proton-proton collisions at $\sqrt{s} = 13$ TeV. *JHEP* **03,** 141 (2019).

224. Hocker, A. *et al.* TMVA - Toolkit for Multivariate Data Analysis. arXiv: `physics/0703039` (Mar. 2007).

225. Antcheva, I. *et al.* ROOT: A C++ framework for petabyte data storage, statistical analysis and visualization. *Comput. Phys. Commun.* **180,** 2499–2512 (2009).

226. Aaij, R. *et al.* Measurement of the ratio of branching fractions $\mathcal{B}(\bar{B}^0 \to D^{*+}\tau^-\bar{\nu}_\tau)/\mathcal{B}(\bar{B}^0 \to D^{*+}\mu^-\bar{\nu}_\mu)$. *Phys. Rev. Lett.* **115.** [Erratum: Phys.Rev.Lett. 115, 159901 (2015)], 111803 (2015).

227. Aaij, R. *et al.* Measurement of the ratio of the $B^0 \to D^{*-}\tau^+\nu_\tau$ and $B^0 \to D^{*-}\mu^+\nu_\mu$ branching fractions using three-prong τ-lepton decays. *Phys. Rev. Lett.* **120,** 171802 (2018).

228. Aaij, R. *et al.* Test of lepton universality in beauty-quark decays. *Nature Phys.* **18.** [Addendum: Nature Phys. 19, (2023)], 277–282 (2022).

229. Di Luzio, L., Fuentes-Martin, J., Greljo, A., Nardecchia, M. & Renner, S. Maximal Flavour Violation: a Cabibbo mechanism for leptoquarks. *JHEP* **11,** 081 (2018).

230. Di Luzio, L., Greljo, A. & Nardecchia, M. Gauge leptoquark as the origin of B-physics anomalies. *Phys. Rev. D* **96,** 115011 (2017).

231. Abe, F. *et al.* Measurement of the ratio $(W \to \tau\nu)/B(W \to e\nu)$, in $p\bar{p}$ collisions at $\sqrt{s} = 1.8$ TeV. *Phys. Rev. Lett.* **68,** 3398–3402 (1992).

232. Abbott, B. *et al.* A measurement of the $W \to \tau\nu$ production cross section in $p\bar{p}$ collisions at $\sqrt{s} = 1.8$ TeV. *Phys. Rev. Lett.* **84,** 5710–5715 (2000).

233. Aaij, R. *et al.* Measurement of forward $W \to e\nu$ production in pp collisions at $\sqrt{s} = 8\,\mathrm{TeV}$. *JHEP* **10,** 030 (2016).

234. Aad, G. *et al.* Test of the universality of τ and μ lepton couplings in W-boson decays with the ATLAS detector. *Nature Phys.* **17,** 813–818 (2021).

235. Tumasyan, A. *et al.* Search for pair-produced vector-like leptons in final states with third-generation leptons and at least three b quark jets in proton-proton collisions at s=13TeV. *Phys. Lett. B* **846,** 137713 (2023).

236. Mikuni, V. & Canelli, F. ABCNet: An attention-based method for particle tagging. *Eur. Phys. J. Plus* **135,** 463 (2020).

237. Collaboration, C. *CMS Internal Analysis Note: Search for vector-like leptons to third generation fermions* CMS Internal Document: AN-21-099. 2022.